# Stony Brook University

# Measurement of Hemodynamic Responses to Neuronal Activity and Drug Effects in the Brain: Combining Laser Doppler and fMRI Techniques

A Dissertation Presented

by

Zhongchi Luo

to

The Graduate School

in Partial Fulfillment of the

Requirements

for the Degree of

Doctor of Philosophy

in

Biomedical Engineering

Stony Brook University
December 2009

Stony Brook University
The Graduate School

Zhongchi Luo

We, the dissertation committee for the above candidate for the
Doctor of Philosophy degree, hereby recommend
acceptance of this dissertation.

Helene Benveniste, PhD/MD, Dissertation Advisor
Professor, Department of Anesthesiology
Adjunct Professor, Department of Biomedical Engineering

Congwu Du, PhD, Dissertation Co-advisor
Assistant Professor, Department of Anesthesiology
Adjunct Professor, Department of Biomedical Engineering

Yingtian Pan, PhD, Chairperson of Defense
Associate Professor, Department of Biomedical Engineering

David Schlyer, PhD
Adjunct Professor, Department of Biomedical Engineering

Mary Kritzer, PhD
Associate Professor, Department of Neurobiology and Behavior

This dissertation is accepted by the Graduate School

Lawrence Martin
Dean of the Graduate Schoo

Abstract of the Dissertation

Measurement of Hemodynamic Responses
to Neuronal Activity and Drug Effects in the Brain:
Combining Laser Doppler and fMRI Techniques

by
Zhongchi Luo
Doctor of Philosophy
in
Biomedical Engineering

Stony Brook University
2009

**Abstract**: Measurements of cerebral hemodynamic and metabolic markers allow us to study brain responses to functional activities, drug effects and patho-physiology complications such as ischemia or epilepsy.

Many different technologies have been invented to measure and spatially map brain activity by recording the local changes of cerebral blood flow (MRI with arterial spin labeling, laser Doppler, $^{15}$O-PET), blood volume (MRI with contrast agent, optic oximetry), blood oxygenation (optic oximetry, functional MRI based on blood-oxygen-level-dependent (BOLD)) and glucose uptake ([$^{18}$F]FDG-PET). This thesis mainly focuses on fMRI and laser optic measurement of cerebral vascular and metabolic responses evoked by somatosensory and drug challenges.

Functional MRI (fMRI) can produce a tomographic view of areas of activation across the entire brain. On the other hand, optical measurements only provide a reflective view of subsurface cortical events. However, by utilizing different optic effects, optical measurements can provide better discrimination between blood volume, oxygenation and flow changes and have the potential for higher spatiotemporal resolution, compared with fMRI.

Interpreting the implications of those functional markers (CBV, CBF, CMRO2, BOLD etc) requires a profound understanding of the complex bio-physical mechanisms underlying the measurements. Therefore, I precede my work with an introduction of the coupling between neuron-metabolic-vascular events and how they exhibit contrast in different functional measurements, first qualitatively and then mathematically.

To test our design of peripheral somatosensory stimulation paradigm and the associated animal experiment protocols, we started with standard local field potential recording and laser Doppler flowmetry, then a customized optic diffusion and fluorescence spectroscopy for tracking local oxygenation and intracellular calcium activity, and finally a home-built, full-field, high resolution flow mapping system based on Laser speckle contrast imaging (LSCI) technique. Then, we moved on to more dedicated studies for characterizing the impacts of lidocaine and cocaine on the brain and further improvement of LSCI technique.

First, we used BOLD based fMRI to characterize lidocaine's analgesic effect on innocuous and acute noxious electric stimulation. The results showed that, unlike opioids, the analgesic action of systemic lidocaine was not reflected in a straightforward interruption of the fMRI-indicated brain activation evoked by either innocuous or

noxious stimulation. Instead, high iv doses lidocaine enhanced S1 and S2 responses to acute nociceptive stimulation, similar to what has been reported for cocaine.

Although with appealing features, LSCI so far is non-quantitative and can only map relative flow change. In order to calibrate LSCI flow measurement, we combined our LSCI system with spectral domain Doppler optical coherence tomography (SDOCT), which is a fully quantitative, high resolution flow-metric technique developed in Dr Pan's group. The simultaneous flow imaging both in phantom and in-vivo animal experiments exhibited good correlation between the two modalities, thus demonstrated the high linearity of LSCI flow measurement and its potential as a quantitative flow imaging tool. This quantification method was then used to characterize the cortical blood flow changes in the rat across the convoluted cortical vascular network in responses to systemic cocaine injection.

Finally, due to the great importance of simultaneous measurement of cerebral blood flow and hemoglobin oxygenation changes, a dual-wavelength laser speckle contrast imaging technique (DW-LSCI) is developed to characterize those dynamics in vivo with high spatiotemporal resolutions. Experimental validation was performed using a rat transient forebrain ischemia model. The results showed that DW-LSCI was able to track detailed hemodynamic and oxygen metabolic changes induced by ischemia, which allowed us to distinguish cerebral arterial and venous flows.

# Table of Contents

# List of Figures

# List of Tables

# List of Abbreviations

| | |
|---|---|
| **AA** | Arachidonic Acid |
| **AC** | Alternating Current |
| **ADC, A/D** | Analog-to-Digital Converter |
| **AP** | Action Potential |
| **ATP** | Adenosine Triphosphate |
| **BOLD** | Blood Oxygen Level Dependent |
| **BP** | Blood Pressure |
| **BW** | Bandwidth |
| **cAMP** | Cyclic Adenosine Monophosphate |
| **CBF** | Cerebral Blood Flow |
| **CBV** | Cerebral Blood Volume |
| **CCD** | Charge Coupled Device |
| **cGMP** | Cyclic Guanosine Monophosphate |
| **CMRglu** | Cerebral Metabolic Rate of glucose consumption |
| **$CMRO_2$** | Cerebral Metabolic Rate of Oxygen consumption |
| **CNS** | Central Nervous System |
| **COX-1** | Cyclooxygenase-1 |
| **CSF** | Cerebrospinal Fluid |
| **DAQ** | Data Acquisition |
| **DC** | Direct Current |
| **DOT** | Diffuse Optical Tomography |
| **DW** | Dual Wavelength |
| **ECG** | Electrocardiogram |
| **EEG** | Electroencephalogram |
| **EPI** | Echo-Planar Imaging (MRI) |
| **$^{18}$FDG** | $^{18}$Fluorodeoxyglucose |
| **FFT** | Fast Fourier Transform |
| **FLASH** | Fast Low Angle Shot Magnetic Resonance Imaging (MRI) |
| **FP** | Field Potential |
| **fps** | Frame Per Second |
| **fMRI** | Functional Magnetic Resonance Imaging |
| **FOV** | Field Of View |
| **FWHM** | Full Width at Half-Maximum |
| **GE/GRE** | Gradient Echo (MRI) |
| **HbR** | Deoxyhemoglobin |
| **$HbO_2$** | Oxyhemoglobin |
| **Hbt** | Total Hemoglobin |
| **IBP** | Intravascular Blood Pressure |
| **IEEE** | Institute of Electrical and Electronics Engineers, Inc. |
| **IP** | Intraperitoneal (injection) |
| **IV / *iv*** | Intravenous (injection) |
| **L-Arg** | L-arginine (amino acid) |
| **LCBF** | Local Cerebral Blood Flow |

| | |
|---|---|
| **LCBV** | Local Cerebral Blood Flow |
| **LD** | Laser Diode |
| **LDF** | Laser Doppler Flowmeter (Flowmetry) |
| **LSCI** | Laser speckle Contrast Imaging |
| **LSF** | Least Square Fit |
| **MAP** | Mean Arterial (blood) Pressure |
| **MEGX** | Monoethylglycinexylidide |
| **mmHg** | Millimeters of mercury column, same as Torr |
| **NA** | Numeric Aperture (Optics) / Number of Averages (MRI) |
| **NADH** | The protonated form of Nicotinamide Adenine Dinucleotide |
| **ND** | Neutral Density (attenuating filter) |
| **NIR** | The Near-Infrared spectral band, 600nm to 900nm |
| **NIRS** | Near-Infrared Spectroscopy |
| **OCT** | Optical Coherence Tomography |
| **OEF** | Oxygen Extraction Fraction |
| **OH** | Hydroxyl Functional Group |
| **$pCO_2$** | The partial pressure of carbon dioxide |
| **PDF** | Probability Density Function |
| **PE** | Polyethylene |
| **PET** | Positron EmissionTomography |
| **$PGI_2$** | prostacyclin |
| **pH** | The negative log of the hydrogen ion (proton) concentration |
| **PNS** | Peripheral Nervous System |
| **$pO_2$** | The partial pressure of oxygen |
| **PPX** | Pipecoloxylidide |
| **psi** | Pounds per Square Inch. 1psi = 60mmHg |
| **PTFE** | Polytetrafluoroethane, Teflon |
| **RARE** | Rapid Acquisition with Relaxation Enhancement |
| **RBC** | Red Blood Cell, erythrocyte |
| **RF** | Radio Frequency |
| **ROI** | Region of Interest |
| **S1/S2** | Primary and Secondary Somatosensory Cortex |
| **$SaO_2$** | Arterial oxygen saturation |
| **SD** | Spectral Domain (OCT) |
| **SE** | Spin Echo (MRI) |
| **SNR** | Signal to Noise Ratio |
| **SPECT** | Single Photon Emission Computerized Tomography |
| **TCD** | Transcranial Doppler Sonography |
| **TE** | Echo Time (MRI) |
| **TR** | Repetition Time (MRI) |
| **TTL** | Transistor–Transistor Logic |
| **VTA** | Ventral Tegmental Area |
| **XYL** | Xylidide |

# Acknowledgements

To Dr Helene Benveniste, Dr Congwu Du, Dr Yingtian Pan, Dr David Schlyer, and Dr Mary Krizter, my most sincere thanks for your participation in my dissertation defense committee, and your willingness to go through the contents of my dissertation.

I would also like to specifically thank the following people and organizations for their various contributions to my doctoral efforts:

Dr Helene Benveniste, for allowing me the freedom to pursue my doctoral research, for introducing me to a world of biomedical research, especially teaching me the art of anesthesia and physiology maintenance for brain function measurement in live animal, which I never knew existed, for often assigning high priority to my fMRI projects when allocating the precious MRI machine time, for meticulously revising many sections of my dissertations.

Dr Congwu Du, for sparking my interest in optical imaging and broadening my view in this field, for encouraging me to become an independent researcher along the way and giving me the freedom and all necessary supports to plan, initialize and accomplish each of my projects in my own way, for helping me and giving me confidence through many difficult times, and for investing great effort to help me get my research works published

Dr Yingtian Pan, for giving me the opportunity to work in his lab, for helping me to feel like a member of his team, for providing invaluable guidance to my design of the DW-LSCI system and allowing me to calibrate my LSCI system using the SD-OCT system newly developed by his group and for offering his precious time and insightful directions to help me get my research works published.

Dr David Smith, for being an invaluable resource of knowledge on both MRI and instrumentation and for timely troubleshooting and problem solving, which I have relied upon on numerous occasions.

Mei Yu, for her surgical and many other valuable skills, which I heavily relied upon in my experiment, for teaching me how to plan and prepare thoroughly for the demanding in-vivo functional experiment and for helping and encouraging me on some of life's other problems along the way.

Melissa Tully, Rubin Pan, Like Shu, for their talent to quickly grasp and perfect various skills for the animal experiments, which I relied upon to run all my experiment and harvest the results and for patiently spending many days helping me track the brain responses to electrical and drug stimulus. Zhijia Yuan, Hugang Ren, for inspiring me with their inventive ideas and creative spirits, for their willingness to offer me the use of any equipment and optic part they had, at any time and for helping me construct the DW-LSCI system. Many others, not mentioned above, have also assisted me in numerous ways, and their assistance was invaluable – for this I thank you all.

We gratefully acknowledge financial support from Department of Energy Office of Science and Biological Research, New York State Office of Science, Technology, and Academic Research, National Institute of Health (K25-DA021200, 2R01-DK059265, and R01-DK068401).

The text of this dissertation in part is a reprint of the materials as it appears in Optic Letter, Applied Optics, Anethesia and Analgesia and J. Innovative Optical Health Sciences. The permission has been granted by the publishers for their noncommercial use. The co-authors listed in the publications directed and supervised the research that forms the basis for this thesis or dissertation.

# List of Publications

**Journal Articles**

- Zhongchi Luo, Zhijia Yuan, Yingtian Pan and Congwu Du, "Simultaneous imaging of cortical hemodynamics and blood oxygenation change using dual-wavelength laser speckle contrast imaging during cerebral ischemia in rat", Optic Letter, 2009, 34(9): 1480-2
- Zhongchi Luo, Zhijia Yuan, Melissa Tully, Yingtian Pan and Congwu Du, "Quantification of cocaine-induced cortical blood flow changes using laser speckle contrast imaging and Doppler OCT", Applied Optics, 2009, 48(10): D247-55
- Zhijia Yuan, Zhongchi Luo, Hugang Ren, Congwu Du and Yingtian Pan, "A digital frequency ramping method for enhancing doppler flow imaging in Fourier-domain optical coherence tomography", Opt Express. 2009, 17(5):3951-63.
- Zhongchi Luo, Mei Yu, S. David Smith, Mary Kritzer, Congwu Du, Yu Ma, Nora D. Volkow, Peter S. Glass and Helene Benveniste, "Effect of intravenous lidocaine on brain activation during non-noxious and acute noxious stimulation of the forepaw: A functional MRI study in the rat", Anesth and Analg, 2009, 108(1): 334-44
- Congwu Du, Zhongchi Luo, Mei Yu, Helene Benveniste, Melissa Tully, Rubing Pan, Britton Chance, "Detection of Ca Dependent neuronal activity simultaneously with dynamic changes in cerebral blood volume and tissue oxygenation from the live rat brain", Journal of Innovative Optical Health Sciences 2009, 2(2):1-12
- Zhongchi Luo, Zhenguo Wang, Zhijia Yuan, Congwu Du, and Yingtian Pan, "Optical coherence Doppler tomography quantifies laser speckle contrast imaging for blood flow imaging in the rat cerebral cortex", Optic Letter 2008, 33(10): 1156-8

**Proceedings**

- Zhongchi Luo, Zhenguo Wang, Zhijia Yuan, Congwu Du, and Yingtian Pan, "Combining laser Doppler speckle contrast imaging and optical coherence tomography for quantitative imaging of cortical blood flow in rat brain", OSA Topic Conf on Biomed Optics, Mar, 2008
- Zhongchi Luo, Helene Benveniste, Mei Yu, Yingtian Pan, Congwu Du, "Laser doppler speckle contrast imaging of cerebral blood flow during functional activation in rat somatosensory cortex", IEEE Northeast BioEngin Conf, 2005 Mar

# Chapter 1 Physiology of Neurovascular Activity and its Biophysical Modeling

## 1.1 Neurovascular physiology

The brain is the command center for major vital regulatory functions in high level living organisms including mammals. Therefore, the brain and its functions are well supplied with nutrients at all times in order to be operational and ready to adapt to rapidly changing tasks.

The basic functional unit of the brain is the neuron. Neurons communicate with each other via synapses between the axon terminals and/or dendritic spines. The membrane encasing the neurons is designed with different permeabilities for ions (e.g. $K^+$, $Na^+$, $Cl^-$, $Ca^{2+}$) in order to maintain its excitability [Marieb, 2003]. For example, in its resting state, neurons maintain a high $K^+$ concentration, a low $Na^+$ and $Cl^-$ concentration in its cytosol and a complementary ionic composition in the extracellular space. This combined intra/extra-cellular ionic milieu, together with other ions, results in a resting intracellular potential 'polarized' at ~-70 mV. A stimulus that activates the $Na^+$ channels may (if sufficiently strong) incur a transmembrane $Na^+$ influx and elevate the local transmembrane potential, a process which is called 'depolarization'. The repolarization process occurs via opening of $K^+$ channels with ensuing $K^+$ efflux which is less intensive but lasts longer than the $Na^+$ influx. The stimulation triggered impulse, if strong enough, can initiate propagation along the axon and pass the stimulus on to other cells. This process is called an 'action' potential [Marieb, 2003], also referred to as a 'spike'. In contrast, synaptic transmissions which can be recorded by means of micro-electrodes are known as field potentials.

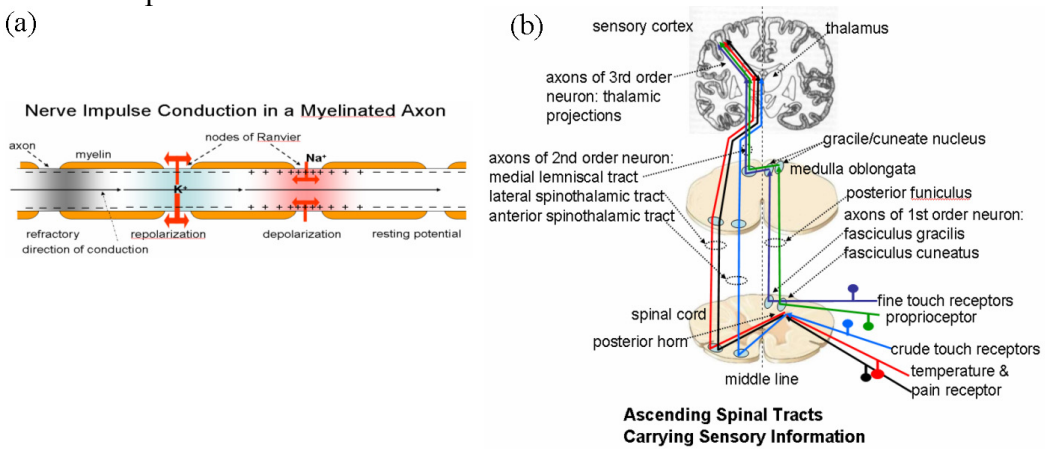


Fig. 1-1 (a) The leap-style propagation of action potential impulse along a myelinated neuron axon (b) The different transduction pathways of five types of somatosensory information within the central nerve system (brain and spinal cord).

In the brain, the long axon projections are myelinated in sections by oligodendrocytes. The transmembrane ion flux only takes place at the gaps of the myelin (between sections), where ion channels are densely populated. Therefore, the locally elicited impulses can propagate rapidly along the axon unidirectionally in a leaping style rather than a passive or a continuous style, which is slower and less economical from a metabolic point of view. Action potential follows the concentration and potential gradient, therefore is not an energy-expensive process [Lauritzen, 2001, Logothetis, 2003] However, the post-synaptic process of restoring equilibrium i.e. reestablishing the electrochemical gradient is ATP dependent because it uses the ATPase, $Na^+$-$K^+$ exchange pump intensively [Ames, 2000; Kida, 2001].

The brain is a big consumer of nutrients and energy, even in its resting state. The cerebral metabolic rate of oxygen consumption ($CMRO_2$) is 3.5-5 ml/100g/min and the cerebral metabolic rate of glucose utilization (CMRglu) is 5-6.5mg/100g/min averagely throughout the brain, but most (94%) of the energy is consumed in grey matter. The blood circulation is responsible for delivering the metabolic nutrients, exchanging and eliminating the waste products. On average, the cerebral blood flow (CBF) perfuses the whole brain at ~50-60 ml/100g/min (~40 ml/100g/min in white matter, ~80 ml/100g/min in grey matter). Those quantities, when summed for the whole adult human brain, amounts to a blood flow of 750-1000 cc/min through the whole brain or 14-20% of cardiac output (~5 L/min from the adult human heart) and ~46cc/min of oxygen consumed through the whole brain or ~20% of the total oxygen consumed in the whole body (~250ml/min $O_2$) respectively, and this should be seen in the perspective that the brain mass accounts for a much smaller fraction of total body weight. (e.g., ~1300g or 1.6% for adult human, ~1-2g or ~0.5% for rat) [Marieb, 2003; Kandel, 2000; Rengachary, 2005].

In the normal microvasculature of mammals, the capillary diameter is 3~8 μm, the arteriole diameters are in the range of 5~150μm, and venules in a wider range of 5~200 μm.

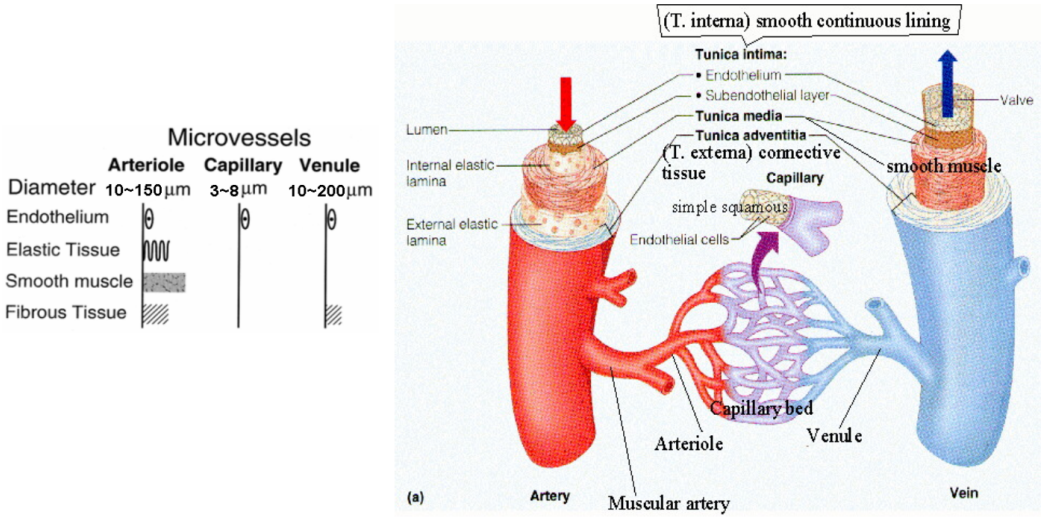


Fig.1-2 The layer structures of three vascular types: artery (arteriole), capillary and vein (venule) and the range of their diameters [Bronzino, 2000; Marieb, 2003].

All the three types of vessels have a single layer of endothelial cells lining the inner lumen which is in direct contact with the blood. The major difference between venules and arterioles is that arterioles have a smooth muscle layer and an elastic layer surrounding its endothelium layer, which can actively modulate the blood flow by either constricting or dilating the vessel diameter according to varying local demands. The venules are devoid of smooth muscle cells and are very compliant. They collapse and expand passively with their blood volume, and thus serve as reservoirs to prevent excessive fluctuations of upstream blood volume and pressures. The capillaries are composed of only a single layer of endothelial cells to allow direct exchange of nutrients and wastes between the tissue and blood. The capillaries, without elastin, collagen or muscle fibers, can only sustain a blood pressure lower than 20 mmHg and maintain a fairly constant diameter. The blood speed in the capillaries is on the order of 0.3~1 mm/sec and the blood in the arterioles and venules can move ten to a hundred times faster than that of the capillaries [Marieb, 2003].

Among the three main types of cell elements (i.e. leukocytes (white blood cells), platelets and erythrocytes (red blood cells) in the blood, the one drawing the greatest interest in neuroimaging is the red blood cells (RBC) which contains hemoglobin in its cytosol. The shape of the RBC is biconcave and the average RBC size is about 3~8 μm in diameter and in the rat it is 1~2 μm thick (varying slightly with species). RBCs are very deformable which enables their easy passage through the 3~10 μm-diameter capillary. RBCs tend to travel in the center of the vessel, where the flow is the fastest, and their concentration decreases towards the vessel wall, where flow is slowest. Thus, when flowing through the vessel, RBCs are sheathed by a layer of plasma which is in contact with the endothelium and, on average, RBCs move faster than plasma in small vessels. This specific feature results in the phenomenon described as the apparent viscosity of flowing blood in vessels being effectively lower than the one measured in bulky volume of whole blood. This observation is referred to as the 'Fahraeus-Lindqvist effect'. In addition, the microvascular hematocrit (*i.e.* volume percentage of red blood cells in blood) is found to be 45~75% lower than that found in larger vessels (40-45%). This phenomenon is known as the 'Fahraeus effect'.

*Physiological role of hemoglobin*

Hemoglobin plays an essential role in delivering oxygen in mammals. The iron atoms folded in the globin units can recurrently be oxidated to $Fe^{3+}$ from $Fe^{2+}$ by binding oxygen when passing through the pulmonary capillaries and reduced to $Fe^{2+}$ by dropping off the oxygen in peripheral capillaries. Each heme group is able to bind one oxygen molecule and therefore, one hemoglobin molecule can bind four oxygen molecules. This oxidation and reduction of the iron atoms is accompanied by conformational changes in the hemoglobin complex and therefore the names, oxyhemoglobin ($HbO_2$) and deoxyhemoglobin (HbR), are given [Kneipp, 2006]. The hemoglobin concentration in blood is normally 6.8~10.5mmol/L. The binding of oxygen to hemoglobin is a so called cooperative binding process because when one oxygen molecule binds to one of the units, conformational changes occur, which makes the binding of the other oxygen molecules more favorable. The hemoglobin carries most of the oxygen content in blood (200cc/L), which is poorly dissolvable in plasma (~5cc/L). The actual oxygen concentration dissolved in plasma is in linear proportion with the partial pressure of oxygen ($PO_2$) in

blood, while the percentage of the oxyhemoglobin among the total hemoglobin (also referred to as oxygen saturation of hemoglobin or $StO_2$) exhibits a Sigmoid-shape relationship with the $PO_2$ in plasma due to the cooperative binding of oxygen to hemoglobin. This relationship is often depicted as an oxygen disassociation curve with $StO_2$(%) vs. PO2 (shown in Fig.1-3). Hemoglobin also has binding sites for $CO_2$ and participates in its transportation. 7% of total $CO_2$ in blood is physically dissolved in plasma, 70% is in the form of bicarbonate anion within the RBC cytosol, and the rest (23%) is in the form of carbamino compound primarily bound to hemoglobins [Marieb, 2003].

In peripheral capillaries, release of $O_2$ from hemoglobin increases its affinity to $CO_2$, therefore facilitates $CO_2$ removal from the tissue; and vice versa in pulmonary capillaries. This is known as the Haldane effect. Conversely, binding of $CO_2$ to hemoglobin in peripheral capillaries, where [$CO_2$] is high, decreases its affinity to $O_2$, which shift the $StO_2$ vs. $PO_2$ curve to the right, and thus promotes $O_2$ release; and vice versa in pulmonary capillaries where [$CO_2$] is low. This is known as Bohr Effect, which is shown as dotted curves in Fig.1-3.

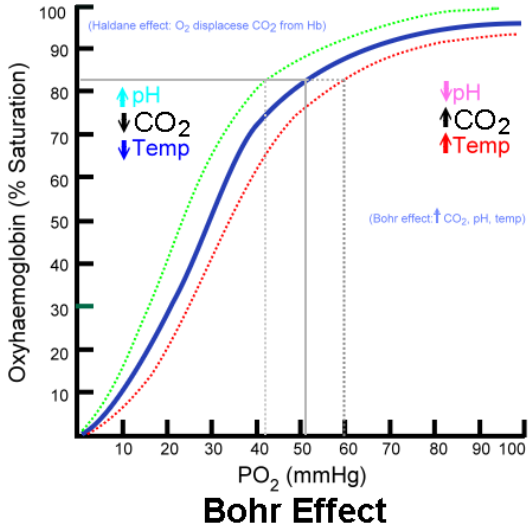


Fig. 1-3 The oxygen disassociation curve of hemoglobin and the shift caused by Bohr Effect. [Marieb, 2003]

*Neuro-metabolic-vascular coupling*

Neural activity creates enhanced regional consumption of $O_2$ ($CMRO_2$) and glucose (CMRglu) in the activated neurons and their supporting astrocytes. The raised metabolic demand evokes a complex pathway which leads to the dilation of local arterioles and the increase of local cerebral blood flow (LCBF) which is known to exceed the increase in local oxygen consumption, therefore lowering the oxygen extraction rate from the arterial blood. In the meantime, veinules are also passively expanded by the pressure drop and thus, combined with the active dilation in arterioles, increase the local cerebral blood volume (LCBV). This whole cascade of events in the brain is known as 'functional hyperemia' or neuro-vascular coupling. The underlying mechanism eliciting this phenomenon as well as the spatiotemporal characterisitcs of this process has intrigued decades of investigations and to a large extent driven the development of novel techniques to probe the brain activity. With the continued advancement in biotechnology

and novel approaches to measure these phenomena, it becomes even more necessary to bridge the biological and technical aspects of measuring neural activity to fully understand the context of the spatial and temporal domains.

The stability and responsiveness of the blood circulation system largely relies on sympathetic/parasympathetic neural regulation and body fluid regulation. However, studies have shown that, the change of local blood flow accompanying brain activation is mainly governed by release of certain metabolites in the process of neuronal activity. For example increased neuronal activity elevates consumption of $O_2$ and glucose and production of $CO_2$ in the activated neurons and their surrounding astrocytes [Magistretti, 1999; Mintun, 2001; Zonta, 2003]. The metabolic demand is met by an increase of the local cerebral blood flow (LCBF) via release of molecules that, via some complex and as yet incompletely understood pathways, cause relaxation in the smooth muscle layer and thus dilation of arterioles. For instance, the elevated $CO_2$ content and lower pH are believed to elicit the endothelial release of a vasodilator (most likely nitric oxide (NO)) in arterioles. Recently, evidence has emerged to support the hypothesis that synaptic glutamate activity mediates (at least partly) the increase in astrocytic $Ca^{2+}$, which elicit endothelial release of another more potent vasodilator prostacyclin ($PGI_2$) [Takano, 2006]. The vasodilator molecules diffuse into the smooth muscle layer and activate production of secondary massagers (such as cGMP and cAMP) that can increase $K^+$ channel activity, induce hyperpolarization and relaxation in smooth muscle layer. [Marieb, 2003]. There might be other potential pathways such as adenosine and epo-oxygenase involved in mediating vasodilation however those pathways are coupled in a way where inhibition of a single one of them does not eliminate the process of vasodilation [Takano, 2006].

LCBF has been recognized as an indirect biomarker of neuron activity and extensively used to study brain activation as well as its coupling with cerebral vasculature. The most popular methods for measuring LCBF are the wide variety of Laser Doppler techniques, which are all based on the Doppler frequency shift of coherent Laser light when the photons are scattered by moving red blood cells. The frequency shift creates fluctuating interference signal in the photon detector (or array), which can be detected to indicate the blood flow.

In the mean time, the dilated arterioles decrease their resistance to blood flow thus relaying the pressure gradient to downstream vessels. The capillary bed as a whole has very low resistance and functions as a pressure drop, and its endothelial wall acts almost like a rigid tube that cannot easily, if at all, be distended. The pressure gradient is hence mostly transferred onto the venules, which are compliant and can be passively expanded to hold the increase in blood flow and the accompanying pressure drop. Thus the arterial dilation and venous expansion in combination results in an increase in the local cerebral blood volume (CBV), which can be tracked by measuring the local content of total hemoglobin [HbT], assuming that local hematocrit does not change with time. [Mandeville, 1999b].

It is widely recognized that, during functional hyperaemia, the oxygen delivered by the increased LCBF largely exceeds the actual oxygen consumption in order to maintain a concentration gradient for oxygen to diffuse from the blood vessel to the consuming cells. [Dunn, 2003; Durduran, 2004; Jones, 2001]. Therefore, the increase in oxygen dropping off from hemoglobin molecules and the forming of deoxygenated hemoglobin is compensated by the accelerated washout by blood flow, which in turn causes a

reduction in the deoxyhemoglobin content in the activated brain region [Buxton, 1997; Ogawa, 1993; Logothetis, 2003]. The local increase of blood volume and the decrease of deoxyhemoglobin content, as discussed above, can also be used as indirect measures to trace brain activation, thanks to the magnetic and optical properties of hemoglobin.

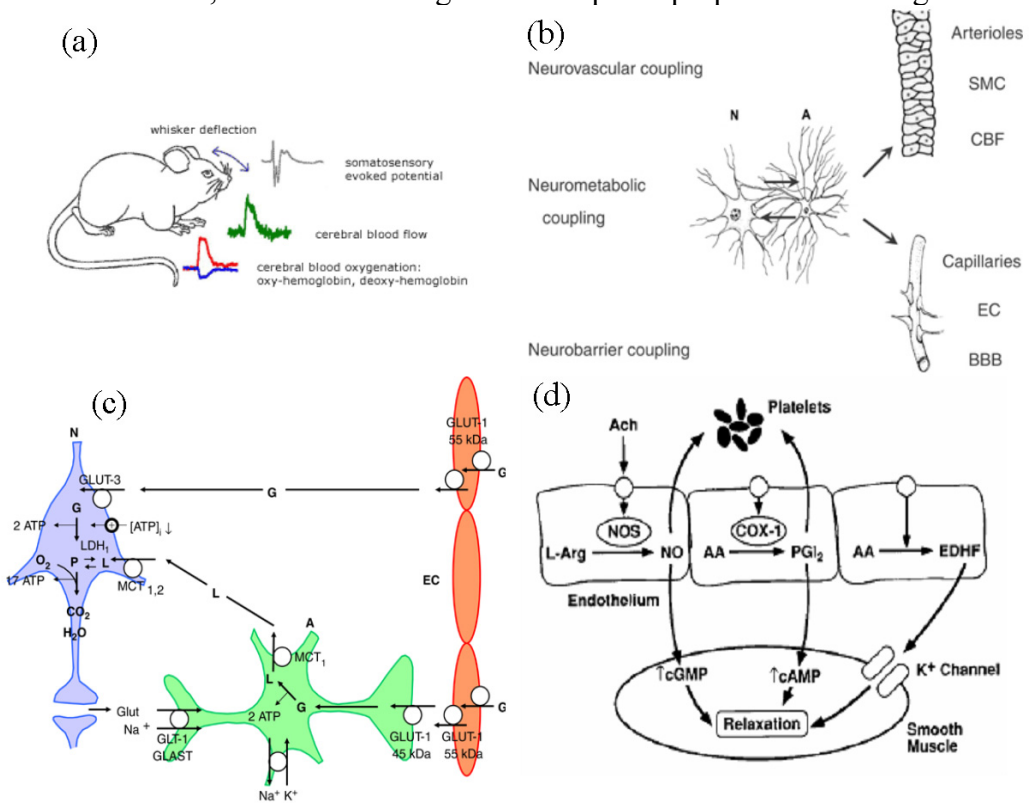


Fig 1-4. (a) The vascular responses (CBF, Δ[HbR], Δ[$HbO_2$]) to neuronal activation (indicated by recorded field potential) in somatosensory barrel cortex evoked by whisker deflection (b) Neuro-vascular-metabolic coupling involves interactions (signals and transports) between neurons (N) and astrocytes (A) that trigger the glycolytic breakdown of glucose. Astrocytes form a relay station between neurons and vascular cells and contribute as an intermediate signaling step in neurovascular coupling. [Leybaert, 2005] (c) the pathways of the glucose metabolism in neurons and surrounding astrocytes (d) Some of the mechanisms of endothelium-dependent relaxation of cerebral vascular smooth muscle. NO is produced by NO synthase (NOS) from the amino acid L-arginine (L-Arg). NO diffuses into the vascular muscle, where it activates soluble guanylate cyclase, causing increased production of cyclic guanosine monophosphate (cGMP), which results in vascular relaxation. Prostacyclin ($PGI_2$) is normally produced by cyclooxygenase-1 (COX-1) from arachidonic acid (AA). $PGI_2$ diffuses to vascular muscle where it activates potassium ion ($K^+$) channels. Increased activity of potassium channels produces hyperpolarization that relaxes vascular muscle [Faraci, 1998].

In near-infra-red (NIR) optical measurements, oxyhemoglobin and deoxyhemoglobin exhibit different absorption spectra and their concentration variations dominate the absorption dynamics during brain activation, while other trivial (such as cytochrome

oxidase, methemoglobin) or static chromophores (such as NADH, bilirubin, myoglobin) usually can be safely ignored. Therefore, by applying multi-wavelength spectroscopy, local $\Delta[HbO_2]$ and $\Delta[HbR]$ can be detected separately to indicate the change of $CMRO_2$ and be added up as $\Delta[HbT]$ so as to reflect the change of CBV. [Devor, 2003; Dunn, 2005; Malonek, 1996].

In MRI measurements, deoxyhemoglobin is relatively paramagnetic and creates a slight disturbance to the homogeneity of the local magnetic field. The inhomogeneity accelerates the local transverse relaxation and decreases the signal intensity in voxels with high [HbR] [Logotheris, 2003]. And this additional transverse relaxation rate ($\Delta R_2$') increases with the [HbR]. Therefore, the change of oxygen consumption accompanying neuron activation can be detected by tracing $\Delta R_2$'[Ogawa, 1993] in a MRI scan designed to be sensitized to this particular effect. This will be discussed in detail in the modeling section (Appendix C).

### 1.2 Biophysical modeling of hemodynmic response to neuron activity

Table 1.1 Model variables, parameters, and typical values

| Variables | Definitions |
|---|---|
| *Neuronal Response* | |
| $\Delta n(t)$ | Net neural activity transient |
| S(t) | Stimulus pattern |
| N(t) | Neural activity transient |
| I(t) | Inhibitory transient |
| subscript: 'ssr' | Subscript for steady state of sustained resting |
| subscript: 'sss' | Subscript for steady state of sustained stimulation |
| subscript: '0' | Subscript for basal level |
| *Neurovascular coupling (linear)* | |
| $n$ [=2–3] | Steady-state flow–metabolism relation: $n = (f-1)/(m-1)$ |
| $h(t)$ | Impulse response of CBF and $CMRO_2$ |
| $\tau_h$ | Width of CBF and $CMRO_2$ impulse response [FWHM=4s] |
| $\delta t_m$ | Delay of CBF relative to neural activity |
| $\delta t_f$ | Delay of $CMRO_2$ relative to neural activity |
| $\delta t$ | Delay of CBF relative to $CMRO_2$ |
| $m$ (=1.0~1.33) | Normalized $CMRO_2$ response to sustained neural activation |
| $f$ (=1.0~2.0) | Normalized CBF response to sustained neural activation |
| $f(t)$ | Relative CBF transient |
| $m(t)$ | Relative $CMRO_2$ transient |
| $e(t)$ | Relative $O_2$ extraction fraction transient |
| *Balloon model parameters* | |
| $\alpha$ [=0.4] | Steady state flow–volume relation: $v=f^{\alpha}$ |
| $\tau_{MTT}$ | Transit time through the balloon ($V_0/F_0$) |
| $\tau_n$ [=0~30s] | Viscoelastic time constant (inflation) |
| $\tau_p$ [=0~30s] | Viscoelastic time constant (deflation) |
| $f_{out}(t)$ | Outflow from the balloon (transiently different from $f(t)$) |
| $v(t)$ | Relative CBV transient |
| $q(t)$ | Relative HbR transient in a voxel |

| | |
|---|---|
| $o(t)$ | Relative $HbO_2$ transient in a voxel |
| $q_b(t)$ | Relative HbR transient in vessel |
| $o_b(t)$ | Relative $HbO_2$ transient in vessel |
| *BOLD signal generation* | |
| $b(t)$ | Relative BOLD signal transient |
| $\beta$ [=1~1.5] | Field depedent exponent |
| $R_2'$ | Susceptibility induced transversal relaxation rate |

* Lower case represents relative change normalized to baseline, upper case represents real physical quantities; constant without '(t)' represnts steady state conditions during sustained stimulation, same as 'sss'

This section attempts to provide a more quantitative way to understand the vascular and metabolic responses to neuronal activation described above. The mathematic models will help us answer not only 'where' in the brain it occurs but also address the more challenging quest of 'how' from the temporal and spatial information revealed by NIR, MRI and other supplemental techniques.

(1) Neuronal Response Evoked by Stimulus

First, we have to model the neural activity $N(t)$ in response to the temporal course of the stimulation $S(t)$. Since the goal here is to derive a general model for the neuro-vascular response, the model will be indifferent to the type of and design of the stimulation paradigm (such as type, frequency, pulse shape etc). The stimulus will be treated simply as an on/off signal that indicates the stimulus duration. In turn, the neuronal response as an 'output' refers to a relative and scalable activity level rather than the actual field potential signal. This model will also include a simple inhibitory feedback $I(t)$ and basal level neural activity $N_0$ [Buxton, 2004]. Coefficient $k$ scales the changing rate of $I(t)$ relative to $N(t)$ A rectangular pulse with duration $T_s$ and amplitude $S_0$ is applied as the stimulus input.

$$N(t) = Max[S(t) - I(t) + N_0, 0] \tag{1-1}$$

$$\frac{dI}{dt} = \frac{kN(t) - I(t)}{\tau_1} = \begin{cases} \dfrac{k(S(t)+N_0) - (k+1)I(t)}{\tau_1} & N(t) \geq 0 \\ \dfrac{-I(t)}{\tau_1} & N(t) \leq 0 \end{cases} \tag{1-2}$$

$$S(0^-) = 0: \quad I(0^-) = I_{ssr} = \frac{kN_0}{k+1}; \quad N(0^-) = N_{ssr} = \frac{N_0}{k+1} \tag{1-3}$$

$$S(0 \leq t \leq T_s) = S_0: \quad I_{sss} = \frac{k(S_0+N_0)}{k+1}; \quad N_{sss} = \frac{(S_0+N_0)}{k+1} \tag{1-4}$$

The steady state conditions ($I_{ssr}$, $N_{ssr}$, $I_{sss}$, $N_{ssr}$) for prolonged resting and stimulating periods ('ssr' and 'sss') are set so that $dI/dt$ equal to zero and $I$ and $N$ can stay in their steady states. Here we also assume that the initial state $I(0^-)$ and $N(0^-)$ meet the equilibrium condition for resting period. The analytical solution to this equation during and after stimulation is given in Appendix. (A-1) and (A-2).

Fig. 1-5 shows the situation of a single stimulus trial with different parameters of ($N_0$, $k$) and a fixed $\tau$ of 1sec. The steady state 'ssr' and 'sss' are attained as prolonged stimulation and rest is given. When no inhibition is involved ($k$=0) and $I(t) \equiv 0$, $N(t)$

follows the shape of $S(t)$ exactly except with a baseline $N_0$. On the contrary, when the inhibition is imposed ($k \neq 0$), the inhibition $I(t)$ behaves like the charging and discharging of a capacitor against abrupt change, which in turn cause a more abrupt overshoot and undershoot in the neural response $N(t)$ at the transitions between stimulus onset and the resting state [Logothetis, 2003]. The threshold, if involved, clamps the undershoot response at zero until the inhibition finally falls below $N_0$ then the inhibition and the response get back to their 'ssr' level [Boynton, 1996].

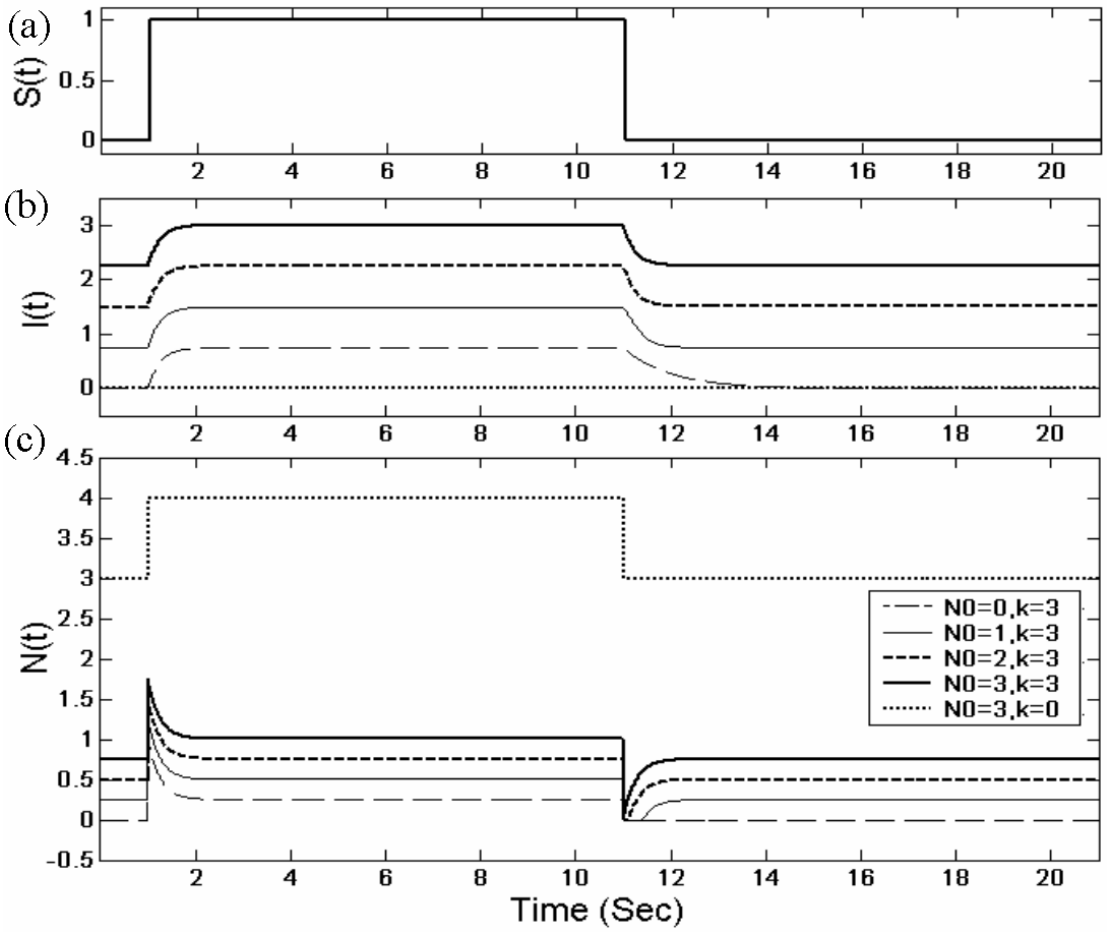


Fig.1-5 (a) a single continuous stimulation trial (10 sec) evoked (b) the inhibitory feedback I(t) and (c) the neural activity response N(t), when ($N_0$, k) equal to (0,3)/dash line, (1,3)/ thin solid line, (2,3)/ thick dotted line, (3,3)/ thick solid line, (3,0)/ thin dotted line respectively and $\tau_1$=1sec for all cases.

Hereafter, the activity response to $S(t)$ will be used as input to the neurovascular coupling mechanism to drive all the hemodynamic responses. To that model, only the relative net changes of $N(t)$ against its steady state baseline is legible as the driving input. So this driving input is normalized as follows:

$$\Delta n(t)=\begin{cases}\dfrac{N(t)-N_{ssr}}{N_{ssr}} & N_0>0\\ N(t) & N_0=0\end{cases} \tag{1-5}$$

(2) Metabolic and CBF transients driven by neuronal activity

The metabolic and hemodynamic responses to neuronal activation involve a complex cascade of chemical and dynamic events, which are still difficult to describe precisely. However, some basic relationships have been disclosed to characterize this process. First, the evoked neuronal activity increases metabolic rate, which can be represented by higher oxygen consumption rate ($CMRO_2$ or $M$) (oxygen content consumed in a unit tissue volume in a unit of time). The demand for more oxygen is satisfied by release of molecular 'moieties' required for vessel dilation which then increase the local cerebral blood flow (CBF or $F$) (blood volume through a unit of tissue volume in a unit of time). Local $CMRO_2$ is derived by the product of CBF, oxygen extraction fraction (OEF or $E$, a percentage variable) and the arterial concentration of $[HbO_2]_{art}$.

$$CMRO_2=E\cdot[HbO_2]_{art}\cdot CBF \tag{1-6}$$

Given that $[HbO_2]_{art}$ remains nearly constant, the baseline-normalized functions of $CMRO_2$, CBF and OEF ($m(t)$, $f(t)$, $e(t)$) the can be written as below.

$$m(t)=e(t)\cdot f(t) \tag{1-7}$$

The above mentioned surplus of blood delivery over actual oxygen consumption can then be characterized by the ratio $n=(f-1)/(m-1)$ in the steady state for a modest functional hyperemia. $n$ is 2~3 under normal conditions [Davis, 1998; Hoge, 1999]. Therefore $e(t)$ should decrease with excessive increase of $f(t)$ during function hyperemia, as shown in Fig.1-6. The case n=∞ represents a hypercapnia challenge, which is assumed not to change the metabolic rate ($m(t)\equiv 1$).

The complex chemical and dynamic mechanisms of metabolic and CBF changes have lead to an alternative attempt to model the neuro-vascular coupling process as a black-box system [Friston, 2000] and simply characterize the input and output relationship without knowing the exact inner states. This method, in its simplest expression, treats the $CMRO_2$ changes as an output linearly driven by neural activity as the input and then simply scale it to the CBF change with only a period of latency. A plausible convolution core is a gamma-variant distribution function [Boynton, 1996], which has a sharp initial response. Here, the parameters $k$=3, $\tau_h$=0.968 sec (so FWHM=4 sec) will be prescribed for the convolution core, as shown in Fig.4.a.

$$h(t)=\frac{1}{\tau_h k!}\left(\frac{t}{\tau_h}\right)^k e^{-t/\tau_h} \tag{1-8}$$

The latencies from neuronal activation to metabolic demand were introduced as $\delta t_m$. The vascular response is further delayed in relation to the metabolic increase by $\delta t$. As will be seen later, it is this lag between $f(t)$ and $m(t)$ that provides the theoretical possibility for the initial dip in the OEF change and BOLD signal. As mentioned above, the net increase magnitude $f$-1 and $m$-1 have ratio of n.

$$m(t)=1+(m-1)h(t-\delta t_m)\otimes \Delta n(t) \tag{1-9}$$

$$f(t)=1+n\cdot(m(t-\delta t)-1) \tag{1-10}$$

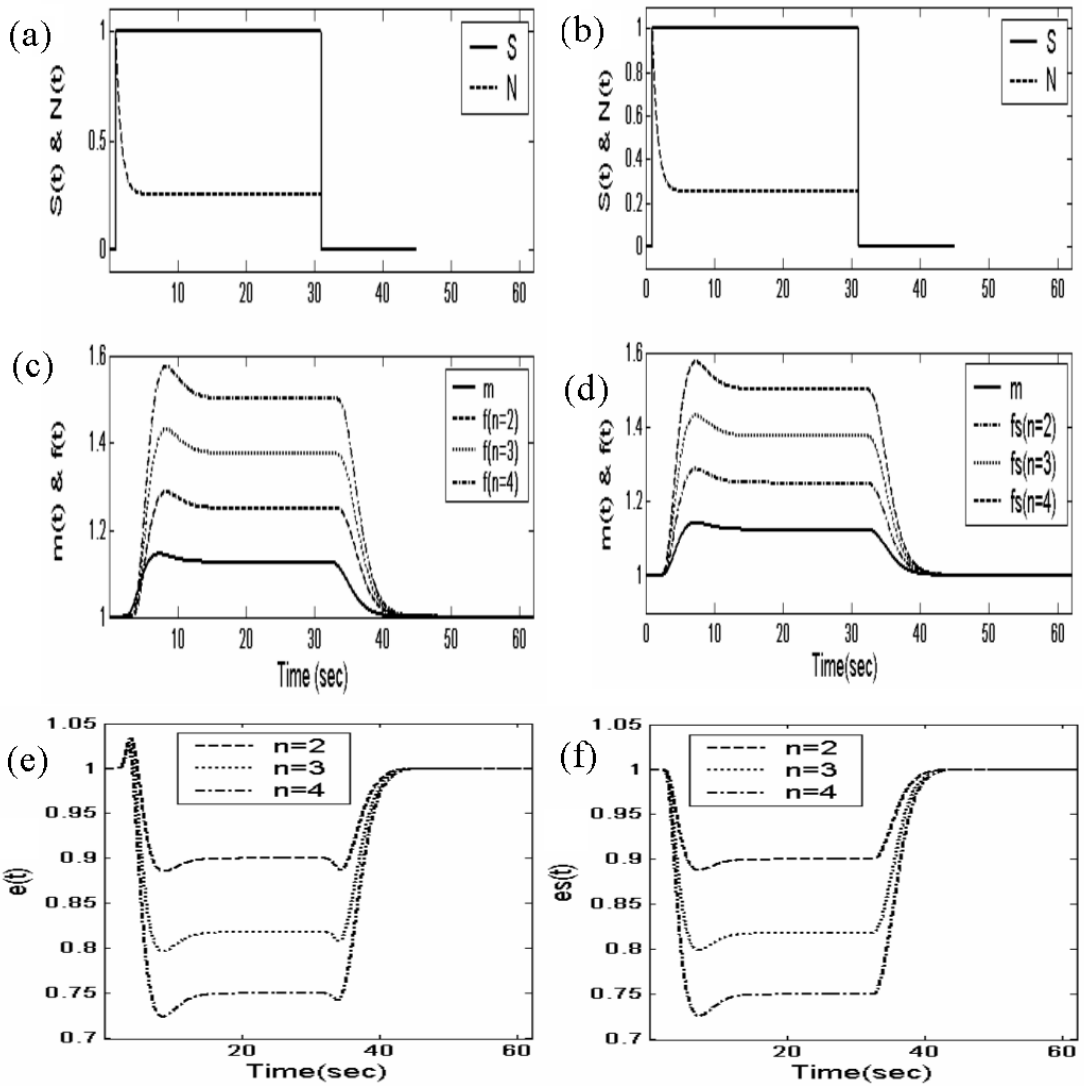


Fig.1-6. The normalized CBF ($f(t)$), $CMRO_2$ ($m(t)$) (in (c) and (d)) and OEF ($e(t)$) (in (e) and (f)) driven by neuronal activity change $\Delta n(t, N_0=0, k=3)$ (in (a) and (b)) through convolution with the lowpass core function h(t) in Fig. 1-4. The origin excitation is a continuous stimulus S(t) lasting 30 sec (in (a) and (b)). In steady state, $\Delta m$=10% for all case (solid line), the ratio n to $\Delta$f is 2 (dashed line ), 3(dotted line), 4 (dash-dotted line) respectively. For the left side, $f$ and $m$ are out of phase from each other with the latences $\delta t_f$=2sec and $\delta t_m$=1sec, for the right side, they are in phase with the latences $\delta t_f = \delta t_m$=1sec.

Fig.1-6 simulates the normalized CBF and $CMRO_2$ change driven by the convolution model and the OEF with different n. It is clear that the OEF goes down during functional hyperemia, except at the beginning of the response, during which $e(t)$ overshoots above the baseline, reflecting a more complete use of the local oxygen content, due to the lagging of CBF increase (on the left side of Fig.1-6).

(3) Balloon model (CBV and [HbR]) of hemodynamic response

The local cerebral blood volume (CBV or $V$, venous blood volume within single unit tissue volume) and local [HbR] change apparently is directly caused by the local CBF and CMRO2 changes. Here, it needs to be pointed out that this local HbR content refers to the apparent concentration in total tissue volume ($[HbR]_a$ or Q), in contrast to the concentration in venous volume $[HbR]_b$, which is known as Q(t)/V(t).

This section will provide an intuitive physical model, instead of an empirical one, for the CBV and $[HbR]_a$, which will directly incur the susceptibility change and hence the BOLD signal. A balloon model driven by relative transients of CBF and $CMRO_2$ was recently proposed by [Buxton, 2004] as a suitable method in understanding this process.

In this ballon model the venules are treated as a balloon filled by blood flow through the capillaries (i.e. CBF) and drained by venous flow, noted as $CBF_{out}$. The dilation of arterioles reduces upstream resistance and passes part of the pressure gradient to the downstream venules. This in turn causes passive expansion in venules, thus increases the CBV. The steady state relationship between relative CBV and CBF changes(i.e. $v$ and $f$) can be approximated by a simple empirical power function [Grubb, 1974].

$$v=f^{\alpha} \tag{1-11}$$

where $\alpha$ is a physiology-dependent parameter and typically takes a value of 0.4 under normal conditions.

Moreover, in the balloon model, there is another way to define OEF or $E$ in terms of local CBV and HbR content as follows. This definition is only valid in steady state, where we have e=m/f=q/v:

$$E=\frac{[\mathrm{HbR}]_b}{[HbO_2]_{art}}=\frac{Q}{V\cdot[HbO_2]_{art}} \tag{1-12}$$

The transient relationships of CBF, CBV, $CMRO_2$, $[HbR]_a$ can be derived based on those observed in steady state. The deduction for the balloon model in Appendix-B gives the differential equations for the relative dynamic changes of CBV and $[HbR]_a$. They can be numerically solved to get transients of $v(t)$ and $q(t)$ during functional hyperemia, knowing driving input $f(t)$ and $m(t)$ and initially $v(0)=q(0)=1$.

$$\frac{dv(t)}{dt}=\frac{f(t)-v(t)^{\frac{1}{\alpha}}}{\tau+\tau_{MTT}} \tag{1-13}$$

$$\frac{dq(t)}{dt}=\frac{1}{\tau_{MTT}}\left[m(t)-\frac{q(t)}{v(t)}\frac{\tau\cdot f(t)+\tau_{MTT}\cdot v(t)^{\frac{1}{\alpha}}}{\tau+\tau_{MTT}}\right] \tag{1-14}$$

We are now able to predict the transients for the local neuronal activity ($n(t)$), metabolic ($m(t)$, $e(t)$, $q(t)$, $o(t)$ (see Appendix-B)) and hemodynamic responses ($f(t)$, $v(t)$) from external stimulation S(t). Those signals can be directly measured or indirectly derived from EEG, NIR oxymetry and laser Doppler signals recorded on the brain surface. While the BOLD signal is a mixed effect of those responses, but it has the unique ability to non-invasively locate the activities deep inside the brain.

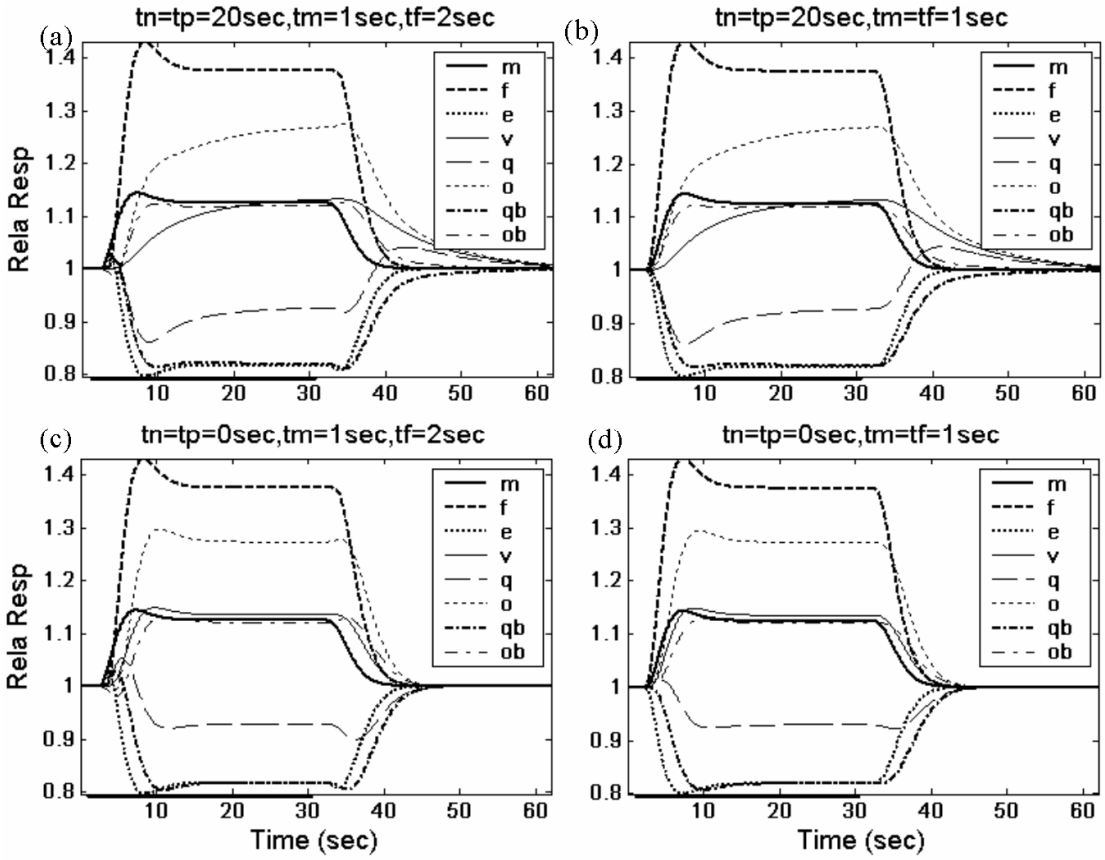


Fig. 1-7 Simulation of Balloon model: the normalized CBV ($v(t)$ as thin solid line), $[HbR]_a$ ($q(t)$ as thin dash line) is driven by normalized CBF ($f(t)$ as thick dash line) and $CMRO_2$ ($m(t)$ as thick solid line)(n=3), and thereout OEF ($e(t)$ as thick dotted line), $[HbO_2]_a$ ($o(t)$ as thin dotted line), $[HbR]_b$ ($q_b(t)$ as thick dash-dotted line) and $[HbO_2]$ ($o_b(t)$ as thin dash-dotted line). The case for nonsynchronous $\{m(t), f(t)\}$ input are shown in (a, c), and the case for synchronous $\{m(t), f(t)\}$ are shown in (b,d) for comaprison. The case with a long viscoelastic times $\tau_n$ and $\tau_p$ (20 sec) in addition to $\tau_{MTT}$ (3 sec) is shown in (a, b), comparing with the two cases without viscoelastic times shown in (c, d).

The comparison between synchronous and non-synchronous $m(t), f(t)$ input discloses no major differences in the $q(t)$, $v(t)$ output of balloon model but the non-synchronous input causes initial overshoot in the $q_b(t)$, and downshoot in $o(t)$ and $o_b(t)$. The long viscoelastic times greatly slow down the change of $v(t)$, $q(t)$ and $o(t)$ towards their steady state and baseline and remove the overshoot in $o(t)$ at the beginning of the response and creates an overshoot in q(t) before returning to baseline presented when $\tau_p=\tau_n=0$. However, it is interesting that no prominent differences related to the viscoelastic times was found in the dynamics of normalized venuous concentration of HbR ($q_b(t)$) and $HbO_2$ ($o_b(t)$) .

### 1.3 BOLD signal and its temporal characteristics

The BOLD signal depends on a combination of vascular (CBF, CBV) and oxygen metabolic ($CMRO_2$) changes, and as a $T_2^*$-weighted signal, is also effected by the baseline physiological parameters [Ogawa, 1993; Logothetis, 2003] The change of signal level ( $\Delta S/S_0$) can be given as dynamic functions of {q,v} or in terms of {m,f} for steady state only, as deducted in Appendix C [Davis, 1998].

$$b-1=\frac{\Delta S}{S_0}=A\left(1-\left(\frac{q^{\beta}}{v^{\beta-1}}\right)\right)=A(1-ve^{\beta})\Big|_{steady\ state}=A\left(1-\left(\frac{m^{\beta}}{f^{\beta-\alpha}}\right)\right) \qquad (1\text{-}15)$$

$$\left\{A=TE\cdot R_{20}^{'}\right\}$$

During normal functional hyperemia, the local $E$ and HbR content would yield a modest decrease and V would increase slightly. The net effect will reduce the transverse decay rate thus increase the local GE signal above baseline.

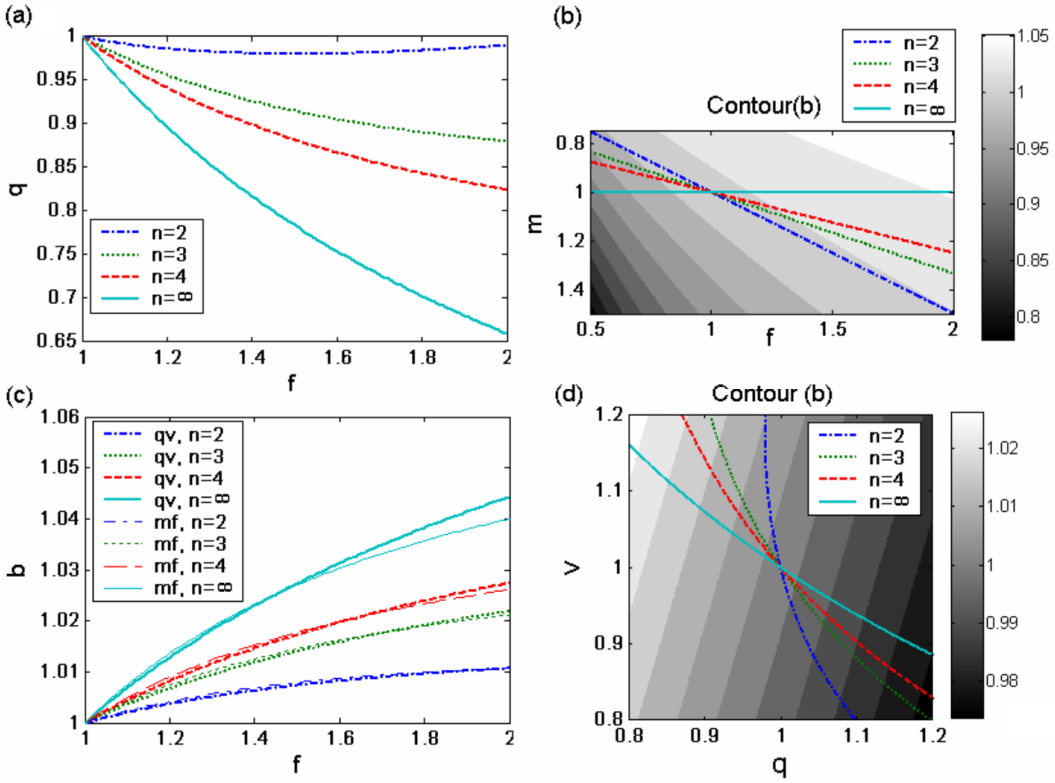


Fig.1-8 Steady state relation of (**a**) normalized $[HbR]_a$ ($q$) *vs* CBF ($f$) ($q=(f+n-1)\,f^{\alpha-1}/n$), (**b**) $CMRO_2$ ($m$) *vs* CBF ($f$) overlapped on the contour map of BOLD ($b$), (**c**) BOLD ($b$) *vs* CBF ($f$) (**d**) $[HbR]_a$ ($q$) *vs* CBV ($v$) overlapped on the contourmap of BOLD ($b$). The solid line represent for $n=\infty$ (hypercapnia challenge), dashed line for n=4, dotted line for n=3, dash-dotted line for n=2.

Based on the models in this text so far, all the steady state quantities m, f, e, q, v have a deterministic relationship (equ (1-6,11,12)) once a $n$ is given. Therefore, we are able to predict the steady state change of BOLD ($b$) given values of $n$ and any one of $\{m, f, q, v\}$ using equ (1-15). Therefore, a BOLD contour-map on the grid of $\{m, f\}$ and {q, v} is presented in Fig.1-8.b and d, respectively. Unlike the steady state BOLD estimation in

terms of $\{m, f\}$, the estimation in terms of {v, q} can be used to describe the transients of BOLD response as shown in Fig.1-9.

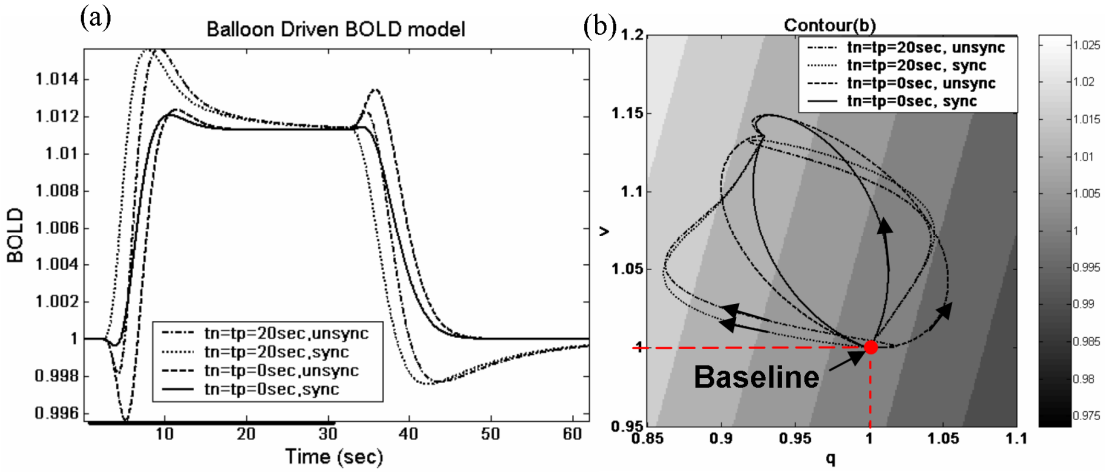


Fig. 1-9 (**a**) The transient dynamics of BOLD change using Equ (1-15) (**b**) The traces of $\{q(t), v(t)\}$ from Balloon model on top of the contour-map of BOLD. The 2 cases for synchronous $\{m(t), f(t)\}$ input to the Balloon model are plotted with dotted and solid , the 2 case for non-synchronous $\{m(t), f(t)\}$ are with dashed and dot-dashed line. The 2 cases with only mean transition time ($\tau_{MTT}$) for venous inflation-deflation in Balloon model are represented by solid and dashed line and take counterclockwise traces, the 2 cases with additional vessel viscoelastic time ($\tau_n$=$\tau_p$=20sec) for venous inflation-deflation in Balloon model by dotted and dot-dashed line, and take clockwise traces.

Finally, using Eq (1-15) with $\{q(t), v(t)\}$ from balloon model, we can predict the transient nature of the BOLD response ($b(t)$). The BOLD transients with different time parameters in hemodynamic models are compared in Fig 1-9.a. The imposing of lag $\delta t$ between $m(t)$ and $f(t)$ in the convolution make a difference by inducing an initial dip before the BOLD elevation and an minor overshoot at the end the elevated plateau, while the addition of long viscoelastic times ($\tau_n$, $\tau_p$) to the mean transition time ($\tau_{MTT}$) for vessel inflation-deflation in the balloon model results in an overshoot at the beginning of the elevated plateau and an undershoot before returning to baseline. Fig.1-9.b translates those BOLD transients into the $\{q(t), v(t)\}$ traces superimposed on the BOLD contour map based on Equ (1-15), where contribution from $\{q(t), v(t)\}$ to BOLD change can be easily examined. More interestingly, the imposing of additional viscoelastic times makes a big difference in the directions of the $\{q(t), v(t)\}$ traces. For example:

(1) the initial dip in the non-synchronous case with long viscoelastic times (shown as dot-dashed lines) is mainly from the temporary increase of [HbR] ($q(t)$), while in the case with only $\tau_{MTT}$ (as dashed line) is from an increase of [HbR] ($q(t)$) counteracted by increasing CBV ($v(t)$); the subsequent BOLD change represented by the dashed line is alike with solid line (synchronous case with only $\tau_{MTT}$) basically following the normal conceit of BOLD process;

(2) In the case for synchronous $\{m(t), f(t)\}$ and with only $\tau_{MTT}$ as shown by solid line, the BOLD change is more from CBV ($v(t)$) than from [HbR] ($q(t)$) and follows the normal

conceit of the BOLD process, while in the cases of additional long viscoelastic times shown by the dotted and dot-dashed line, the BOLD increase is contributed more by a decreased [HbR] ($q(t)$) and the BOLD decrease is first made by an increased $q(t)$ counteracted by still increasing $v(t)$ and then by the coalition of an increased $q(t)$ and a decreased $v(t)$ until an undershoot take places and finally another decrease of $q(t)$ bring the BOLD back to baseline.

## 1.4 Summary

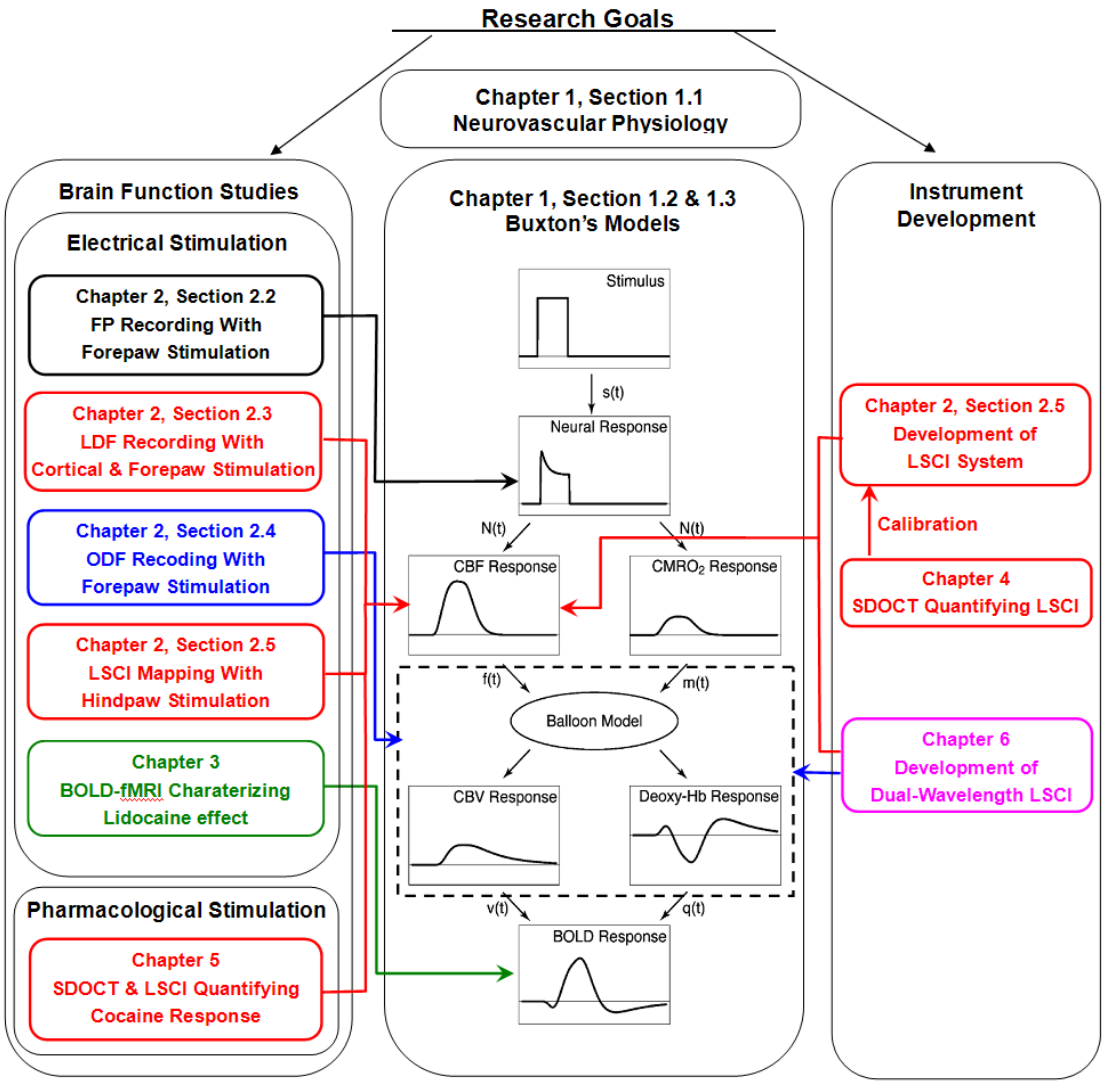


Fig. 1-10 The frame work of this thesis and the its connections with Buxton's models [Buxton, 1997; Buxton, 2004] linking the applied stimulus to the resulting physiological responses (ie. Changes in FP (linked by black arrow), CBF (linked by red arrows), CBV/Δ[Hb] (linked by blue arrows)) and the measured BOLD response (linked by green arrow).

As an introduction, this chapter briefly reviewed the biological and physiological mechanism of the neuron-metabolic-vascular coupling in response to brain activation and described how the magnetic and optical properties of the involved vascular and cellular contents, such as the Doppler scattering of RBC as well as the differential optical absorption and magnetic susceptibility of $HbO_2$/HbR, can be used to manifest the cerebral hemodynamics in brain function studies.

Furthermore, for better interpreting the implications of those functional markers (FP, CBV, CBF, $CMRO_2$, BOLD etc), a series of bio-physical models proposed by Buxton and his coworkers were laid out to mathematically describe the cascade of neuron-metabolic-vascular events evoked by external stimulation, as shown by diagram in Fig.1-10. To summarize of the key points characterized by those models:

First, it included an empirical model for depicting the general signal profile of field potential (FP). FP is a neuronal response closely related with the metabolic and vascular response and usually starts with a peak followed by a lowered plateau phase This amplitude profile can be subsequently used as the input to a pair of responsive functions to approximate the relative changes of cerebral blood flow (CBF) and oxygen consumption rate ($CMRO_2$) during functional hyperemia. Both CBF and $CMRO_2$ responses lag behind but also last longer than the neuronal response. And the increase of CBF is greater than the increase of $CMRO_2$, which results in surplus oxygen supply in the activated area. Then, an interesting balloon model succeeded to simulate the venous charging and discharging of blood, $HbO_2$ and HbR at different rates. In veinules, [HbR] decreases because it formation by oxygen metabolism is overdrawn by increased blood washout. Both CBV and [HbR] change extend even longer due to viscoelasticity of the venous network. This formed the basis to resolve their dynamics optically using multi-wavelength spectroscopy and to infer the changes of oxygen consumption. Eventually, the expression of $T_2^*$ weighted MRI contrast was given to predict how those hemodynamic processes would mix nonlinearly to influence gradient echo strength and to give rise to the BOLD contrast. And the expression also explained why BOLD contrast is effected by location and baseline in functional MRI for mapping activated brain regions.

The mathematical models not only can help us have a more profound understanding of those function indications, but also include a variety of interesting parameters, such as latencies and visco-elastisity etc, that can possibly mediate the amplitudes and times courses obtained from our functional measurements. Thus they also served us as a reminder of those contexts in designing the in-vivo experiments, processing the signal and interpreting the outcome for technical developments and various experimental studies pursued in this thesis. As outlined by the frame work in Fig.1-10, the models linking the applied stimulation to evoked neuro-response and accompanying cerebral blood flow and tissue oxygenation will guide our in vivo measurement of field potential, cerebral blood flow and tissue oxygenation change in Chapter 2. The model for generating BOLD signal will assist us in evaluating lidocaine'e analgesic effect on brain activation using fMRI in Chapter 3. In addition, the models for cerebral blood flow and tissue oxygenation changes also give us important physiological clues for developing and calibrating the laser speckle contrast imaging (LSCI) system in Chapter 2 and 4, as well as integrating multi-wavelength into the LSCI system to build the combined flowmeter and oxyimeter in Chapter 6.

## 1.5 List of References


1-1) Ames III A. CNS energy metabolism as related to function. Brain Res. Rev. 2000, 34: 42.

1-2) Bronzino JD. The Biomedical Engineering Handbook, Second Edition ed. Boca Raton, FL: CRC Press LLC. 2000.

1-3) Boynton GM, Engel SA, Glover GH, Heeger DJ. Linear systems analysis of functional magnetic resonance imaging in human V1. J. Neurosci. 1996, 16: 4207–21.

1-4) Buxton RB, Frank LR. A model for the coupling between cerebral blood flow and oxygen metabolism during neural stimulation. J. Cereb. Blood Flow Metab. 1997, 17: 64.

1-5) Buxton RB, Uludag K, Dubowitz DJ, Liu TT. Modeling the hemodynamic response to brain activation. NeuroImage, 2004, 23: S220.

1-6) Davis TL, Kwong KK, Weisskoff RM, Rosen BR. Calibrated functional MRI: mapping the dynamics of oxidative metabolism. Proc. Natl. Acad. Sci. U. S. A. 1998, 95: 1834.

1-7) Devor A, Dunn AK et al.. Coupling of total hemoglobin concentration, oxygenation, and neural activity in rat somatosensory cortex. Neuron, 2003, 39-2: 353.

1-8) Dunn AK, Devor A et al., Simultaneous imaging of total cerebral hemoglobin concentration, oxygenation, and blood flow during functional activation. Opt Lett. 2003, 28: 28.

1-9) Dunn AK, Devor A, Dale AM, Boas DA. Spatial extent of oxygen metabolism and hemodynamic changes during fucntional activation of the rat somatosensory cortex. NeuroImage. 2005, 27: 279.

1-10) Durduran T and Yu G et al., Diffuse optical measurement of blood flow, blood oxygenation, and metabolism in a human brain during sensorimotor cortex activation. Opt. Lett. 2004, 29-14: 1766.

1-11) Faraci FM and Heistad DD. Regulation of the Cerebral Circulation: Role of Endothelium and Potassium Channels. Physiol. Rev. 1998, 78: 53.

1-12) Friston KJ, Mechelli A, Turner R, Price CJ. Nonlinear responses in fMRI: the Balloon model, Volterra kernels, and other hemodynamics. NeuroImage. 2000, 12: 466.

1-13) Grubb RL, Raichle ME, Eichling JO, Ter-Pogossian MM. The effects of changes in PaCO2 on cerebral blood volume, blood flow, and vascular mean transit time. Stroke. 1974, 5: 630.

1-14) Hoge RD and Atkinson J et al. Linear coupling between cerebral blood flow and oxygen consumption in activated human cortex. PNAS-USA. 1999, 96, 16: 9403.

1-15) Jones M and Berwick J et al., Concurrent optical imaging spectroscopy and laser-Doppler flowmetry: the relationship between blood flow, oxygenation, and volume in rodent barrel cortex. Neuroimage. 2001, 13: 1002.

1-16) Kandel et al. Principles of Neural Science. New York: McGraw Hill. 2000.

1-17) Kida I, Hyder F, Behar KL. Inhibition of voltage-dependent sodium channels suppresses the functional magnetic resonance imaging response to forepaw somatosensory activation in the rodent. J. Cereb. Blood Flow Metab. 2001, 21: 585.

1-18) Kneipp J, Balakrishnan G, Chen R, Shen TJ, Sahu SC, Ho NT, Giovannelli JL, Simplaceanu V, Ho C, Spiro TG. Dynamics of allostery in hemoglobin: roles of the penultimate tyrosine H bonds. J Mol Biol. 2006, 356(2): 335.

1-19) Lauritzen, M. Relationship of spikes, synaptic activity, and local changes of

cerebral blood flow. J. Cereb. Blood Flow Metab. 2001, 21:1367.
1-20) Leybaert L. Neurobarrier coupling in the brain: a partner of neurovascular and neurometabolic coupling. J. Cereb. Blood Flow Metab. 2005, 25: 2.
1-21) Logothetis NK. The underpinnings of the BOLD functional magnetic resonance imaging signal. J. Neurosci. 2003, 23: 3963.
1-22) Magistretti PJ, Pellerin L. Cellular mechanisms of brain energy metabolism and their relevance to functional brain imaging. Philos. Trans R Soc Lond B Biol Sci. 1999, 354: 1155.
1-23) Malonek D, Grinvald A. Interactions between electrical activity and cortical microcirculation revealed by imaging spectroscopy: implications for functional brain mapping. Science. 1996, 272-5261: 551.
1-24) Mandeville JB, Marota JJA, Weisskoff RM et al. Evidence of a cerebrovascular post-arteriole Windkessel with delayed compliance. J. Cereb. Blood Flow Metab. 1999b, 19: 679.
1-25) Marieb EN. Human Anatomy & Physiology. Benjamin Cummings. 2003, 6 ed.
1-26) Mayhew J, Johnston D et al. Increased oxygen consumption following activation of brain: theoretical footnotes using spectroscopic data from barrel cortex. Neuroimage. 2001(13): 975.
1-27) Mintun MA, Lundstrom BN, Snyder AZ, Vlassenko AG, Shullman GL, Raichle ME. Blood flow and oxygen delivery to human brain during functional activity: Theoretical modeling and experimental data. PNAS. 2001, 98: 6859.
1-28) Ogawa S, Menon RS, Tank DW, Kim SG, Merkle H, Ellerman, JM, Ugurbil K. Functional brain mapping by blood oxygenation level-dependent contrast magnetic resonance imaging: a comparison of signal characteristics with a biophysical model. Biophys. J. 1993, 64: 803.
1-29) Raichle ME. Behind the scenes of functional brain imaging: A historical and physiological perspective. PNAS.1998, 95: 765.
1-30) Rengachary SS, Ellenbogen RG, editors, Principles of Neurosurgery, Edinburgh: Elsevier Mosby, 2005.
1-31) Takano T, Tian G, Nedergaard M et al, Astrocyte-mediated control of cerebral blood flow, Nat Neurosci. 2006, 9(2: 260.
1-32) Zonta M, Angulo MC, Gobbo S, Rosengarten B, Hossmann KA, Pozzan T, Carmignoto G, “Neuron-to-Astrocyte Signaling is Central to the Dynamic Control of Brain Microcirculation,” Nat. Neurosci. 2003, 6: 43.

# Chapter 2 Experimental Studies of Somatosensory Stimulation

## 2.1 Introduction

In Chapter1, we have reviewed the mechanisms and characteristics of neuro-metabolic-vascular coupling, and in this chapter we will use animal models to experimentally study the neurovascular activation induced by electrical stimulation. Two traditional approaches *i.e.* field potential (FP) recording and Laser Doppler flowmetry (LDF) as well as two newly-developed optic techniques of our lab *i.e.* optical diffusion and fluorescence (ODF) probe and laser speckle contrast imaging (LSCI) were used for detecting neuronal activity accompanying electrical sensory stimulation.

It has been widely reported that metabolic and vascular changes are correlated with the local field potential signal [Thomsen, 2004; Offenhauser, 2005], which represents a direct measure of neuronal activity in the brain and serves as the 'gold standard'. To validate the animal preparation and optimize the stimulation paradigm used in many studies throughout the thesis, we first recorded electrophysiological signals by recording the FP in the somatosensory cortex of rat brain in response to the electrical forepaw stimulation. As described in Chapter 1, the energy is consumed mainly in the post-synaptic processing (resulting in field potential change) rather than axonal transmission (action potential, or 'spike') during neuron activation. Therefore the local field potential reflects of the post-synaptic ionic current in response to forepaw stimulation of graded current intensity.

The measurement of hemodynamic response has become the cornerstone for tracking neural activity in brain function studies. Although it is an indirect measure of neural activation, it is extensively used to map brain activation in response to a wide variety of behavioral and cognitive paradigms in the normal and diseased human brain. To study the coupling between neuronal activity and cortical hemodynamic responses, we used various optical approaches to measure the different aspects of electrically-elicited hemodynamic changes in the somatosensory cortex.

First, we use LDF to track LCBF changes in somatosensory cortex in response to direct cortical stimulation or forepaw stimulation; Secondly, we use our ODF probe to simultaneous capture the cortical changes of cerebral blood volume (CBV), tissue oxygenation ($S_tO_2$) and intracellular calcium($[Ca^{2+}]_i$) fluorescence induced by forepaw stimulation. Unlike the vascular manifestation of brain activation by the signals of CBV, CBF and $S_tO_2$, the $[Ca^{2+}]_i$ change is a cellular response that is directly associated with neuronal activity. Thirdly, we use our newly-developed LSCI technique to image LCBF change in response to the electrical stimulation. LSCI technique, based on the derivative phenomenon of Doppler effect, associates the scatterer speed with the spatial statistics of the speckle pattern in the image [Briers, 2001; Durduran, 2004; Briers, 1996]. It provides sharp contrast for vasculature at sub-millimeter spatial resolution only using low-cost off-the-shelf photographic equipments and can track relative flow changes at sub-second

temporal resolution (down to the order of 10 milliseconds if necessary) for continuous digital image acquisition.

The preliminary results obtained from these studies have been partially published (Luo et al., IEEE NE BioEngin Conf, 2005; Du et al., JIHO 2009) and we will present more details in the following sections.

## 2.2 Recording local field potential changes in brain cortex in response to electrical forepaw stimulation

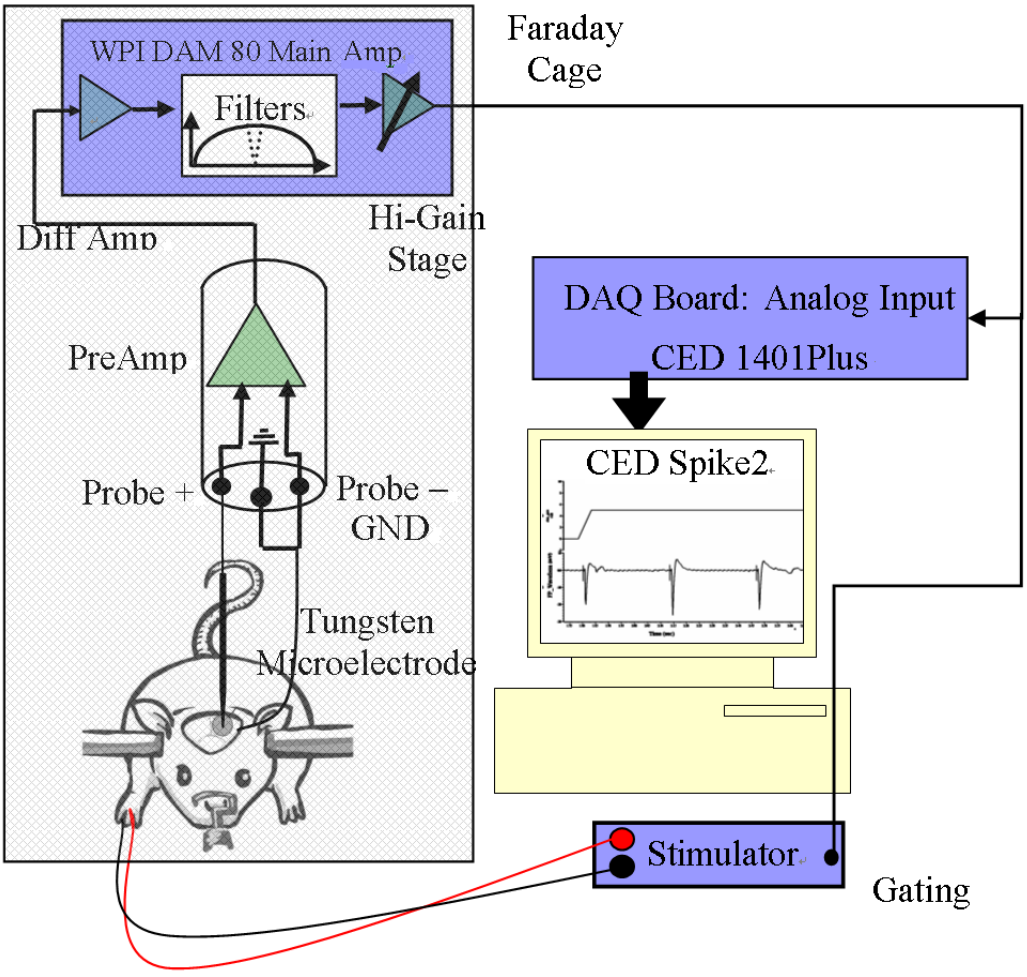


Fig.2-1 A sketch of experiment setup for field potential recording with forepaw peripheral stimulation in rat.

*2.2.1 Materials and methods*

Animal Preparation for brain activation studies: In the following studies, the animal preparation is the very similar and the procedures can be summarized as follows:

Sprague-Dawley rats were initially anesthetized with isofluorane inhalation and an intraperitoneal injection of sodium brevital (150 mg/kg) mixed with glycopyrolate (0.06 mg/kg). The rats were subsequently intubated and mechanically ventilated. The

anesthesia was maintained with isofluorane (0.75-1.0%) in a 2:1 air: $O_2$ mixture. The body temperature was maintained at 36.5 - 37.0 °C using a feedback-regulated heating pad (CMA150, CMA Inc). The right femoral artery was catheterized for blood sampling and blood pressure transduction. The electrocardiogram and arterial blood pressure was continuously monitored (PC-SAM monitor, SA Inc). Arterial pH, $PCO_2$, $SPO_2$ and $PO_2$ were measured periodically (ABL 700, Radiometer Medical), and their values were maintained in ranges of 7.35-7.40 (pH), 35-41 mmHg ($PCO_2$), 97±1% ($SPO_2$) and 115±5 mmHg (MBP), respectively. The rats were positioned in a stereotaxic frame (Stoelting Inc). A small (~ϕ2-3mm) craniotomy was made above the forepaw area (4mm lateral from Bregma [Paxinos, 1982; Xerri, 2005]) using a dental drill cooled with normal saline. After surgery, the anesthesia was switched to α-chloralose. It was induced intravenously first with a single bolus of 50mg/kg and maintained with a 25mg/kg/hr continuous dose during the measurement.

Electrical forepaw stimulation: Fig.2-1 shows the experiment setup for field potential recording with peripheral stimulation. Two stainless steel needle electrodes were inserted under skin between digits 2-3 and 4-5 in the forepaw. Each stimulation trial was composed of negative current pulses of 0.3 msec width and 3mA amplitude repeated at a selected frequency over 10 sec, using the same stimulator. The stimulus frequency was set to 3 pulses/sec and different stimulus currents from 0.5mA to 3mA were tested. For field potential recording, a tungsten electrode (0.5MΩ, ϕ0.127mm, A-M Systems Inc.) was inserted 0.6mm deep into the layer III-IV of the forepaw somatosensory cortex (4mm left from Bregma) [Fabricius, 1997; Silva, 2002], using a 3D micromanipulator (KITE-R, WPI Inc.). Then it was connected to the positive socket of the head-stage pre-amplifier (1×, A-M Systems Inc.). A half–cell pellet electrode was fixed beneath the scalp and connected to the ground of the pre-amplifier. The head-stage output was fed to the main amplifier (DAM 80, WPI Inc.). The amplification was set to $10^3$×, and the low and high cutoff frequencies were set at 0.3KHz and 3KHz to suppress the high frequency 'spike'. The whole animal fixation and the main amplifier were placed in a Faraday cage on an optic table to shield electromagnetic interference. The stereotaxic frame, manipulator, optic table, Faraday cage and the ground outlet of the head-stage were all grounded at a single point. The output of the main amplifier was converted to digital signal by a DAQ module (1401-Plus, CED Inc.) at rate of 20KHz together with the TTL stimulus marker from the stimulator and stored in a PC console installed with the DAQ software (Spike2, CED Inc.).

*2.2.2 Results and discussion*

Fig 2-2 (a) shows the field potential recorded during 10sec stimulus (marked by the TTL gate signal from stimulator). Thus, the 3Hz stimulus pulse train evoked 30 field potential impulses in this trial. Fig 2-2(b) is a magnification of the waveform of one impulse following a stimulus pulse. The 0.3msec wide pulse is an artifact from stimulus. A field potential impulse consists of a negative sharp peak at ~10-20 ms after stimulus pulse followed by a positive overshoot and then recovery to the baseline. The FP impulse lasts ~60-70msec following the stimulus pulse. Fig. 2-2(c) shows the peak amplitude of FP impulse as a function of time during the 10sec stimulation trial. Different curves in Fig. 2-2(c) represent different stimulus currents from 0.5mA to 3mA. The curves show

that weak stimuli (0.5 and 0.75mA) required three pulses to bring the negative peak amplitude to its deepest level, as the stimulus grew stronger (1-2 mA), the deepest peak was reached after two pulses, and strong stimulus (2.5-3mA) evoked the deepest peak immediately after the first pulse. This trend of amplitude is very close to the one generated by the model in Chapter 1 (shown in Fig.1-5(c)), which approximates the change of neuronal activity level accompanying stimulation as the difference between the stimulation profile and an introduced inhibition function using Eq(1-1~4).

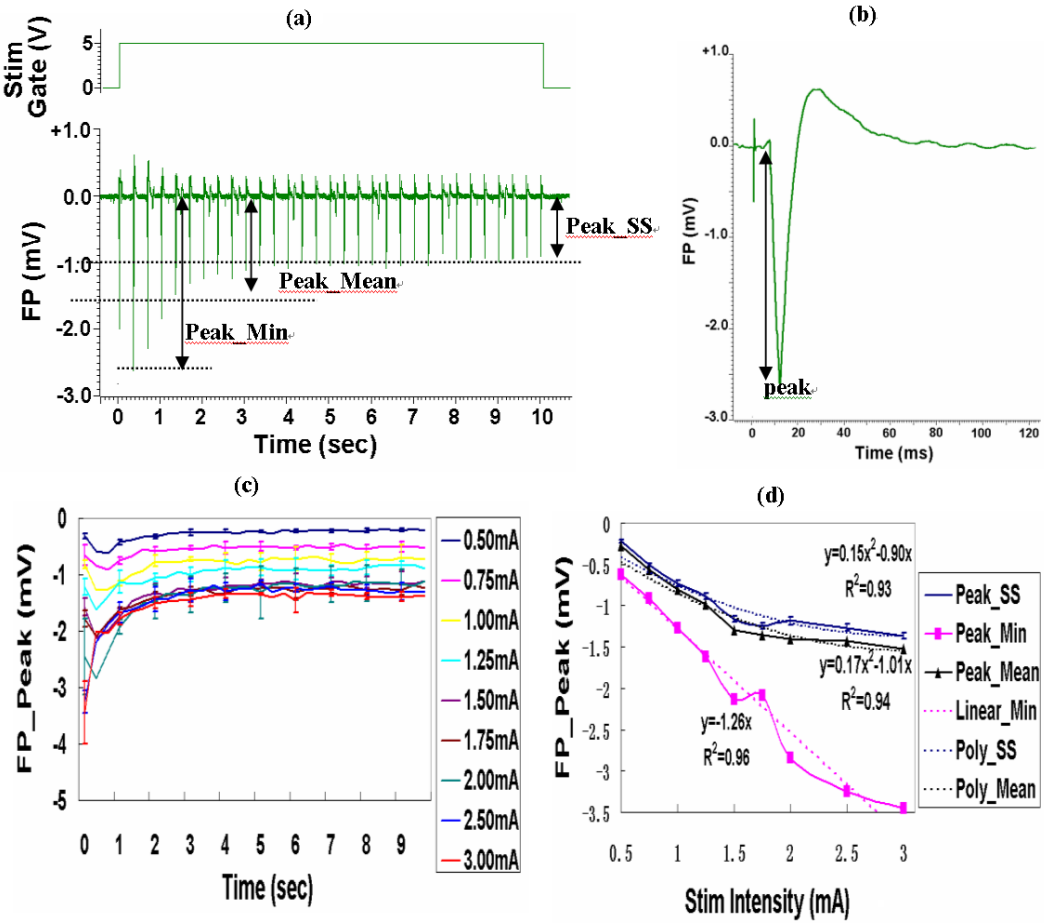


Fig 2-2 (a) A snapshot of field potential recording with 3Hz forepaw stimulation for 10 sec duration, the upper trace is the TTL gate indicating the onset and end of stimulus train. (b) A single impulse of field potential following a stimulus pulse, which is marked by the stimulus artifact (at time 0). (c) the peak amplitudes (negative) of field potential impulse as a function of time during 10 sec stimulus of different current intensities from 0.5 mA to 3mA. The peak amplitude first reaches a deepest level then converge to a steady state level (d) The trend plot of the deepest (minimal), steady state and mean peak amplitudes (as illustrated in (a)) and their fitting functions against different stimulus currents.

As shown in Fig.2-2(d), the deepest peak value ($y$) also linearly decreases (pink curves, $y$=-1.26$x$, $r^2$=0.96) with the stimulus intensity ($x$), from ~-0.62mV with 0.5mA

stimulus to ~-3.45 mV with 3mA stimulus. After the strongest impulse, as more stimulus pulses were coming in, inhibition started to take effect and brought the impulse peak amplitude to a steady state level ($y$) within ~3 sec after the deepest peak, which is consistent with the time constant predicted in modeling back in Chapter 1. This steady state peak amplitude also decreases with the stimulus intensity ($x$). However as shown by the blue curve and the parabolic fitting ($y$=0.15$x^2$-0.9$x$, $r^2$=0.93) in Fig.2-2(d), this trend deflected flatted beyond 2mA stimulus. Thus the steady state level decreases from ~-0.22mV with 0.5mA stimulus to ~-1.36 mV with 3mA stimulus. To compare the overall magnitudes of field potential in response to different stimulus strength, in Fig.2-2 (d), we also include the mean peak level ($y$) averaged over 30 impulses versus stimulus intensity ($x$) and its parabolic fitting curve ($y$=0.17$x^2$-1.01$x$, $r^2$=0.94). As we can see, the overall field potential magnitude increases with stimulus intensity, but the trend becomes flat while the stimulus is greater than 2-3 mA. This guides us to choose stimulus currents of 2-3 mA in the following brain functional studies using fMRI and functional optical imaging in the next sections in order to get maximal but innocuous hemodynamic responses to the forepaw stimulation.

## 2.3 Recording local cerebral blood flow changes evoked by cortical and forepaw electrical stimulation using laser Doppler flowmeter

*2.3.1 Materials and Methods*

Laser Doppler flowmetry can measure relative changes of blood perfusion rate / flow ('flux'), blood volume (in facto concentration of moving red blood cell, assuming constant hematocrit) and mean speed of red blood cells within the illuminated tissue volume. The principle is based on the fact that, due to Doppler effects, moving RBC's in the illuminated tissue volume cause beating in the detected photon current which is proportional to the backscattered light intensity. The frequency ($\omega$) weighted integration of the AC power spectrum, $P(\omega)$ (within the selected bandwidth $\omega_1$~$\omega_2$), of the photon current is used to approximate the relative blood perfusion rate. This is often normalized by the mean square of the DC current $<I_{dc}^2>$ to compensate for laser power variation as expressed by equ (2-1) [Barfod, 1997; Barnett, 1990; Bonner, 1981; Matsuura, 1999; Jones, 2001].

$$flow \sim \frac{\int_{\omega_1}^{\omega_2} \omega P(\omega) d\omega}{< I_{dc}^2 >} \qquad (2\text{-}1)$$

The animal preparation is the same as described in Section 2.2.1.

Direct electrical stimulation in brain cortex: Five rats were used for cortical stimulation, for which the craniotomy was made above the left hindpaw area within the right somatosensory cortex (1-mm posterior and 2 mm right from Bregma [Paxinos, 1982]). The stimulation electrode was inserted through the cranial window to a depth of 1.5 mm [Fabricius, 1997; Silva, 2002] with an inclined angle to make room for mounting optical probe and minimize blocking of light path. The electrode is composed of a nickel-chromium wire ($\phi$ ~80 μm) with the shaft part insulated by a glass pipette. Then the circuit was closed by grounding a needle inserted subcutaneously. The cortical stimulation was performed using a pulse train stimulus paradigm (Isolated Pulse

Stimulator 2100, A-M Systems). The stimulus train consists of negative current pulses of 0.1ms width applied at 100Hz over 50ms followed by 150ms rest. This pattern was repeated five times per second for each 6-sec trial. And 4min resting was allowed between two trials to let LCBF recover to the baseline. The pulse amplitudes were switched from 0.1 to 0.4mA at interval of 0.05mA (negative) in random order for different trials to examine the dependence of the LCBF responses on stimulus intensity.

Electrical forepaw stimulation: Five rats were used for forepaw stimulation, for which the craniotomy was made above the forepaw sensory cortex area (4mm lateral from Bregma [Paxinos, 1982; Xerri, 2005]). Two stainless steal needle electrodes were inserted under skin between digits 2-3 and 4-5 in the forepaw to deliver stimulation pulses. Each stimulation trial was composed of negative current pulses of 0.3 msec width and 3mA amplitude repeated at a selected frequency over 6 sec, using the same stimulator. The stimulation frequency was randomly selected from 2, 3, 4, 5 Hz from trial to trial to avoid possible adaptation of the rat brain to a given frequency.

A commercial near-infrared laser Doppler flowmeter (MoorLab, $\lambda$=785 nm, P~1.6mW, Moor Instruments) was used for this experiment. The bandwidth ($\omega_1$~$\omega_2$ in equ (2-1)~(2-3)), which was 20~15kHz in our setup, provides a linear dynamic range for the speed roughly between 0~10 mm/s [Bonner, 1981; Lindsburg, 1989; Skarphedinsson, 1988]. Fig.2-3(a, b) show the experimental setup. A fiber optical probe (MP3, Moor Instruments) with one emission fiber and two detector fibers, was vertically mounted above the exposed cortical surface, with particular care to avoid compressing underlying brain tissues and vessels [Tenland, 1982].

The local cerebral blood flow, red blood cell concentration and RBC speed was continuously recorded and stored in the PC using MoorLab software. The baseline fluctuations were considered as artifacts due to heartbeats or other rhythmic motions, thus were filtered out by a lowpass filter (cutoff frequency =1 Hz) [Tenland, 1982; Vongsavan, 1993]. The 10 second period prior to the stimulation was defined as baseline (100%), and the obtained data are presented as a relative change normalized by the baseline. For a given stimulation current, the data was averaged cross the trials and animals and presented as mean ± SEM.

Fig.2-3 (c) illustrates the parameters to be extracted from the CBF measurement for analysis, which includes: 1) Peak response (PR), defined as the maximal amplitude of the relative CBF; 2) Mean response (MR), defined as the amplitude averaged across the half maximum waist of the relative CBF; 3) the delay to half peak (DHP), defined as the latency from stimulus onset to the first half maximum point; 4) the delay to peak response (DP), defined as the latency from stimulus onset to the peak response; and 5) the half maximum width of the response (HMFW), defined as the duration of the half maximum waist. Fig.2-3 (c) illustrates how these parameters will be extracted from the CBF time course.

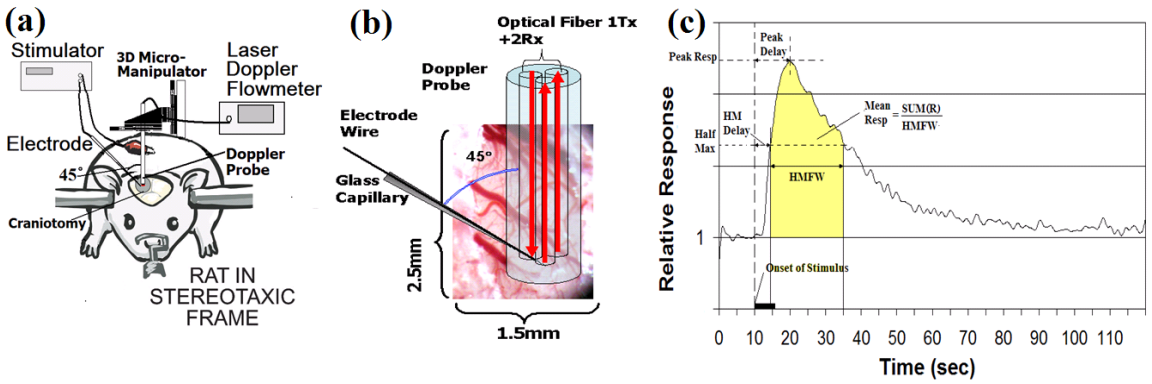


Fig.2-3 (a) A sketch of experiment setup for direct cortical stimulation and laser Doppler flowmetry of rat brain *in vivo*. (b) placement of LDF probe and stimulation electrode at the craniotomy site (c) The definitions of the characteristic parameters (HM-Delay, Peak_Delay, HMFW, Peak_Resp and Mean_Resp) on the temporal profile of LCBF response. The 6 sec stimulation was marked by the black bar.

*2.3.2 Results and discussion*

LCBF response to the direct cortical stimulation: Fig.2-4 (a) shows a typical example of the cortical blood flow response to direct electrical stimulation. Each occurrence of the stimulation was marked on the LDF recording trace. Fig.2-4(b) shows the averaged time course of the LCBF changes in response to 6-second cortical stimulation with various stimulus currents of 0.1, 0.2, 0.3 and 0.4mA. The LCBF rises to half maximal level within 4~5 sec following the onset of direct electrical stimulation, and reached the maximum peak within another 8-10 seconds. From the peak, it started a slow decline till fully recovering to the baseline. For instance, it took 60~70 seconds for LCBF to return from peak to baseline when the stimulus current was over 0.2mA, which was as long as 10 folds of the 6 sec stimulus period. In addition, it can be seen that both the amplitude and the duration of the LCBF response increased along with increases in the applied stimulation current. Fig.2-4 (c)~(e) summarizes the LCBF amplitude and duration as a function of the stimulus current. As shown in Fig.2-4 (c), both the peak response (PR) and the mean response (MR) of the LCBF increased linearly with the increase in stimulus current: Peak Response (PR) increased from (128±2)% to (170±4)% (PR=(124*I+119)%, r=0.94) along with the increase of the stimulus current from 0.1 mA to 0.4mA, and MR increased was from (119±2)% to (151±4)% (MR=(100*I+110)%, r=0.97). Fig.2-4 (d) shows the relationship between the LCBF response duration, i.e. HMFW defined above, and the stimulus current. For the 6-secord stimulus, the half maximal width of the LCBF response (HMFW) increased significantly from 8.3 ±1.0 sec to 23.7 ±1.7 sec along with the increase in the stimulus current from 0.1 mA to 0.3 mA, then following by a slight increase to 5.6 ±2.8 sec when the stimulus current was further increased to 0.4mA. Fig.2-4 (e) illustrated the latency of the LCBF signals (both delay to the peak (DPK) and delay to the half maximum (DHM)) relative to the stimulation onset as a function of the stimulus current. The DHM was between 4~6 seconds, while the DPK was 8~10second in response to the stimulation currents varied between 0.1 to 0.4 mA.

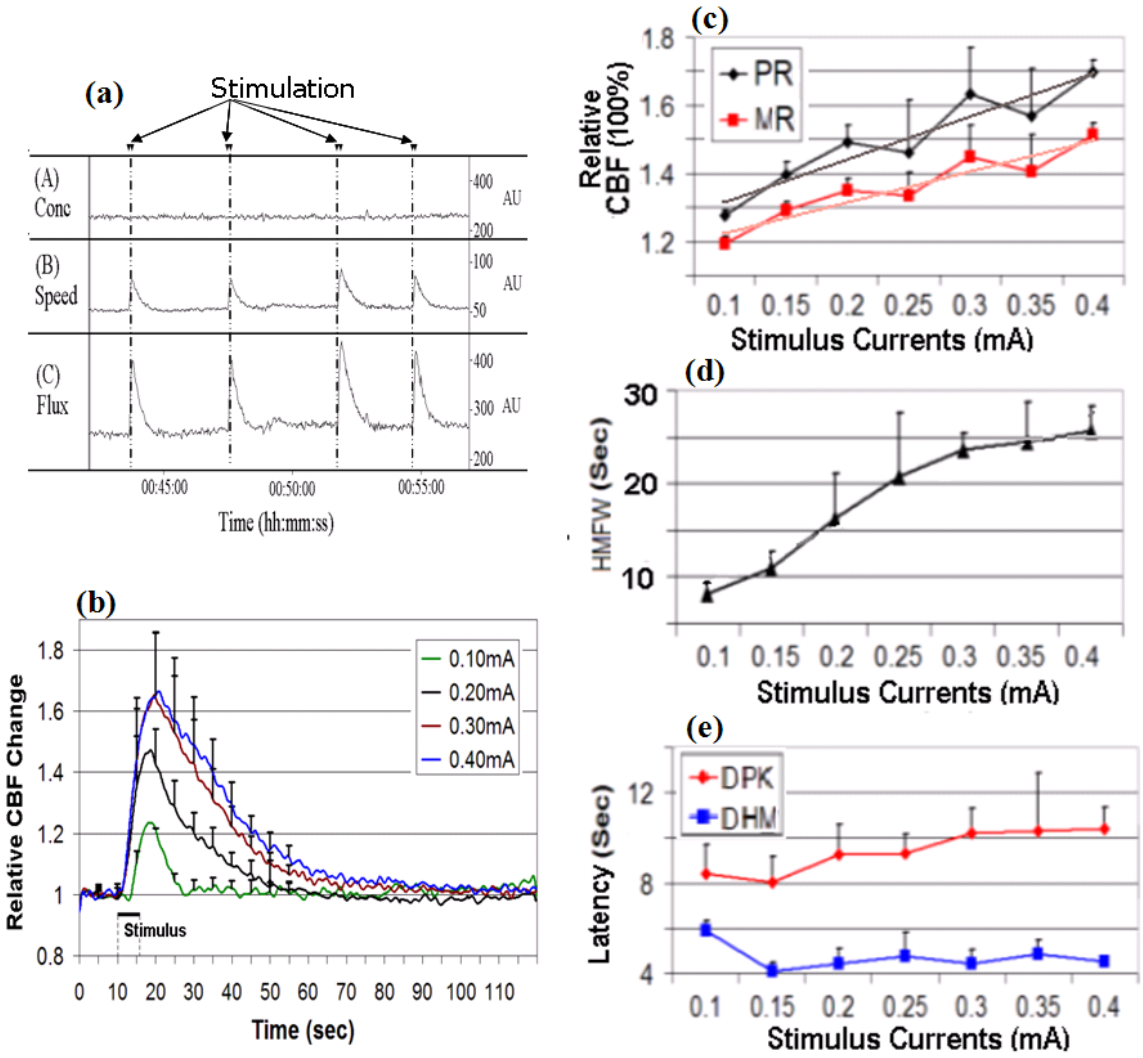


Fig.2-4 (a) A snapshot for LDF acquisition of RBC concentration, cerebral blood speed and flow ('flux') over four stimulus trials conducted in cortex. All the data are in arbitrary unit (AU). (b) The averaged LCBF response to different stimulus amplitudes delivered to cortex. The errors bars represent standard deviations. (c)LCBF peak response at (PR=1.24×I+1.19, r=0.94) and mean response (MR=1.00×I+1.10, r=0.97) during half maximal width vs. stimulus intensities (I). (d) HMFW of LCBF response profile vs. stimulus intensities. (e) Latency of peak (DPK), and half maximal (DHM) response relative to stimulus onset vs. stimulus intensities.

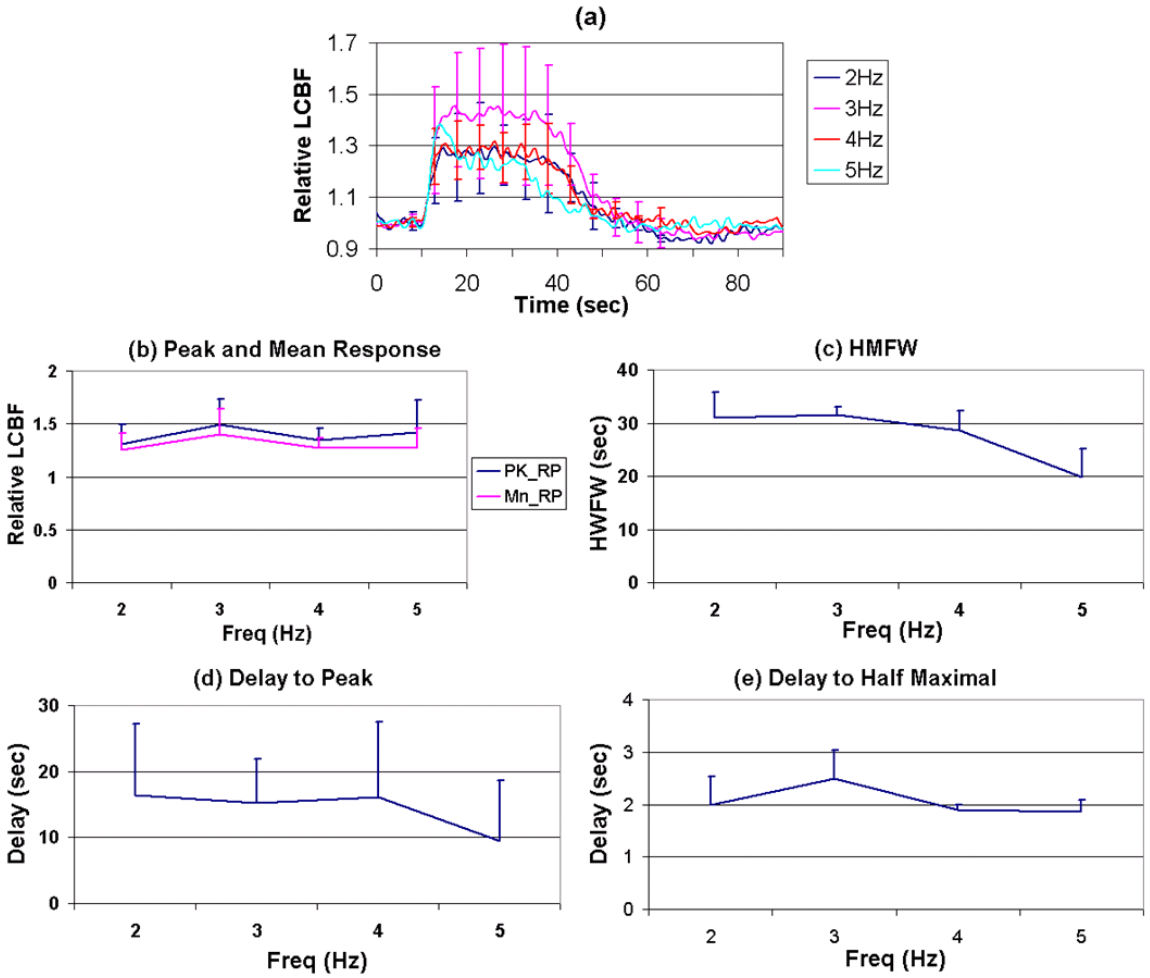


Fig 2-5 (a) The averaged LCBF response to different stimulus frequency applied to forepaw. The errors bars represent standard deviations. (b)LCBF peak response at and mean response across half maximal full width vs. stimulus frequencies. (c) HMFW of LCBF response vs. stimulus frequencies. (d) Latency of peak (DPK), and (e) first half maximal (DHM) response relative to stimulus onset vs. stimulus frequencies.

LCBF response to the forepaw electrical stimulation: Fig. 2-5 (a) shows the averaged (± stdev) time courses of LCBF in responses to 6 sec of peripheral forepaw stimulation with various frequencies from 2 to 5 Hz and pulse magnitude of 3mA. In terms of response magnitude (as shown in Fig. 2-5 (b)), stimulus of 3 Hz elicited greatest peak (~50%) and mean increase (~40%) across the HMFW. There was no significant increase of LCBF while the stimulation frequency was higher than 5Hz. The response duration is estimated by using the full width of half maximum of the LCBF signals. As shown in Fig2-5 (c), stimulus of 2-4 Hz retained a prolonged and relatively flat plateau (~30 sec) after the ending of stimulus while the 5Hz stimulus provided a much shorter plateau (~20 sec) following a initial high peak. This difference of temporal profile with stimulus frequency was confirmed by looking at the latency from the stimulus onset to the maximum (as shown in Fig2-5 (d)). While 2~4Hz show no significant difference in their latency to maximum, the latency with 5Hz to its initial peak is significantly shorter

than others. However, their early risings to the half maximal height again show no difference in their latency from the stimulus onset. Hereon, we would use 3Hz stimulus for most of our stimulation experiments including field potential recording, BOLD-fMRI and LDSCI measurement, as supported by this studies and similar results previously reported [Ureshi, 2004].

## 2.4 Simultaneous recording of local changes in cerebral blood volume, blood oxygenation and fluorescence-labeled calcium signals in response to peripheral electrical stimulation

### *2.4.1 Materials and methods*

ODF system: Fig.2-6(A) shows a systematic diagram of the multi-wavelength ODF probe designed to detect the changes of the local CBV, StO2 and $[Ca^{2+}]_i$ from the surface of the brain. It consisted of a 150-W Xenon lamp; a monochromater (Mono-Ex) and the photon detectors for fluorescence (PMT-F) and diffuse reflectance (PMT-A). The lamp was connected to a computer-controlled monochromater to select the incident wavelengths of 548nm, 555nm and 572nm by time-sharing to sequentially deliver the light at these wavelengths onto the brain surface through one arm of a Y-shape bifurcated fiber-optic bundle. The calcium-dependent fluorescence and diffusive reflectance from the brain tissue were collected by the fiber tip of the common leg and detected by the photon detectors of PMT-F and PMT-A accordingly. The changes in CBV and StO2 could be separately distinguished from the reflectance measured by summing and subtracting the optical densities of the signals at 555nm and 572nm (i.e., symmetric wavelengths to the hemoglobin isosbestic point. The signals are digitized and stored in a personal computer for data processing. The ratio of $Ca^{2+}$ fluorescence emission at 589nm over re-emitted excitation reflectance at 548nm represents the calcium-dependent fluorescence with a minimum influence of physiological interference. As the fluorescence technique can track intracellular calcium ($[Ca^{2+}]_i$) changes which are directly associated with neuronal activity, we conducted the simultaneous measurements of CBV, StO2 and $[Ca^{2+}]_i$- fluorescence to examine the feasibilities of our ODF probe to optically dissect the cellular and vascular events in the evoked functional hyperemia.

For ODF measurements, the surgical preparation and anesthesia on the rats is similar to the procedure described for the field potential recording.

In-vivo loading of fluorescent dye (Rhod2(AM)): In the following experiments, animal preparation is the same as being described in Section 2.2.1. In addition the cortical areas of the animal brain were labeled in vivo using the fluorescence calcium indicator Rhod2 (AM). 50μg of Rhod2(AM) (Molecular Probes, Eugene, OR, USA) was dissolved first in 2μl dimethysulfoxide (DMSO) and then diluted in 440μl distilled water at a room temperature. A 30-G needle attached to a stereotaxic micromanipulator was inserted into the cortex (~1.2-1.5mm beyond the surface) with a certain angle (~30-45°). The Rhod2 solution of 100μl was infused into the brain at a perfusion flow rate of 3μl/min using a microinjection pump (CMA/100, Carnegie Medicine, Stockolm, Sweden). Afterwards, 60-80 mins was allowed for Rhod2 to be hydrolyzed by intracellular esterases to become membrane-impermeable calcium-binding indicators.

Forepaw electrical stimulation was performed using two needle electrodes, inserted under the skin of the left forepaw in the space between digits 2 and 3, and another between digits 4 and 5. The stimulus was generated by a current source (Isolated Pulse Stimulator 2100, A-M Systems). Fig. 1C shows the stimulus paradigm. The stimulus frequency was set to 3 Hz with 2-3 mA currents. Stimulus durations were 30 sec.

For detecting CBV, $StO_2$, $[Ca^{2+}]_i$- florescence from the cortex of the rat, the optical fiber tip was placed in contact with the cortical surface as shown in Fig. 1A. The interface between the fiber optical tip and the brain was filled with transparent gel (Surgical Lubricant Sterile Bacteriostatic; NY) to reduce the mismatch in refractive index between fiber, air and brain tissue, thus minimizing the specular reflection from the surface of the brain. All CBV, $StO_2$, $[Ca^{2+}]_i$ changes were expressed as a percentage of the baseline ±SEM.

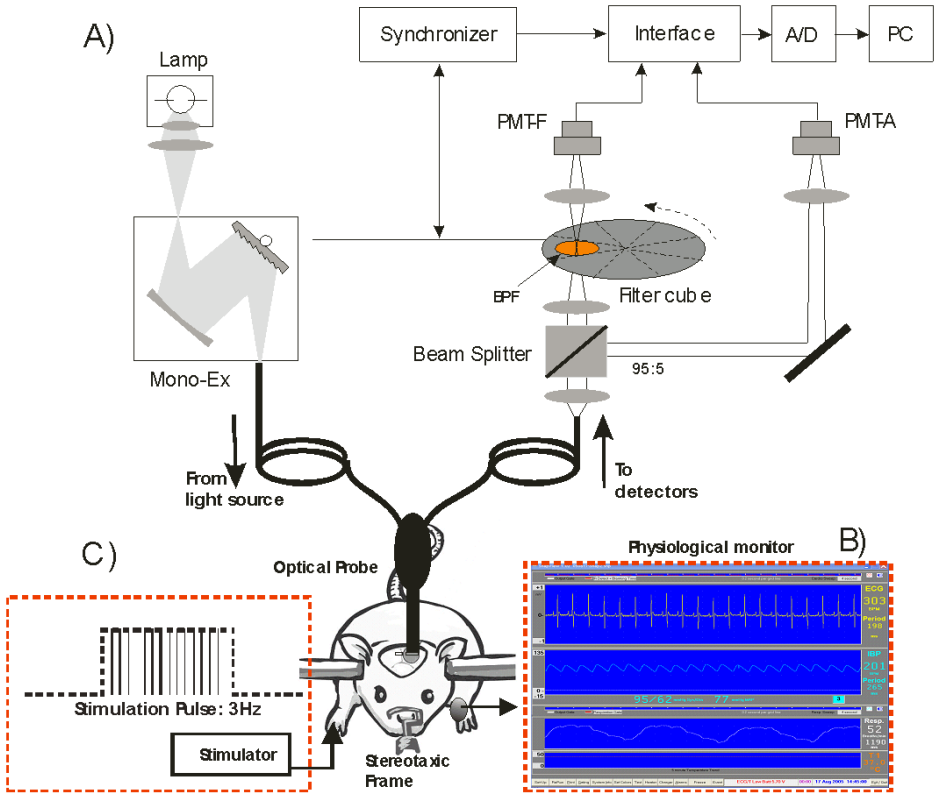


Fig 2-6 A). Diagram of ODF probe used for detecting the changes in CBV, $StO_2$ and $[Ca^{2+}]_i$ fluorescence from the cortical brain of the rat; B). An example of a real time physiological monitor during the in vivo experiments; C). Paradigm of electrical stimulation of forepaw to induce a somatosensory response of the rat brain.

*2.4.2 Results and discussion*

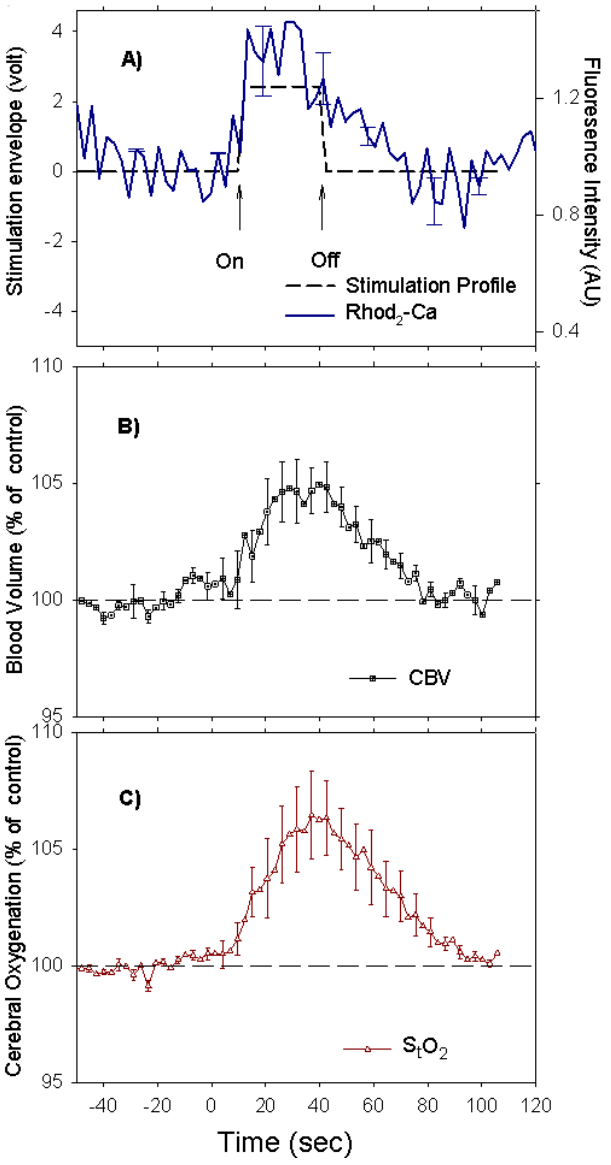


Fig 2-7 Changes in $[Ca^{2+}]_i$ fluorescence of Rhod2 (A), cerebral blood volume (B) and oxygenation (C) obtained from the living rat brain in response to electronic forepaw stimulation (3Hz, 3mA).

Fig. 2-7 shows the changes in CBV, $StO_2$ and $[Ca^{2+}]_i$ fluorescence of the somatosensory response to the forepaw stimulation. The stimulation profile is superimposed on the time-course of $[Ca^{2+}]_i$ fluorescence as shown in Fig.2-7(A). CBV and StO2 changes induced by forepaw stimulation are shown in Fig. 2-7(B, C), respectively. As can been seen, the forepaw stimulation induced ~40-50% increase in [Ca2+]i fluorescence. Concurrent increases of ~ 3-6 % in CBV and StO2 were also observed, respectively. These results demonstrate the proof-on-concept of our ODF probe can be used to separately distinguish the multi-parameters and track changes of $[Ca^{2+}]$i, CBV, $StO_2$ in the live brain during functional activation, thus extended the capability of the current technologies such as MRI and DOT for brain functional studies.

It was clearly more challenging to integrate the detection of these three parameters into one measurement. For instance, to minimize effects of hemoglobin oxygenation changes on the Rhod2 excitation and emission, we selected a pair of isobestic wavelengths for excitation (e.g., 548nm) and fluorescence emission (e.g., 589nm). Also, the ratio of Rhod2 fluorescence at 589nm over the re-emitted excitation at 548nm was used to eliminate the influence of the absorption and scattering changes within the tissue on the [Ca2+]i fluorescence signal.

To detect changes in CBV and StO2, we measured the diffusive reflectance from the brain at the additional two wavelengths of 555nm and 572nm, which coincided with the absorption band of oxy- and deoxy-hemoglobin, and changed with the same amplitude but

in opposite directions corresponding to the hemoglobin oxygenation changes. This approach was pioneered by Chance et al. [Chance, 1962; Chance, 2003] and theoretically extended and experimentally validated continually [Du, 2001; Nioka, 1997; Culver, 2003].

These preliminary results demonstrated that the ODF probe can be used to detect the fluorescence emission and diffuse reflectance from the brain surface based on the concept of time sharing at multiple wavelengths. This approach may open new opportunities to study the functional activations in normal or disease brains.

### 2.5 Design of LSCI system and in-vivo mapping of local cerebral blood flow changes evoked by peripheral electrical stimulation

#### *2.5.1 Materials and Methods*

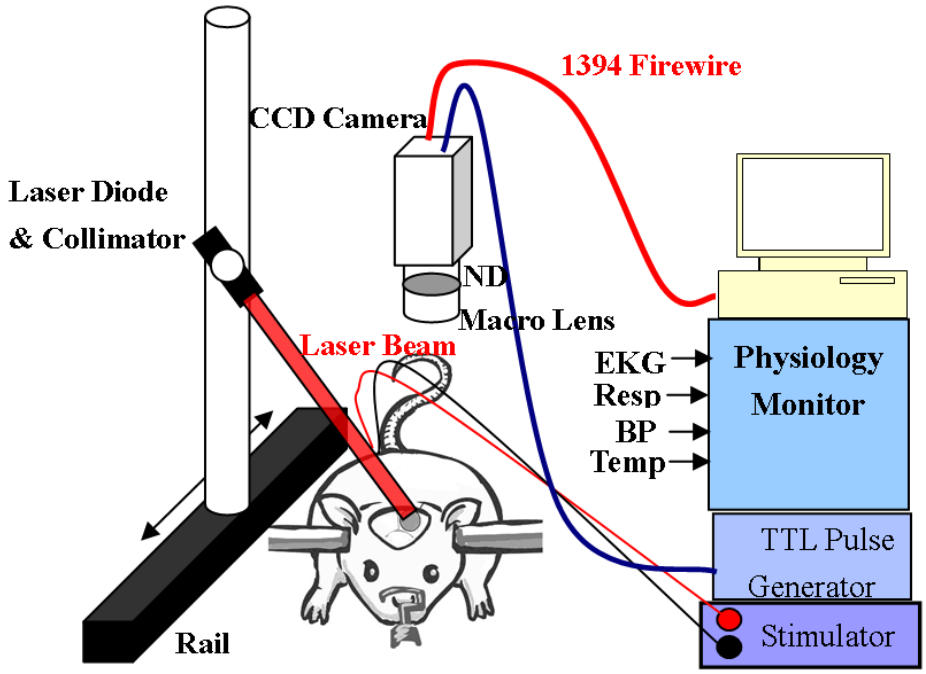


Fig. 2-8 LSCI setup for imaging cortical LCBF response to hindpaw stimulation in rat. (ND: neutral density filter)

Development of LSCI system: For acquiring laser speckle images, a NIR laser diode (HL851G, λ=785nm, mono-mode, $P_{max}$= 50mW, Hitachi) driven by a constant power supplier (LT220P-B, Thorlabs) was used as illuminator. The laser beam was collimated (LD1100, Thorlabs) onto the exposed brain surface at an angle of 30° from the normal. A monochromatic CCD camera (Retiga-Ex, Qimaging) with a quantum efficiency of ~45% at 785 nm wavelength and pixel size of 6.45μm was installed upright above the cranial window. For LSCI, it is important to match speckle size to pixel size so that speckle contrast can be easily calculated. Therefore, a close-up lens (Nikon, f=105mm) was used with 1/F# set at 2.8 and magnification at 1:1, assuming

all optic aberrations can be ignored. The exposure time of the camera was set at 10 ms. The exposure was triggered by external TTL pulses and image series was transported to a PC via 1394 interface. The diagram for LSCI system and in-vivo experiment setup is illustrated in Fig.2-8.

For imaging LCBF response to neuronal activation in somatosensory cortex, we used the same surgical and anesthesia procedure described for the field potential recording.

Similarly to the forepaw stimulation, the electrical stimulation of hindpaw was conducted by inserting two electrodes under skin into the left hindpaw between 2nd-3rd and 4th-5th digits. The stimulus consisted of a 10 sec train of rectangular current pulses, with pulse amplitude of -2 mA, pulse duration of 0.3 msec and different repetition frequencies of 1, 2, 3 and 5 Hz. The speckle images was capture at 3 frames per second over a period 20 sec before,10sec during and 20sec after the stimulation. Thus a total of 150 frames were acquired in each stimulation trial.

Data Processing for LSCI: The post-processing of LSCI dataset is illustrated by Fig.2-9. To extract blood flow information from those speckle images, first, a sliding window of 5*5 pixels was moved over each individual frame and a speckle contrast map ($K$) was calculated for each frame using the following definition.

$$K = \frac{\sigma}{< I >} \tag{2-2}$$

where $\sigma$ and $<I>$ stand for, respectively, the standard deviation and the mean value of the pixel intensity in that window at each sliding step. This windowed operation results in a nominal resolution of 5*6.45≈32.2μm. The speckle contrast $K$ has been proved to relate to the ratio between the correlation time ($\tau_C$) of the speckle intensity fluctuation here at the CCD sensor and the exposure time ($T$) of the camera [ Briers, 1996; Brier, 2001; Durduran, 2004]. This relation can be defined by equ (2-3) and shown in Fig.2-9 (c).

$$K^2 = \frac{1}{2}\left(\frac{\tau_C}{T}\right)^2\left[\exp\left(-\frac{2T}{\tau_C}\right) - 1 + \frac{2T}{\tau_C}\right] \tag{2-3}$$

$(T/\tau_C \to \infty,\ K \to 0;\ T/\tau_C \to 0,\ K \to 1)$

Furthermore, the correlation time $\tau_C$ is inversely proportional to the root of mean square (RMS) speed of the scattering particles ($<v^2>^{1/2}$), which is noted as equ (2-5).

$$\tau_C = \frac{1}{ak < v^2 >^{1/2}} \tag{2-5}$$

where $k$ is the wave-number of the original incident light and $a$ is a complicate unit-less factor related to the speed distribution and the scattering properties of the medium. Therefore, with exposure time $T$ and wavenumber $k$ usually known for an experiment, the speckle contrast $K$ can be rewritten, as equ (2-6) show, a function of solely $a<v^2>^{1/2}$, which is a linear index of blood cell speed assuming a constant $a$ in the given pixel.

$$K^2 = \frac{\exp\left(-2Tak<v^2>^{1/2}\right) - 1 + 2Tak<v^2>^{1/2}}{2\left(Tak<v^2>^{1/2}\right)^2} \tag{2-6}$$

As we plot out this formula as shown in Fig.2-9(c), we see that $K$ value ranges only from zero, which corresponds to scattering particles with very high speeds, to one, which indicates no motion.

Although it is not easy to directly calculate $a<v^2>^{1/2}$ given a $K$ value, we have established a lookup table of $a<v^2>^{1/2}$ which can be easily indexed by $K$ value. Unlike in previous LSCI method [Durduran2004; Dunn2003; Dunn, 2005], where contrast was directly used as nonlinear and reverse indication of flow speed, our calculation so far would provide a time series of mapping of positive indices for the flow speed.

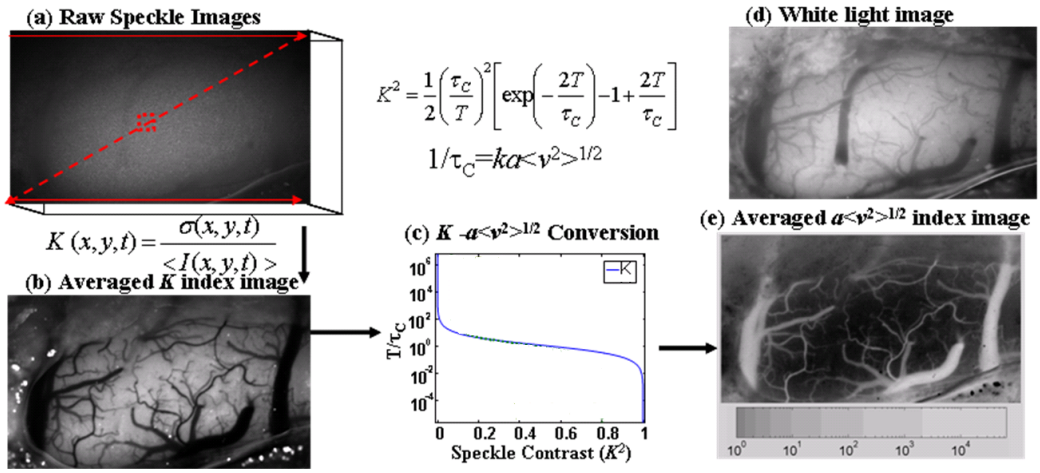


Fig. 2-9 (a) raw laser speckle image of the cortex (b) averaged speckle contrast image, (c) speckle contrast ($K$) as a function of the ratio $T/\tau_C$. (d) white light image, (e) averaged flow index image, which was rendered in logarithm scale to enhance the vascular contrast.

To detect the statistically significant change accompanying stimulation, both t-value between resting period $I_c$ and stimulation period $I_b$ and the correlation coefficients $cc$ (and their associated $p$-values) of the stimulus profile $I_s(nt)$ (shown as the black-curve in Fig.2-7(e)) with the time series of flow index $I_f(nt)$ was calculated for each pixel as equations (2-7 and 8) respectively.

$$t = \frac{\langle I_c \rangle - \langle I_b \rangle}{\sqrt{\frac{S_c^2(n_c - 1) + S_b^2(n_b - 1)}{(n_c - 1) + (n_b - 1)}\left(\frac{1}{n_c} + \frac{1}{n_b}\right)}} \tag{2-7}$$

Where $<I_b>$, $S_b$, $<I_c>$ , $S_c$ stand for the mean and standard deviation of flow index during the baseline and challenged period, and $n_c$, $n_b$ stand for the number of frames acquired during baseline and challenged period.

$$cc = \frac{\sum_{n=0}^{N}(I_f(nt) - < I_f >)(I_t(nt) - < I_t >)}{\sqrt{\sum_{n=0}^{N}(I_f(nt) - < I_f >)^2 \cdot \sum_{n=0}^{N}(I_t(nt) - < I_t >)^2}} \quad (2\text{-}8)$$

Where $< I_f >$, $< I_s >$ stand for the mean of flow index series $I_f(nt)$ and stimulus profile $I_s(nt)$, respectively.

With both *cc* and *t* measures, the pixels with the associated *p*-value below 5% threshold were collected as the activated region, otherwise the pixel would be masked later analysis. The mean LCBF time course for the activated region was obtained by normalizing the time course of each pixel to its pre-stimulation baseline and then averaging over all pixels in that region. Moreover, to demonstrate the spatiotemporal dynamics in response to cocaine challenge, the relative change against the baseline average was color-mapped onto the activated region on each frrame, thus sequentially forming a video clip of th local hemodynamic change.

### *2.5.2 Results*

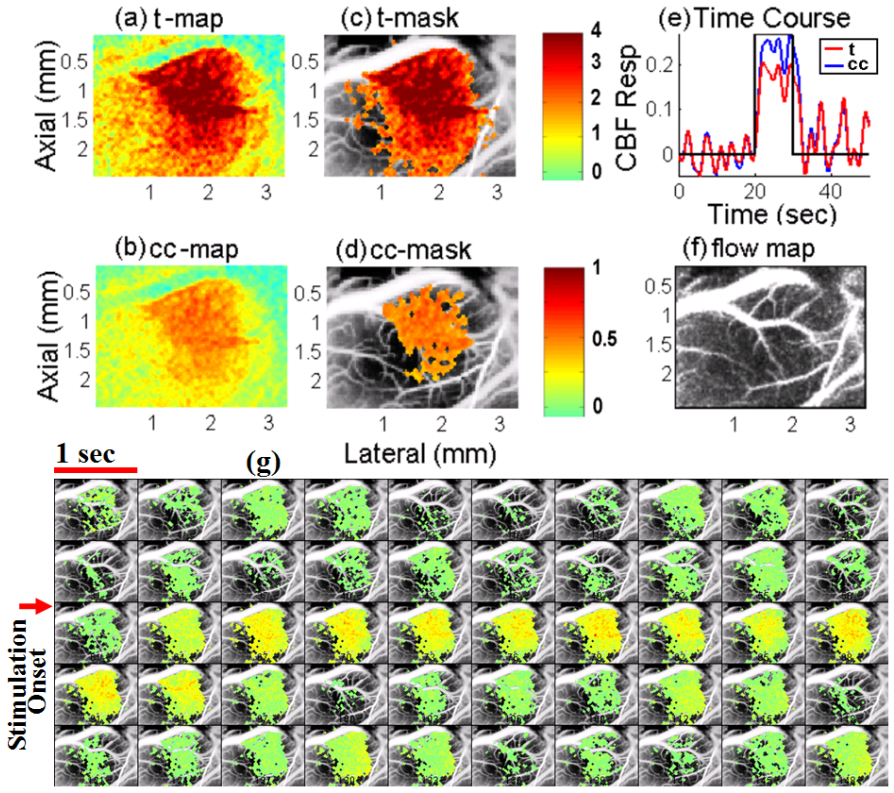


Fig.2-10 Cortical LCBF response to hindpaw stimulation (a) pseudo-color mapping of t-value between resting and stimulation period, (b) masked mapping of t-value after thresholding, beside the color-table (c) mapping of correlation coefficient with stimulation profile. (d) masked mapping of correlation coefficient after thresholding, beside the color-table. (e) averaged LCBF time course from regions with significant increase

approved by t-test (as high lighted in (b)) and correlation coefficient (as high light in (d)), respectively. (f) averaged map of cortical vasculature and flow index from LDSCI. (g) the t-masked mapping of percentage change against baseline in each individual pixel over the resting and stimulation period at 1 sec interval.

Fig.2-10.(b) and (d) show a typical example of masked maps of the t-value and correlation coefficient *cc* indicating region with significant LCBF increase evoked by hindpaw stimulation, respectively, and superimposed on the flow index image. It shows that the centroid of the activation region is 1.2 mm posterior and 1.8 mm right from the Bregma, which is consistent with the hindpaw sensory cortex location in atlas [Paxinos, 1998]. The pixel-wise percentage change over baseline as a function of time is color mapped in Fig.2-10(g), which indicates the LSCI system can be used to capture the brain activation with both high temporal and spatial resolution.

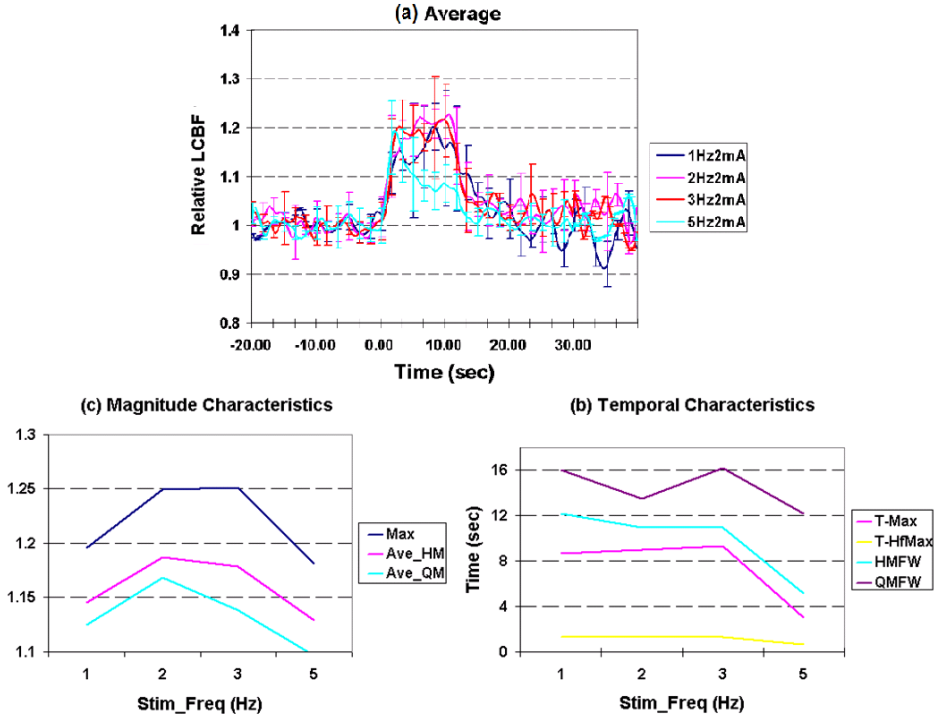


Fig.2-11 (a) Inter-subject mean (±std) time courses extracted over the activated area selected by t-test vs different stimulus frequencies (1, 2, 3, 5Hz) but with identical pulse magnitude of 2mA. (b) Magnitude and (c) temporal characteristics of those averaged time courses vs different frequencies (1, 2, 3, 5Hz). (Max: maximal value of time course, Ave_HM: average value across the full width of half maximal, Ave_HM: averge value across the full width of one quater of the maximal; T-max: the time latency from stimulus onset to the maximal point, T-HfMax: the latency from

stimulus onset to the first half maximal point, HMFW: full width of half maximal, QMFW: full width of one quarter of maximal).

To compare LCBF responses to different stimulation frequencies, we averaged the time courses across the four rats for each stimulus frequency applied and plotted in Fig.2-11 (a). It is shown that the maximal response were observed at the stimulation frequencies of 2 and 3Hz, but decreased significantly at 5Hz. Other than comparison of this single maximal value, we also averaged the time courses across the full width of half maximal waist and one-quarter waist of the maximal, which more evidently show that greatest response was evoked by 2Hz stimulus whereas slightly lower at 3Hz. On the other side, it is shown that 5Hz evoked a response rising and falling faster than that lower frequencies does by comparing the time latency from stimulus onset to either the maximal point or the first half maximal point and the full width of half maximal (Fig.2-11(b)). However, we didn't observe any significant response using 8Hz stimulus from all the experiments, suggesting a refractory period is entered when applying higher frequency stimulus.

### *2.5.3 Discussion and conclusion*

These preliminary results indicate that the LSCI system we developed allows us to study the functional hyperemia in somatosensory cortex elicited by electrical hindpaw stimulation with a high tempo-spatial resolution. These preliminary results indicate that LSCI system we developed allow us to study the functional hyperemia in somatosensory cortex induced by electrical hindpaw stimulation with a high tempo-spatial resolution. The observed spatiotemporal profiles of the LCBF response are in good agreement with studies using fMRI and LDF [Duong, 2000; Kim, 1995; Kwong, 1992]. However, the peak magnitude of LCBF response to peripheral stimulus measured by LSCI was much lower than LDF measurement. The discrepancy between LDF and LSCI measurement has been reported and discussed previously in other LSCI studies of sensory stimulation [Durduran, 2004], hypercapnia [Kharlamov, 2003] and optical nerve head [Yaoeda, 2000]. It was speculated that the difference can be more likely attributed to different depth sensitivity rather than blaming the linearity of LSCI technology. This is because LSCI is only sensitive to the superficial flow within 0.3mm below the cortical surface [Kohl, 2000], whereas LDF ($\lambda$=785nm) is more sensitive to flow located deeper down to layer IV [Fabricius, 1997; Bonner, 1990].

In summary, compared to other functional imaging modalities such as fMRI, PET, SPECT, LSCI allow us to study the functional hyperemia in cortex in response to functional challenges with a superior spatial resolution of ~30μm. By combining this technique with electrophysiology, PET, MRI and ODF, we can achieve better comprehension of brain function as well as the related diseases.

## 2.6 Summary

In this Chapter, we presented the animal models and electrophysiological/optical techniques to detect the neuro-vacular responses in the brain cortex of rats evoked by somatosensory stimulation. Each of these methods has its own specific advantage and disadvantage. Field potential recording can directly and precisely track the energy-consuming post-synaptic events during neuronal activation, thus can serve as a good

reference for measuring the neuronal activity and assessing the coupling between neuronal activation and metabolic and vascular response. However, this electrophysiology approach lacks spatial resolution or need costly electrode array and complicate algorithms to cover a large brain region and resolve spatial information. Laser Doppler flowmeter can invasively detect functional hyperemia in real time and with high sensitivity, whereas spectroscopy based optical diffusion and fluorescence probe can simultaneously measure vascular, metabolic and cellular ionic responses to neuronal activation. However, both LDF and ODF can only provide a 'point' measurement; in other words, there is no spatial resolution. In contrast, the LSCI system can provide relative LCBF change superimposed on a high resolution, high contrast vascular image and mean while can attain high temporal resolution up to video rate if necessary. The simplicity and attractive features of LSCI trigger our endeavor to convert it into a quantitative flowmetry and also to use it as a platform to accommodate multi-wavelength illumination for simultaneous flowmetric, oxymetric and/or fluorometric imaging, which will be the stories in chapter 4 and 6.

Nevertheless, all of these techniques are used to detect the brain activation in the superficial area of the cortical brain. To detect neuronal activation throughout the whole brain, we will also use fMRI to detect the blood-oxygen-level-dependent (BOLD) signal changes in response to the electrical forepaw stimulation, which will be described in chapter 3. As described in Chapter 1, BOLD based fMRI signal is a mixture of oxygenation and vascular responses. Therefore, the different aspects of functional hyperemia resolved by optic method here along with the previously laid out biophysical modeling could assist us in more context-aware interpreting of the fMRI measurement in the subsequent chapter.

## 2.7 List of References


2-1) Ances BM, Greenberg JH, Detre J. Laser Doppler imaging of activation-flow coupling in the rat somatosensory cortex. NeuroImage. 1999, 10): 716.

2-2) Austin VC, Blamire AM, Grieve SM, O'Neill MJ, Matthews PM, Sibson NR. Difference in the BOLD fMRI response to direct and indirect cortical stimulation in the rat. Magn Reson Med. 2003, 49: 838.

2-3) Barfod C, Akgoren N, Fabricius M, Dirnagl U, Lauritzen M. Laser-Doppler measurements of concentration and velocity of moving blood cells in rat cerebral circulation. Acta Physiol Scand. 1997, 160(2): 123.

2-4) Barnett NJ, Dougherty G, Pettinger SJ. Comparative study of two laser Doppler blood flowmeters. J Med Engin Tech. 1990, 11(6): 243.

2-5) Bonner R, Nossal R. Model for laser Doppler measurements of blood flow in tissue. Appli Optics. 1981, 20(12): 2097.

2-6) Bonner R, Nossal R. Principles of laser-Doppler flowmetry. In: Laser-Doppler blood flowmetry, Vol 107. Shepard Alber P and Öberg P Ake, editors. Boston: Kluwer Academic Publishers. 1990, 17.

2-7) Briers JD, Webster S. Laser speckle contrast analysis (LASCA): a nonscanning, full-field technique for monitoring capillary blood flow. J Biomed Opt. 1996, 1: 174.

2-8) Briers JD. Laser Doppler, speckle and related techniques for blood perfusion mapping and imaging. Physiol. Meas. 2001, 22: R35.

2-9) Chance B, Cohen P, Jobsis F, Schoener B. Intracellular oxidation-reduction state in vivo. Science 1962, 137: 499.
2-10) Chance B, Nioka S, Sadi S, Li C. Oxygenation and blood concentration changes in human subject prefrontal activation by anagram solutions. Adv Exp Med Biol. 2003, 510: 397.
2-11) Chapin JK, Lin CS. Mapping the body representation in the SI cortex of anesthetized and awake rats. J Comp Neurol. 1984, 229: 199.
2-12) Coq JO, Xerri C. Environmental enrichment alters organizational features of the forepaw representation in the primary somatosensory cortex of adult rats. Exp Brain Res. 1998, 121: 191.
2-13) Culver JP, Durduran T, Furuya D, Cheung C, Greenberg JH, Yodh AG. Diffuse optical tomography of cerebral blood flow, oxygenation, and metabolism in rat during focal ischemia. J Cereb Blood Flow Metab. 2003, 23(8): 911.
2-14) Du C, MacGowan GA, Farkas DL, Koretsky AP. Calcium measurements in perfused mouse heart: quantitating fluorescence and absorbance of Rhod-2 by application of photon migration theory. Biophys J 2001,80(1): 549.
2-15) Du C, Koretsky AP, Izrailtyan I, Benveniste H. Simultaneous detection of blood volume, oxygenation, and intracellular calcium changes during cerebral ischemia and reperfusion in vivo using diffuse reflectance and fluorescence. J Cereb Blood Flow Metab. 2005, 25: 1078.
2-16) Dunn AK, Bolay T, Moskowitz MA, Boas DA. Dynamic imaging of cerebral blood flow using laser speckle. J Cereb Blood Flow Metab. 2001, 21: 195.
2-17) Dunn A, Devor A, Bolay H et al. Simultaneous imaging of total cerebral hemoglobin concentration, oxygenation, and blood flow during functional activation. Opt. Lett. 2003, 28: 28.
2-18) Dunn A, Devor A, Dale AM, Boas DA. Spatial extent of oxygen metabolism and hemodynamic changes during functional activation of the rat somatosensory cortex. NeuroImage. 2005, 27: 279.
2-19) Duong TQ, Silva AC, Lee SP, Kim SG. Functional MRI of calcium-dependent synaptic activity: cross correlation with CBF and BOLD measurements. Magn Reson Med. 2000, 43: 383.
2-20) Durduran T, Burnett M, Yu G et al. Spatiotemporal Quantification of Cerebral Blood Flow During Functional Activation in Rat Somatosensory Cortex Using Laser-Speckle Flowmetry. J. Cereb. Blood Flow Metab. 2004, 24: 518.
2-21) Fabricius M, Akgoren N, Dirnagl U, Lauritzen M. Laminar analysis of cerebral blood flow in cortex of rats by laser-Doppler flowmetry: a pilot study. J Cereb Blood Flow Metab. 1997, 17(12): 1326.
2-22) Jones M, Berwick J, Johnston D, Mayhew J. Concurrent optical imaging spectroscopy and laser Doppler flowmetry: The inrelationship between blood flow, oxygenation, and volume in rodent barrel cortex. NeuroImage. 2001(13): 1002.
2-23) Kharlamov A, Brown BR, Easley KA, Jones SC. Heterogeneous changes in cerebral blood flow during hypotension demonstrated by laser speckle technique. J Cereb Blood Flow Metab Suppl. 2003, 23(S1): 84.

2-24) Kim S. Quantification of relative cerebral blood flow change by flow-sensitive alternating inversion recovery (FAIR) technique: application to functional mapping. Mag Res Med. 1995, 34: 293.
2-25) Kohl M, Lindauer U, Royl G, Kuhl M, Gold L, Villringer A, Dirnagl U. Physical model for the spectroscopic analysis of cortical intrinsic optical signals. Phys Med Biol. 2000, 45: 3749.
2-26) Kwong KK, Belliveau JW, Chesler DA, Goldberg IE, Weisskoff RM, Poncelet BP, Kennedy DN, Hoppel BE, Cohen MS, Turner R, Cheng HM, Brady T, Rosen B. Dynamic magnetic resonance imaging of human brain activity during primary sensory stimulation. Proc. Natl Acad Sci USA. 1992, 89: 5675.
2-27) Lindsburg PJ, O'Neil JT, Paakkari IA, Hallembeck JM, Feuerstein G. Validation of laser Doppler flowmetry in measurement of spinal cord blood flow. Am J Physiol. 1989, 257: H674.
2-28) Malonek D, Dirnagl U, Lindauer U, Yamada K, Kanno I, Grinvald A. Vascular Imprints of neural activity: Relationship between the dynamics of cortical blood flow, oxygenation, and volume changes following sensory stimulation. Proc Natl Acad Sci: Neurobiol. 1997, 94.: 14826.
2-29) Marieb EN. Human Anatomy & Physiology. Benjamin Cummings. 2003, 6 Ed.
2-30) Matsuura T, Fujita H, Seki C, Kashikura K, Yamada K, Kanno I. CBF change evoked by somatosensory activation measured by laser-Doppler flowmetry: independent evaluation of RBC velocity and RBC concentration. Jpn. J. Physiol. 1999, a(49): 289.
2-31) Matsuura T, Kanno I. Quantitative and temporal relationship between local cerebral blood flow and neuronal activation induced by somatosensory stimulation in rats. Neurosci Res. 2001, 40: 281.
2-32) National Nuclear Data Center, Brookhaven National Laboratory. Information extracted from the NuDat 2.1 database (retrieved Sept. 2005).
2-33) Navakatikyan M, Leonard BL, Evans RG, Malpas SC. Modelling the neural control of intrarenal blood flow. Clin Exper Pharm Physiol. 2000, 27: 650.
2-34) Nioka S, Luo Q, Chance B. Human brain functional imaging with reflectance CWS. Adv Exp Med Bio. 1997, 428: 237.
2-35) Offenhauser N, Thomsen K, Caesar K, Lauritzen M. Activity induced tissue oxygenation changes in rat cerebellar cortex: interplay of postsynaptic activation and blood flow. J. Physiol. 2005, 565(1): 279.
2-36) Paxinos G, Watson C. The rat brain in stereotaxic coordinates. Academic Press. 1982.
2-37) Phelps ME, Huang SC, Hoffman EJ, Selin C, Sokoloff L, Kuhl DE. Tomographic measurement of local cerebral glucose metabolic rate in humans with (F-18)2-fluoro-2-deoxy-D-glucose: validation of method. Ann Neurol. 1979, 6(5): 371.
2-38) Roy CS, Sherrington CS. On the regulation of the blood supply of the brain. J Physiol. 1890, 11: 85.
2-39) Silva AC, Koretsky AP. Laminar specificity of functional MRI onset times during somatosensory stimulation in rat. PNAS. 2002, 99 (23): 15182.

2-40) Skarphedinsson JO, Harding H, Thoren P. Repeated measurements of cerebral blood flow in rats. Comparison between the hydrogen clearance method and laser Dopplr flowmetry. Acta Physiol Scand. 1988, 134: 133.
2-41) Tenland T. On laser Doppler flowmetry: Methods and microvascular applications. Linkoping University Medical Dissertations, no. 136, Linkoping, Sweden, 1982.
2-42) Thomsen K, Offenhauser N, Lauritzen M. Principal neuron spiking: neither necessary nor sufficient for cerebral blood flow in rat cerebellum. J. Physiol. 2004, 560(1): 181.
2-43) Ureshi M, Matsuura T, Kanno I. Stimulus frequency dependence of the linear relationship between local cerebral blood flow and field potential evoked by activation of rat. NeuroSci Res. 2004, 48: 146.
2-44) Vongsavan N, Matthews B. Some aspects of the use of laser Doppler flow meters for recording tissue blood flow. Exp Physiol. 1993, 78: 1.
2-45) Xerri C , Bourgeon S, Coq JO. Perceptual context-dependent remodeling of the forepaw map in the SI cortex of rats trained on tactile discrimination. Behavioural Brain Research. 2005, 162: 207.
2-46) Yaoeda K, Shirakashi M, Funaki S, Funaki H, Nakatsue T, Abe H. Measurement of microcirculation in the optic nerve head by laser speckle flowgraphy and scanning laser Doppler flowmetry. Am J Ophthalmol. 2000, 129:734.

# Chapter 3 The Effect of Intravenous Lidocaine on Brain Activation During Non-Noxious and Acute Noxious Stimulation of the Forepaw: A Functional Magnetic Resonance Imaging Study in the Rat

## 3.1 Introduction

Lidocaine when administered systemically at doses that result in low plasma concentrations in the range of 1-10g/ml can alleviate acute pain [Bonica, 1953; Cassuto, 1985; Groudine, 1998; Matharu, 2004; Jonsson, 1991] and chronic neuropathic pain in humans and experimental animal models [Petersen, 2000; Strichartz, 2002; Amir, 2006; Araujo, 2003]. Interestingly, when effective, pain relief after a single intravenous (i.v.) lidocaine treatment can last for days or months [Chaplan, 1995], which is far beyond lidocaine's known pharmacokinetic longevity (rapid half-life 17min)[Bennett, 1982; Thomson, 1987]). The plasma concentrations of lidocaine that has proven therapeutic in alleviating pain are significantly below what is required to block electrically evoked peripheral nerve conduction in nociceptive C and Aδ-fibers and non-noxious Aβ fibers, which require near-lethal lidocaine concentrations >250 g/ml [Tanelian, 1991].

Several studies have explored the mechanisms that may underlie the unusually long-lasting analgesic effects of i.v. lidocaine. For example, in animal models of chronic pain, systemic low-doses of lidocaine were effective in blocking tonic neural discharges in injured peripheral Aδ and C-fiber nociceptors in dorsal root ganglions, which might explain its mechanism of action [Tanelian, 1991; Devor, 1991; Devor, 1992]. Other suggested targets for lidocaine's analgesic action include sodium channels and other receptor sites not in the periphery, but in the brain [Rykaczewska, 2006; Waxman, 2006; Zhao, 2006]. Information on lidocaine's effects in the brain or the contributions of these to the intriguing analgesic effects that have been observed in both acute and chronic pain is limited. Although lidocaine's effect on neurotransmitter release [Hernandez, 1991; Fujitani, 1994; Chen, 1994; Woodward, 1995] (21-24), seizure induction [Ikeda, 1982; Niederlehner, 1982; Kragh, 1993; Hirsch, 1997] (25-28) and neurotoxicity [Beardsley, 1995; Sakura, 2005; Yamashita, 2003; Radwan, 2002; Kanai, 1998; Sakura, 1995] in the central nervous system (CNS) has been extensively investigated, brain responses during exposure to painful stimuli with systemic lidocaine to our knowledge have not been characterized.

Non-invasive imaging techniques such as functional magnetic resonance imaging (fMRI) have been used to characterize changes in brain function in small animal models in response to a wide variety of drugs and/or somatosensory stimuli [Bock, 1998; Keilholz, 2004; Spenger, 2000; Austin, 2005; Kida, 2001, 2006; de Zwart, 2005] including acute nociception [Chang, 2001; Tracey, 2000]. For example, in the rat, acute stimulation via the sciatic nerve of nociceptive Aδ and C-fibers resulted in bilateral activation of known brain pain pathways (ie somatosensory cortex, cingulate cortex, medial thalamus and hypothalamus), which were attenuated by systemic morphine [Chang, 2001]. The effect of systemic cocaine, which, like lidocaine, exerts local anesthetic properties by blocking Na channels, has also been characterized using

fMRI and shown to enhance cortical somatosensory responses to intense sensory stimulation [Berwick, 2005; Devonshire, 2004].

As a first step in characterizing the effects of lidocaine on the pain response in the brain, we used blood-oxygen-level-dependent (BOLD) based fMRI to assess the activation pattern induced by innocuous somatosensory and acute noxious stimulation in the rat brain with and without low doses of lidocaine. Based on the knowledge that clinical relevant doses of systemic lidocaine do not block somatosensory or nociceptive peripheral nerve conduction and, we hypothesized that lidocaine would (1) not interfere with brain activation as measured by fMRI in response to neither innocuous somatosensensory nor acute nociceptive stimulation.

### 3.2 Materials and Methods

All surgical and experimental procedures were approved by the institutional animal care and use committee. Female Sprague-Dawley rats (210-290g) were used for the studies.

*Animal preparation for MRI*

All rats were initially anesthetized with 3% isoflurane and an intra-peritoneal (i.p.) dose of methohexital sodium (50mg/kg) and pre-treated with glycopyrolate (0.04mg/kg i.p.). Following oral intubation, mechanical ventilation was initiated (Harvard Apparatus, Inspira ASV). Anesthesia was maintained with 1.5-2% isoflurane delivered in a 1:1 air/O2 gas mixture. The femoral vein and a tail vein were catheterized for fluid and drug administration. Another catheter was inserted into the femoral artery for blood pressure and blood gas measurements during the study.

*MRI and Forepaw Stimulation Protocol*

All imaging was performed on a superconducting 9.4T/210 horizontal bore magnet (Magnex) controlled by an ADVANCE console (Bruker) and equipped with an actively shielded 11.6-cm gradient set capable of providing 20 G/cm (Bruker). A birdcage coil (inner diameter 72 mm) was used for transmission and a 30-mm diameter surface RF coil secured above the head of the rat as receiver. All vital signs (blood pressure, ECG, body temperature, respiratory rate, and peripheral pulse) were continuously monitored during the experiment (SAM PC monitor, SA Instruments, Inc). And arterial blood gases were monitored regularly and the ventilation adjusted as needed to maintain normal values. Needle electrodes were inserted under the skin of each forepaw, between digits 2 and 3 and digits 4 and 5. Following positioning and insertion of needle electrodes, the anesthesia was switched from isoflurane to α-chloralose (Sigma), first with an i.v. bolus of 40mg/kg over a 10-15 min time period followed by a continuous infusion of 25mg/kg/hr. Muscle paralysis with vecuronium (0.01mg/kg) was initiated after 2-3 trials of forepaw stimulations to assure that the anesthetic plane was adequate. If the forepaw stimulation did not induce changes in blood pressure, heart rate or the respiratory waveforms, the anesthetic depth was considered adequate.

For fMRI a single-shot echo-planar sequence was used with the following parameters: TR =1500ms; TE=30 ms; effective bandwidth=227272 Hz, field of view = 2.56×2.56 $cm^2$; 64×64 matrix with a resulting in-plane resolution of 400 μm; 8 axial 1.4 mm-thick slices spaced 0.15 mm apart. Each scan was acquired in 3 s (NA=2). To more accurately identify the anatomical location of the functional activation maps, higher resolution T2-weighted spin-echo images were acquired with identical spatial geometry using a RARE pulse-sequence.

The pulse train forepaw stimulations were generated using a commercial current stimulator (Isolated Pulse Stimulator 2100, A-M Systems). Negative short rectangular

current pulses of 0.3 ms duration were applied at a frequency of 3 Hz to either right or left forepaw. Preliminary data from the literature indicate that a 2mA forepaw stimulus seems to be innocuous (i.e., brain fMRI activation is limited to the somatosensory cortex and does not include other pain-related brain regions), whereas stronger stimulation currents are not. We therefore divided the animals into three groups based on the stimulation current used: Group 1 (n =4) 2mA; Group 2 (n=2) 4mA; and Group 3 (n=3) 8mA. The 2mA paradigm consisted of 23 scans acquired during resting baseline, 10 scans acquired during stimulation (total stimulation time 30s), and followed by a post-stimulation rest period of 30 scans (total acquisition time 63×3s =3.15min). To minimize painful exposures to the higher stimulation currents, we shortened the stimulation time for the 4 and 8mA trials. The 4mA paradigm consisted of 13 scans acquired during baseline, 3 scans during stimulation (total stimulation time 9 s), and followed by a post-stimulation rest period of 20 scans (total acquisition time: 36×3s=1.8min). The 8mA paradigm consisted of 13 pre-stimulation scans, 1 scan during stimulation (total stimulation time 3s) and 22 scans acquired after stimulation (total acquisition time: 36×3s=1.8min). For each of the stimulation current paradigms, the BOLD signal amplitude as well as the activation distribution acquired during control conditions were established before lidocaine administration. The baseline was obtained by repeating the stimulation paradigm (i.e., 2mA, 4mA or 8mA) 4 times at an interval of 6 –10min (Fig. 3-1). After the baseline acquisitions, the animals were allowed to rest for approximately 20min before administration of the first of the 3 escalating doses of lidocaine (see below). The entire fMRI experiment required approximately 3.5 h.

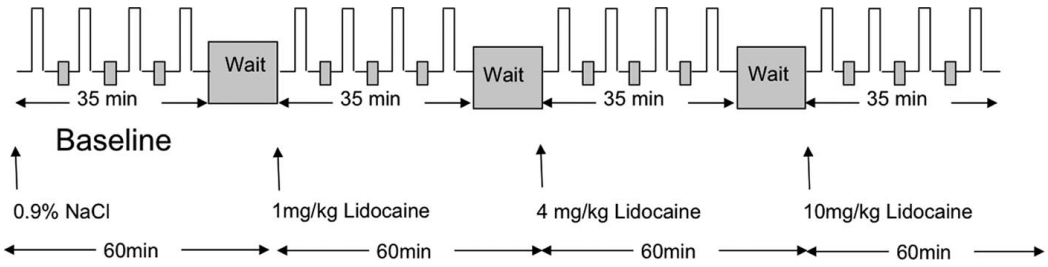


Fig. 3-1. Outline of experimental stimulation paradigm. The rat was allowed to rest 6–10min between each forepaw simulation trial. For the 2mA experiment the stimulation time was 30s. For the 4mA and 8mA currents the stimulation time was 9s and 3s, respectively. Lidocaine was injected IV after establishment of a fMRI baseline obtained over the first 1h (4 sets of stimulations). The first lidocaine dose was 1mg/kg, the second dose 4mg/kg, and the third 10mg/kg. One hour was allowed between each of the escalating doses of lidocaine.

*Systemic Lidocaine Analysis*

In clinical studies using lidocaine for treatment of neuropathic pain or acute nonneuropathic pain, lidocaine was administered IV to achieve plasma levels between 1 to 5 μg/mL [Peterson, 2000]. Thus, previous animal studies with systemic lidocaine have used IV computerized infusions to achieve similar lidocaine plasma concentration ranges to mimic the clinical studies and to keep the lidocaine in a nontoxic range.[Amir, 2006; Araujo, 2003] We did not use a continuous infusion of lidocaine. However, we performed experiments to determine the plasma lidocaine

concentration over time in rats anesthetized and prepared as described for the imaging experiments. The rats were similarly exposed to the escalating doses of lidocaine as shown in Fig. 3-1. Blood samples were collected at set time intervals via the femoral artery and placed in heparinized microcentrifuge tubes. The blood volume removed from the animals was replaced with an equal volume of blood containing heparin to avoid hemodynamic instability secondary to blood loss. The collected blood was centrifuged at 3000rpm for 5–10min, and the plasma was extracted and stored at -80°C until analysis. The blood sampling times were 5 and 35min after the 1mg/kg lidocaine dose and 5, 15, 25, and 35min after the 10mg/kg lidocaine dose (no samples were collected for the 4mg/kg/dose).

Lidocaine and five major unconjugated metabolites were quantified using a specifically developed and validated liquid chromatography procedure. Reference standards for lidocaine and xylidide (XYL) were purchased from Sigma Chemical Co. (St. Louis, MO) and Aldrich Chemical Co. (Milwaukee, WI), respectively. Metabolites monoethylglycinexylidide (MEGX), glycinexylidide, 4-hydroxyxylidide (4-OH-XYL), 3-hydroxymonoethylglycinexylidide (3-OH-MEGX), 3-hydroxylidocaine (3-OH-lidocaine) and internal standard pipecoloxylidide (PPX) were generously supplied by AstraZeneca Pharmaceutical Co. (Sodertalje, Sweden). The extraction procedure involved a 0.2mL sample of plasma (in 0.01M HCl) and the addition of 25μL (250ng) PPX, 0.5mL of 0.5M NaOH, and 5.0mL of ethyl acetate: methyl-tertbutyl ether (1:1). The mixture was shaken for 10min at a slow speed on a tilt-platform rocker and then centrifuged at 2000rpm for 15min. The top organic layer was transferred to a conical centrifuge tube containing 150μL of 0.1M HCl. The contents were mixed for 10 min and then centrifuged for 10min. The organic phase was aspirated to waste and the remaining acid layer evaporated to dryness using a vacuum centrifuge with moderate heat (approximately 45°C). The dried residue was reconstituted with 125μL of mobile phase and transferred to the autosampler inserts for chromatography.

Separation of the extracted lidocaine, its metabolites and internal standard was performed using an octadecylsilyl reversed phase column (Phenomenex Luna C-18, 3 μ, 150×4.6mm, Torrance, CA) with a mobile phase consisting of 0.05 M monobasic potassium phosphate: acetonitrile (84:16) with the addition of 1 mL/L phosphoric acid (85%), 1.2mL/L triethylamine, and 7mL/L heptane sulfonate (20%). The eluted compounds were detected by ultraviolet absorbance at 210nm. Using a flow rate of 1.5mL/min with a column thermostated at 32°C, the retention times of the eluted compounds were: 4-OH-XYL, 3.2min; 3-OH-MEGX, 4.7min; 3-OH-lidocaine, 6.5 min; glycinexylidide, 13.7min; XYL, 15.6 min; MEGX, 19.0 min; PPX, 26.0 min; lidocaine, 28.5 min. Every set of samples was preceded with a 7-point calibration curve, which included the expected concentration range of samples, a blank, and three sets of quality controls. The limit of quantification for lidocaine and the metabolites (except for 4-OH-XYL) was about 12.5ng/mL.

Fig. 3-2 shows the time course of the plasma lidocaine concentration after 1mg/kg and 10mg/kg (other metabolites not shown). As can be seen, the plasma lidocaine concentration is at the "therapeutic" target range of >1μg/mL at the 5-, 15-, and 25-min time points after the 10m/kg lidocaine dose. For the 1mg/kg dose, the plasma concentration is <1μg/mL at both the 5-min and 35-min time point.

In all imaging experiments, the rats were exposed to 1mg/kg, 4mg/kg, and 10mg/kg over the course of the study as illustrated in Fig. 3-1. Each dose of lidocaine was administered IV over 3–5min, which translated into approximately 0.5–0.1mg/min. After each of the IV lidocaine dose challenges, forepaw stimulation trials

were conducted at 5-min, 15-min, 25-min, and 35-min (Fig. 3-1). One hour was allowed between each of the escalating doses of lidocaine to assure that the lidocaine plasma concentration was negligible before the next dose was administered.

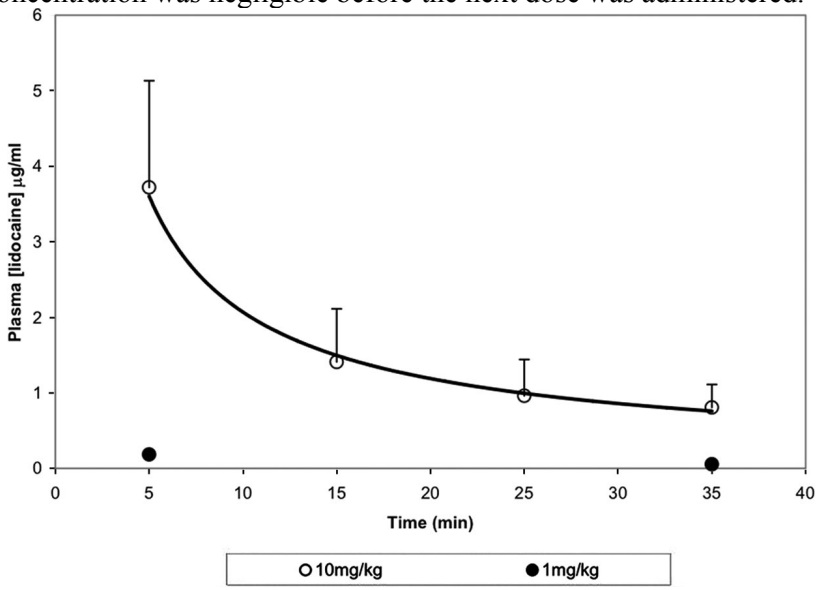


Fig. 3-2. The time course of the average plasma lidocaine concentration after 1mg/kg and 10mg/kg in 3 rats. As can be seen, the plasma lidocaine concentration is at the 'therapeutic' target range of >1µg/mL at the 5-, 15-, and 25-min time points after the 10mg/kg lidocaine dose. For the 1mg/kg dose the plasma concentration is <1µg/mL at both the 5-min and 35-min time point.

*MRI Data Analysis*

The fMRI images were analyzed using Stimulate V6.01 (CMRR, University of MN). After a background masking, the intensity time course of each pixel during the scan was cross-correlated with a boxcar template according to the known stimulation profile. We used a correlation coefficient ($r$) $\geq$0.3 which corresponds to a $P$ value of 0.01 to calculate the activation maps and detect the areas with a statistically significant BOLD signal. A 4-neighbor 2D clustering was performed to remove scattered false activation. For each rat, a sector-shape region of interest (ROI) was delineated covering the entire forepaw area of the somatosensory cortex (which spanned 2–3 of the acquired slices and included both primary and secondary somatosensory cortex). Both the number of pixels (nominally, each pixel accounts for a volume of $0.4\times0.4\times1.5=0.24mm^3$/voxel) and the average time course of the statistically significantly active voxels (voxels with $r\geq$ 0.3) within the ROI were extracted for each trial, and used to represent the spatial and temporal profile of the BOLD response, respectively. Each time course was then normalized to its mean value during the pre-stimulation baseline and the peak value was extracted to assess the magnitude for each stimulation trial. All calculated and color-coded functional activity maps were overlaid on the echo-planar images and the anatomical location of activated pixels identified by comparing with the corresponding high resolution T2-weighted MRI images. Intra-group differences in the baseline BOLD signal amplitude and spatial extension of BOLD activation (number of pixels with statistically significant BOLD signal increases) were analyzed using an F-test. Statistical differences between the averaged baseline BOLD signal amplitude (average of the four individual stimulations before injection of lidocaine) and amplitudes obtained

after the lidocaine administrations were analyzed using a paired *t*-test with a post-hoc bonferroni correction for multiple comparisons. Statistical differences between the cortical volume activated during baseline conditions (average of the 4 trials) was compared with cortical volumes activated 5-min (where the plasma lidocaine concentration was highest) after each of the escalating doses of lidocaine using a paired *t*-test.

### 3.3 Results

*Physiological Values*

All rats had normal blood gas values during the fMRI experiments. Stimulation with 2mA (30s), 4mA(9s) or 8mA (3s) did not produce significant increases in MABP or heart rate. There was no significant effect of IV lidocaine on the MABP or the heart rate regardless of dose administered (data not shown).

*Baseline Brain BOLD Responses and Activity Maps with 2mA and 8mA Stimuli*

Fig. 3-3 shows typical activation maps of the BOLD signal response in the rat brain elicited by each of the 4 baseline 2mA-30s forepaw stimulation trials. As expected, right (or left) forepaw stimulation produced BOLD signal increases in the contralateral primary somatosensory cortex (S1) area corresponding to the forepaw territory. In the 4 Group-1 rats exposed to 2mA for 30s, the S1 area was the only significant brain region eliciting a BOLD response; although this suggests the 2mA-30s stimulus was an innocuous stimulus, because with an $r>0.3$ threshold for data analysis, it is possible that sub-threshold activation of other areas went undetected. The number of pixels (pixels with a statistically significant BOLD signal) in S1 activated by the 2mA stimulus was highly consistent from trial to trial in individual animals (Fig.3), although modest variation in the total number of pixels activated was observed across subjects. Analysis of all Group 1 rats demonstrated that the average amplitudes of the 4 individual 2 mA-induced BOLD responses acquired during control conditions were 4.1%±1.7%, 3.9%±2.5%, 4.5%±0.3% and 4.5%±1.7%, with statistical analyses revealing no significant trial to trial differences (F-test, $P>0.05$) thus indicating that a stable stimulation baseline was present before IV lidocaine challenges.

Forepaw stimulation with 4 mA elicited the expected contrallateral S1 activation. However, areas with significant BOLD signal increases were also observed in the ipsilateral (in relation to the paw stimulated) thalamus, bilaterally in the ventral tegmental area (VTA) and hypothalamus, albeit somewhat inconsistently from stimulation trial to trial. Because of this inconsistency, data derived from 4 mA stimulation were not assessed further.

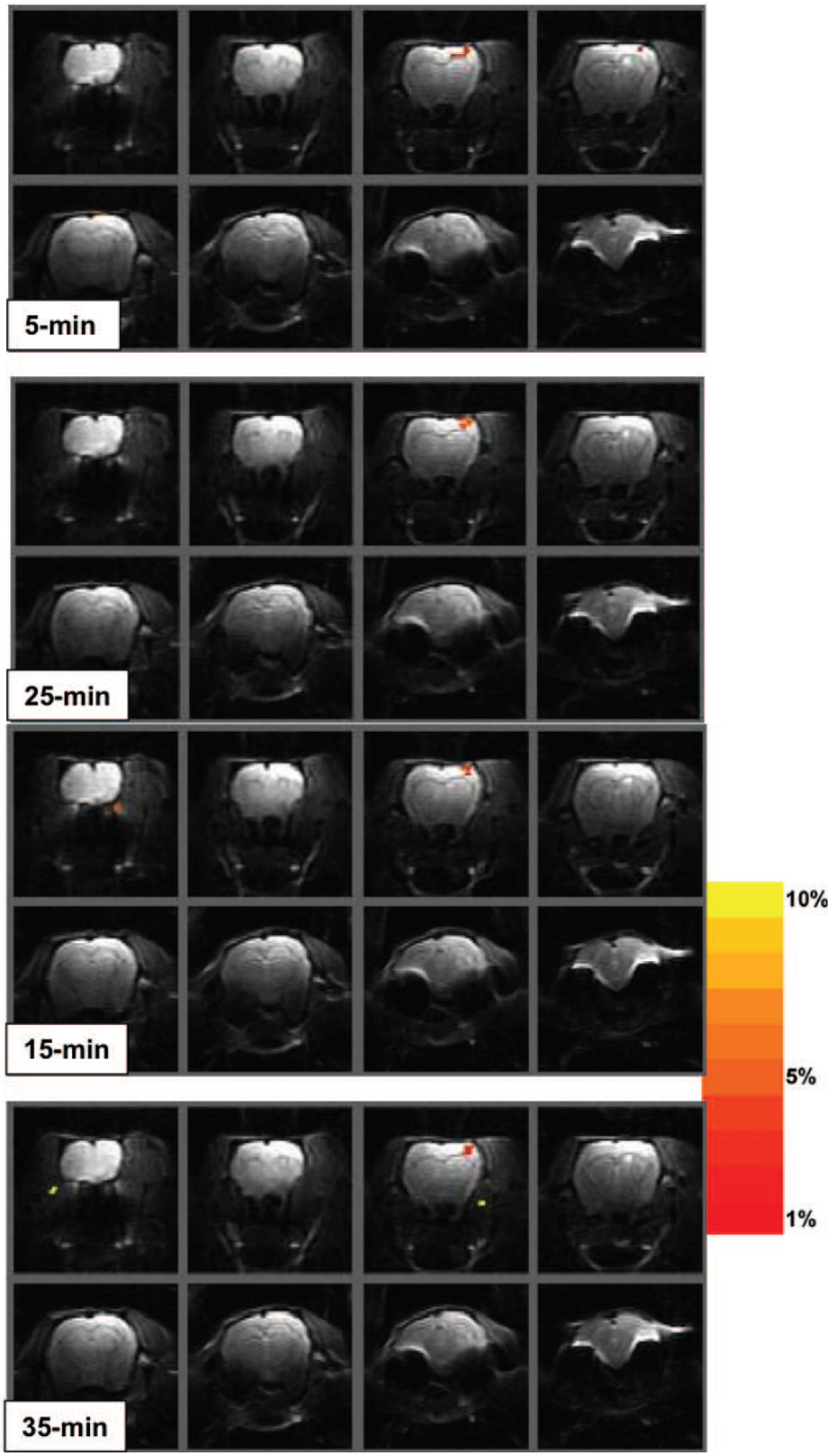


Fig. 3-3. Blood-oxygen-level-dependent (BOLD) activation maps of the responses to 2mA forepaw stimulation for 30s obtained during control conditions (no lidocaine) derived from EPI magnetic resonance imaging

(MRI) images in a Group-1 rat. The activated pixels were calculated using a cross-correlation of $r$>0.3 (STIMULATE). The color bar to the right is a 10-step transition from red to yellow which corresponds to a positive BOLD signal increase from 1% to 10%. In this particular animal the total volume of pixels with statistically significant BOLD signal increase over the 4 individual baseline stimulation trials was 3.6mm$^3$, 1.9mm$^3$, 3.6mm$^3$, and 2.4mm$^3$. The corresponding BOLD signal amplitudes of the 1st, 2nd, 3rd, and 4th stimulation was 2.3%, 2.1%, 4.8% and 2.4%, respectively.

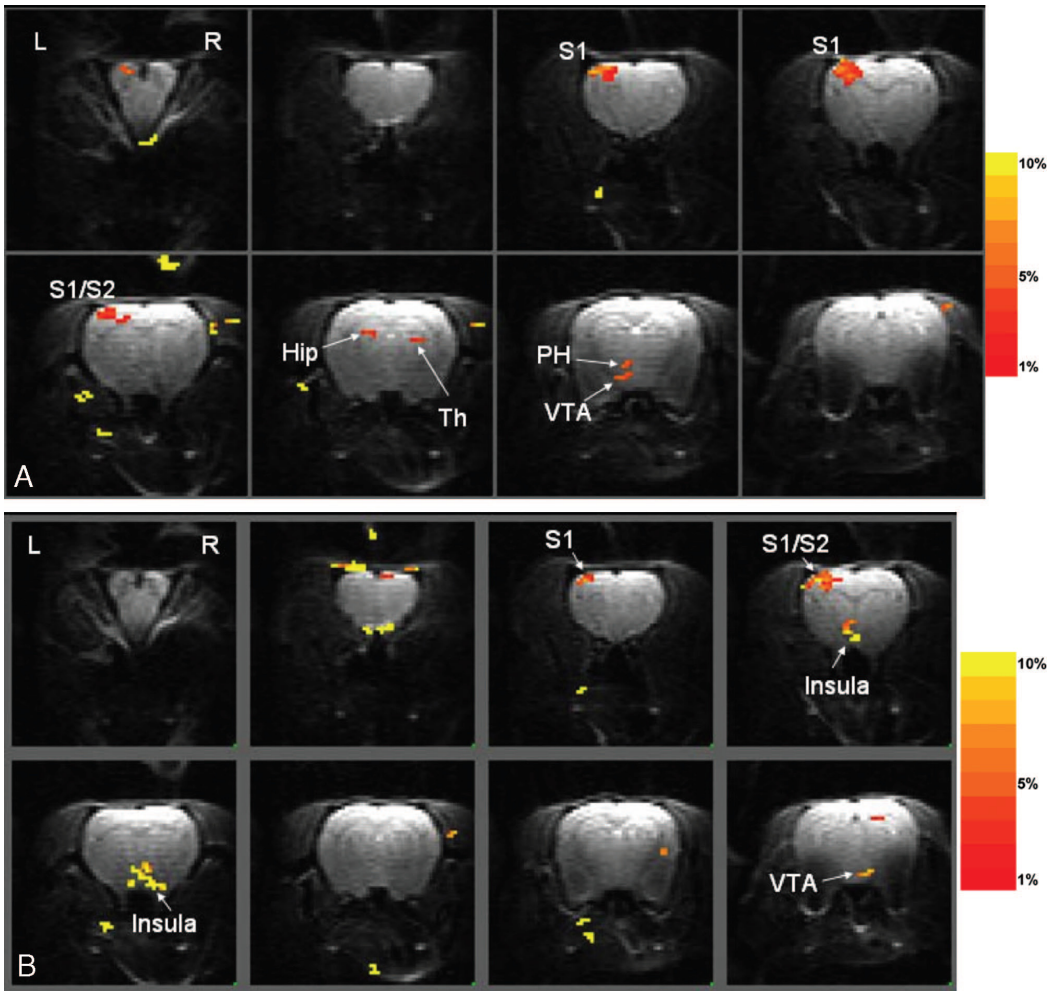


Fig. 3-4. (A) Brain activation map during forepaw stimulation with 8mA for 3s obtained under control conditions before the lidocaine challenges. In this particular animal, brain regions with statistically significant BOLD signal increases was observed contralateral to the forepaw stimulated in the following regions: primary somatosensory cortex (S1), secondary somatosensory cortex (S2), hippocampus, posterior hypothalamus and ventral tegmental area (VTA). Thalamic activity was also observed ipsilateral to the forepaw stimulated. (B) Example with additional activation of the insula region in another rat. Th=thalamus; PH=posterior hypothalamus; Hip=hippocampus. Activated brain regions were identified by comparing locations on the raw EPI images with their anatomical counterparts and labeled rat brain atlas templates. BOLD signal changes are

also observed outside of the brain corresponding to the surface of the brain and/or muscles and are related to large venous structures.

Forepaw stimulation with 8mA for 3s consistently elicited BOLD signal increases in the contralateral S1 and S2. However, in all of the animals, several other brain areas associated with activation of nociceptive C-fibers, such as the thalamus, insula, hypothalamus and VTA,[Peyron, 2000] were also activated although not always coincidently. Nonetheless, because the stimulation trials always included 2–3 of the regions listed above in addition to S1/S2 activation, it was concluded that this stimulation current was noxious. Table 3-1 lists the regions of the brain that were observed to be activated in response to the 8mA forepaw stimulation during control conditions in 3 different animals. Fig. 3-4A shows an example in one of the rats and demonstrates activation in the following areas contralateral to the forepaw stimulated: S1, secondary somatosensory cortex (S2), thalamus, posterior hypothalamus and the VTA. Fig. 3-4B shows another example of brain activation in response to the noxious stimulation with additional activation of the insula. Under control conditions, the BOLD signal amplitude and total activated pixel volume in S1/S2 elicited by forepaw stimulation with 8mA was 5.8%±0.4% and 7.4±2.6 $mm^3$, respectively

Table 3-1. Brain Regions Activated by the Noxious 8 mA Forepaw Stimulus

| Animal Num | Brain regions activated contralateral to the forepaw stimulated | Brain regions activated ipsilateral to the forepaw stimulated |
|---|---|---|
| 1 | S1/S2<br>Thalamus<br>Entorhinal cortex<br>Posterior cingulated cortex<br>VTA | Caudate putamen<br>Temporal cortex<br>Thalamus<br>VTA |
| 2 | S1/S2<br>Entorhinal cortex<br>Insula<br>Thalamus<br>Temporal cortex | Posterior cingulate cortex |
| 3 | S1/S2<br>Insula<br>VTA<br>Posterior hypothalamus<br>Entorhinal cortex<br>Temporal cortex<br>Posterior cingulated cortex | Entorhinal cortex<br>VTA |

VTA = ventral tegmental area.

In a few control animals, we also investigated the stability of the forepaw stimulation brain activation signal over a subsequent 3-h period during which no IV lidocaine was administered. Fig. 3-5 shows the result of a control experiment using an 8mA, 3s forepaw stimulus according to the experimental stimulation design but without the lidocaine challenges. As can be seen, the amplitude of the BOLD signal response measured in primary somatosensory cortex (average of all activated pixels) for each stimulation trial was relatively stable over the 2–3h study time. The

corresponding cortical volume activated by the 8mA, 3s forepaw stimulus in S1 for each trial was also relatively consistent over this timeframe.

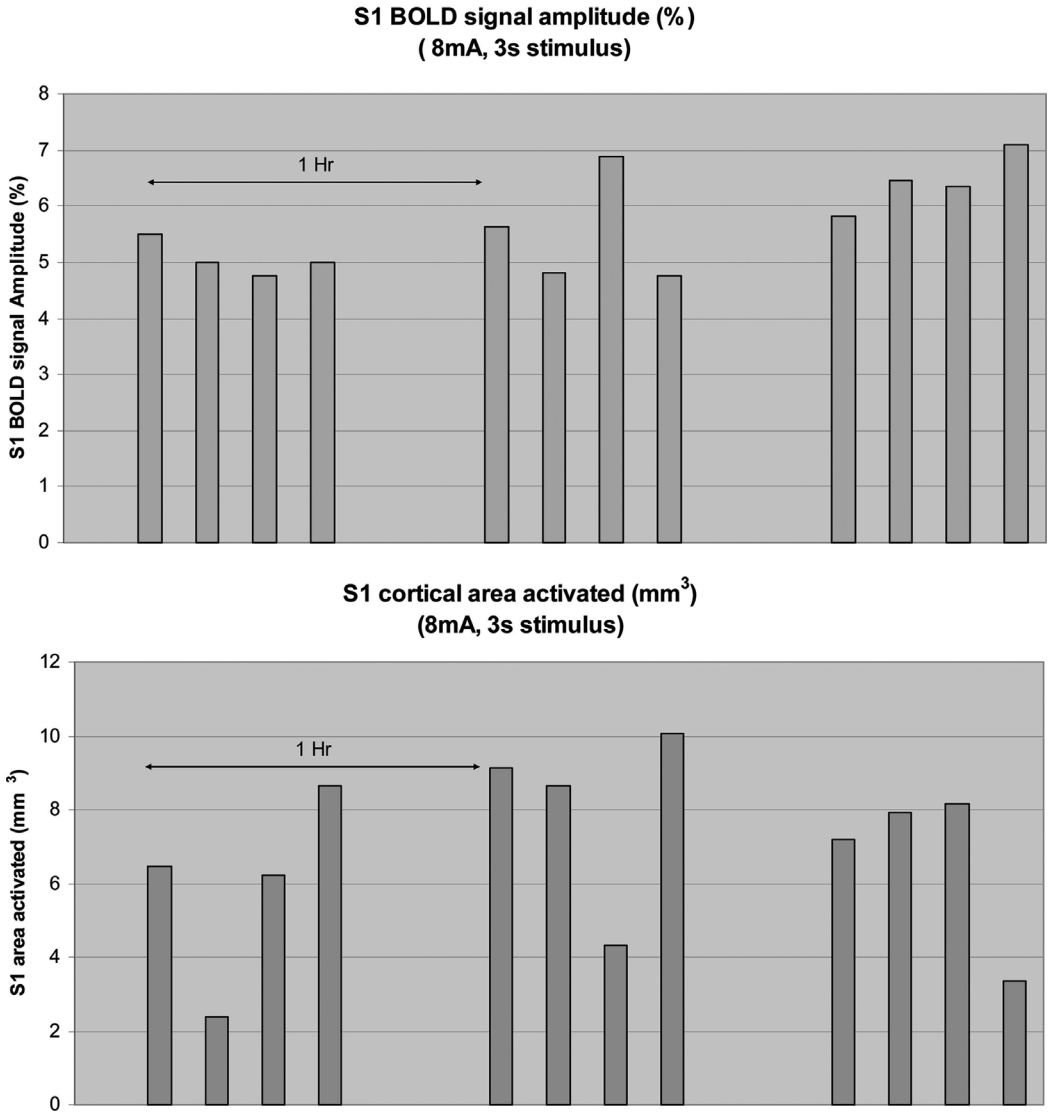


Fig. 3-5. The result of a control experiment using the repetitive 8mA, 3s forepaw stimulation paradigm as outlined in Fig. 3-1 but without the IV lidocaine challenges. As can be seen the amplitude of the BOLD signal response measured in primary somatosensory cortex (average of all activated pixels) for each stimulation trial was relatively stable over the 2–3h study time. The corresponding cortical volume activated by the 8mA, 3s forepaw stimulus in S1 for each trial was also relatively consistent over time although some variation is seen.

*Effect of IV Lidocaine*

(1) Innocuous 2mA, 30s stimulus

The effect of the increasing doses of IV lidocaine on the BOLD signal elicited by the 2mA, 30s stimulus is shown in Table 2. First, the BOLD signal amplitude elicited by 2mA in S1 did not change significantly with either dose of lidocaine when compared with the baseline amplitude. Second, the average volume of pixels in

S1 activated at baseline conditions was 5.9±3.2mm$^3$, and there were no statistically significant changes in the total volume of activated pixels in S1 observed with either dose of lidocaine. However, the S1 response varied considerably from animal to animal. For example, at 5min after the 10mg/kg IV lidocaine challenge, the volume of activated pixels elicited by the 2mA, 30s stimulus in S1 increased from approximately 6mm$^3$ to approximately 20±18 mm$^3$ The large variation in the number of activated pixels is a consequence of 3 animals that demonstrated clear increases in the volume of activated pixels in S1 after the 10mg/kg dose, but one animal which did not. Collectively, the data from the group approached, but did not reach, statistical significance (P=0.056).

Table 3-2. Amplitude of BOLD Signal Changes and Total Volume of Activated Pixels of Group 1 Rats

| BOLD sginal | Condition | 5 min | 15 min | 25 min | 35 min |
|---|---|---|---|---|---|
| Amplitude% | Baseline | 4.3 ± 0.3 | | | |
| | Lidocaine 1 mg/kg (5-min) | 5.6 ± 1.2 | 4.6 ± 1.9 | 6.2 ± 0.8 | 5.5 ± 1.4 |
| | Lidocaine 4 mg/kg (5-min) | 5.3 ± 1.1 | 5.3 ± 0.5 | 4.8 ± 1.4 | 5.5 ± 1.1 |
| | Lidocaine 10mg/kg (5-min) | 6.4 ± 1.6 | 5.5 ± 1.1 | 5.4 ± 1.3 | 5.5 ± 0.4 |
| Activated Volume (mm$^3$) | Baseline | 6 ± 3 | | | |
| | Lidocaine 1 mg/kg (5-min) | 13 ± 7 | 15 ± 6 | 14 ± 6 | 14 ± 7 |
| | Lidocaine 4 mg/kg (5-min) | 18 ±16 | 20 ±15 | 17 ± 15 | 14 ± 11 |
| | Lidocaine 10mg/kg (5-min) | 20±18 | 25 ± 15 | 17 ± 11 | 21 ± 11 |

Data are mean ± SD and are derived from Group 1 animals.

(2) Noxious 8mA, 3s stimulus

Fig. 3-6 shows the brain activation pattern in response to the noxious 8mA forepaw stimuli at baseline and 5min after 4mg/kg and 10mg/kg IV lidocaine. First, Fig. 3-6 demonstrates that brain regions involved in nociception are still activated, including S1 and S2 in spite of the IV challenges with 4mg/kg and 10mg/kg lidocaine. In addition, Fig. 3-6 shows that the fMRI BOLD response in S1/S2 is enhanced (increased total number of pixels) immediately after administration of lidocaine. Fig. 3-7 shows brain activation patterns in response to the nociceptive stimulus 5-min after 10 mg/kg lidocaine in 2 different rats. In the first rat (left forepaw stimulation), brain activation is elicited contralateral in the right in S1, VTA, thalamus and posterior hypothalamus (Fig. 3-7). In the second rat (right forepaw stimulation), brain activation was elicited in the left S1/S2 and thalamus (Fig. 3-7). Table 3-3 shows that the average amplitude of the BOLD signal in somatosensory cortex immediately after 1 mg/kg lidocaine was 7.1% ±1.0%, which was not statistically different from the baseline BOLD signal amplitude (Table 3-3). Further, the pixel volume activated in S1 in response to the 8 mA forepaw stimulus 5-min after 1 mg/kg lidocaine was also similar to baseline conditions. However, the amplitude of the BOLD signal after 10 mg/kg lidocaine was 6.9% and significantly higher than at baseline (5.8±0.4% vs 6.9±0.4%, P=0.0025). In addition, analysis of the 4 mg/kg and 10 mg/kg lidocaine

brain activation maps, demonstrated that the total volume of activated S1/S2 cortex was significantly larger than that observed during control conditions. For example, 5-min after the 4 mg/kg lidocaine challenge the activated pixel S1/S2 volume increased from 7.4 to 15.7 $mm^3$ (P=0.008), and for the 10 m/kg lidocaine challenge it increased from 7.4 to 19.2 $mm^3$ (P=0.03).

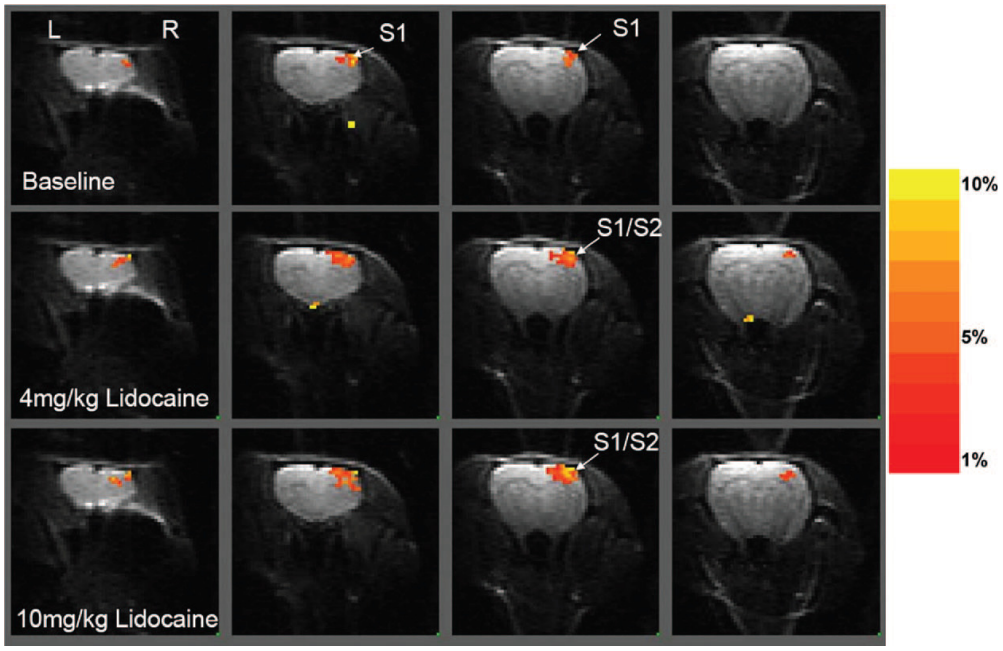


Fig. 3-6. Brain activation patterns in response to the noxious 8mA forepaw stimuli at baseline and 5min after 4mg/kg and 10mg/kg IV lidocaine. As can be seen brain regions involved in nociception are still activated including S1 and S2 in spite of the lidocaine. In addition Fig. 3-6 shows that the BOLD response in S1/S2 is enhanced (increased total number of pixels) after administration of lidocaine.

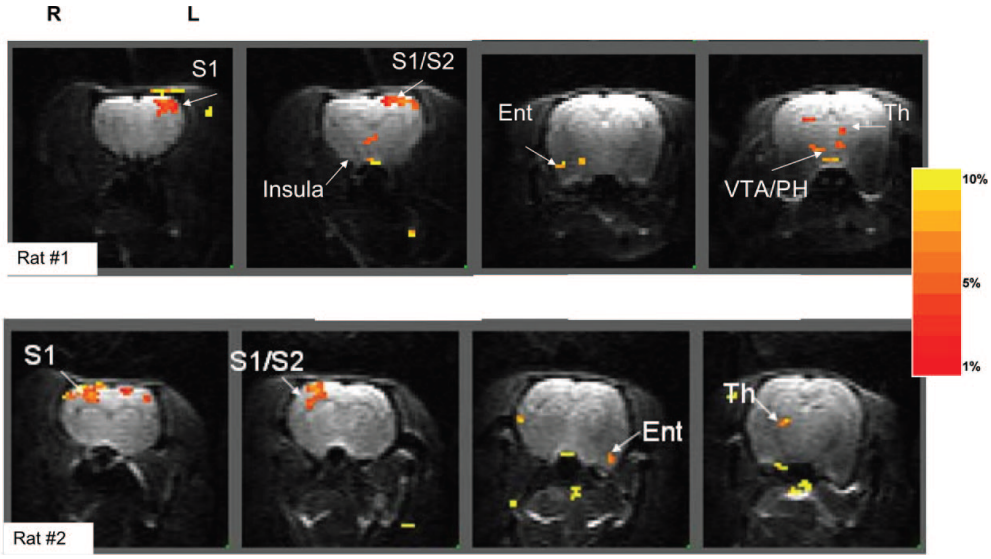


Fig. 3-7. Brain activation patterns in response to the nociceptive stimulus 5min after 10mg/kg lidocaine in 2 different rats. In the first rat, (left forepaw stimulation) brain activation is elicited contralateral in the right in S1,

ventral tegmental area (VTA), thalamus, and posterior hypothalamus. In the second rat (right forepaw stimulation) brain activation was elicited in the left S1/S2 and thalamus.

Table 3-3. Number of Pixels with Statistically Significant BOLD Signal Increases and the Average BOLD Signal Amplitude (1st Stimulus) in Somatosensory Cortex (S1/S2) Induced by Forepaw Stimulation with 8 mA for 3 s Acquired During Baseline Conditions and 5-min After IV Lidocaine

| 8mA, 3s stimulus | condition | Somatosensory cortex (S1/S2) |
|---|---|---|
| BOLD signal amplitude (%) | Baseline | 5.8±0.4 |
| | Lidocaine 1 mg/kg (5-min) | 7.1±1.0 |
| | Lidocaine 4 mg/kg (5-min) | 6.4 ± 0.8 |
| | Lidocaine 10mg/kg (5-min) | 6.9 ± 0.4 |
| Volume activated ($mm^3$) | Baseline | 7.4 ± 2.6 |
| | Lidocaine 1 mg/kg (5-min) | 11.0 ± 9.4 |
| | Lidocaine 4 mg/kg (5-min) | 15.7 ± 3.9 |
| | Lidocaine 10mg/kg (5-min) | 19.2 ± 1.5 |

a) The average BOLD signal amplitude elicited by 8mA in S1/S2 approximately 5-min following 10mg/kg was statistically significant from baseline (5.8±0.4% vs 6.9±0.4%. P=0.0025).
b) The S1/S2 volume activated by 8mA in S1/S2 approximately 5min following 4mg/kg was statistically significantly larger than that activated before lidocaine (7.4±2.6$mm^3$ vs 15.7±3.9$mm^3$, P=0.008).
c) The S1/S2 volume activated by 8mA in S1/S2 approximately 5min following 10mg/kg was statistically significantly larger than that activated before lidocaine (7.4±2.6$mm^3$ vs 19.2±1.5$mm^3$, P=0.03).

### 3.4 Discussion

The major finding of this study was that lidocaine, when administered IV, did not abolish or diminish the brain's response as measured by fMRI BOLD to innocuous or acute noxious electrical stimulation of the forepaw in normal rats. We also showed for the first time that lidocaine enhanced the somatosensory cortical fMRI BOLD response to acute noxious stimulation as evidenced by an increase in the number of activated pixels. Previous experimental animal studies have demonstrated that nerve conduction in peripheral nerves is not blocked by therapeutic, low dose lidocaine.[Araujo, 2003; Huang, 1997; Mao, 2000] Other targets for lidocaine's analgesic action have therefore been suggested, including sodium channels and other receptor sites, not in the peripheral nervous system, but in the central nervous system.[Rykaczewska, 2006; Waxman, 2006; Zhao, 2006] Here we used fMRI to visualize forebrain activation during brief acute pain and demonstrated that the brain circuits and pathways activated in response to peripherally evoked acute noxious stimulation were not disrupted by systemic lidocaine in contrast to what has been observed previously for opioid analgesics, such as morphine.[ Balasubramanian, 2006; Borras, 2004; Hagelberg, 2002; Wise, 2002; Wise, 2004] These results raise several questions. First, does the animal model of acute pain used here to test the analgesic action of lidocaine mimic the clinical condition? Second, what causes the lidocaine induced somatosensory fMRI BOLD enhancement observed during acute nociception?

And third, is the lidocaine-induced cortical fMRI BOLD enhancement of importance for its analgesic efficacy?

*Animal Model of Acute Pain: Clinical Relevance*

To elicit acute pain in the rat, we applied an 8 mA electrical current to the forepaw for 3 s which elicited activation in brain areas known to be involved in acute nociception. Our data agree with previous documentation of neuroanatomical pathways involved in acute pain observed in humans[Peyron, 2000; Balasubramanian, 2006; Borras, 2004; Wise, 2002; Wise, 2004] and animals. [Chang, 2001; Baron, 1999; Shah, 2005; Lowe, 2007] For example, neuroimaging studies in humans have demonstrated hemodynamic brain responses to acute pain in somatosensory cortex (S1 and S2) and insula contralateral to stimulation, anterior cingulate cortex and thalamus primarily contralateral to stimulation but often bilateral (for review[Peyron, 2000]). Preclinical studies with fMRI require that animals be anesthetized and thus a possible confound in these studies is the potential interaction between the anesthetic, the stimulus and/or the drugs tested. However, we used α-chloralose as an anesthetic which interferes the least with brain activation during nociceptive stimulation of A-σ and C-fiber.[Chang, 2001; Baron, 1999; Shah, 2005; Lowe, 2007] For example, electrical stimulation of A-σ and C-fibers via the sciatic nerve elicited activation in somatosensory cortex, cingulated cortex, thalamus and hypothalamus, which could be partially inhibited by morphine.[Chang, 2001] The slightly different distribution of brain activation in previous animal studies and those reported here is probably attributable to differences in the magnitude and length of the noxious stimulus applied (e.g., in previous studies the stimulus was applied for several minutes, whereas it only lasted for 3s in our study). Thus, based on the brain activation patterns that we observe with the noxious 8 mA forepaw stimulus, it is reasonable to conclude that the animal model used is relevant as an acute pain model from a clinical point of view given the fact that some of the same brain regions observed here are activated in humans exposed to acute pain.[Peyron, 2000] It is important, however, to emphasize that we tested the effect of systemic lidocaine on brain responses to acute, brief pain exposures which activate only the normal physiological pain pathways. One could argue, therefore, that a more clinically relevant experimental model is one that is representative of pathological pain that occurs secondary to both peripheral and central hypersensitization. In studies in which lidocaine has shown analgesic efficacy, pathological pain is an important component and thus the potential mechanism of lidocaine may be in altering components of pathological pain pathways in the brain, which clearly warrants further investigation. However, from our results it seems unlikely that lidocaine's mechanism of action in providing analgesia is by affecting physiological pain pathways.

*Lidocaine-induced fMRI Enhancement of Cortical Activation with Acute Nociception*

The lidocaine-induced enhancement of the fMRI BOLD activation in somatosensory cortex to acute noxious stimulation is in agreement with data previously reported for cocaine[Devonshire, 2004] which, like lidocaine, has local anesthetic actions. Cocaine, when administered IV (0.75mg/kg), was shown to augment the electrophysiological response of thalamic neurons to vibrissae stimulation.[Rutter, 1998; Rutter, 2005] Furthermore, Devonshire et al.[ Devonshire, 2004] demonstrated that the neuronal response as measured by summed field potential to intense somatosensory (whisker) stimulation after cocaine was enhanced in barrel cortex. In parallel with the electrophysiological recordings, they also measured the hemodynamic responses during somatosensory stimulation using a combination of optical and BOLD fMRI techniques.[ Berwick, 2005] The data demonstrated that, because cocaine in itself

increased the baseline cerebral blood flow and BOLD signals over time in the somatosensory cortex, the ensuing responses recorded were not accurately reflecting the enhanced neuronal response.[Berwick, 2005] We observed that lidocaine enhanced the fMRI BOLD activation in somatosensory cortex in response to the acute noxious stimulation and, because lidocaine unlike cocaine does not seem to affect baseline cerebral hemodynamics to the same degree,[Lam, 1997] we suggest therefore that the fMRI enhancement observed truly represents enhanced neuronal activation.

*Implications for the Mechanisms of Action of lidocaine in Treatment of Pain*

Both lidocaine and cocaine block sodium channels, which is a mechanism that is believed to contribute to the analgesic effects of lidocaine in neuropathic pain. However, because sodium channels are responsible for the initiation and propagation of action potentialls, [Goldin, 1999] their blockade by lidocaine would have been expected to decrease and not increase cortical activation with somatosensory stimulation. However, we recently showed that both cocaine and lidocaine (1mg/kg) increased the intracellular calcium concentration $[Ca^{2+}]_i$ in somatosensory cortex.[Du, 2006] Since fluctuations in $[Ca^{2+}]_i$ levels affect neuronal excitability,[Verkhratsky, 2006] we propose that lidocaine's ability to increase $[Ca^{2+}]_i$ in somatosensory neurons could also underlie the enhanced cortical activation to noxious and nonnoxious stimulation. Moreover, the increase in $[Ca^{2+}]_i$ in somatosensory cortex by lidocaine may also be relevant for its analgesic effects since studies have proposed a decrease in neuronal calcium currents in somatosensory neurons as the mechanism underlying neuropathic pain.[Fuchs, 2007; Hogan, 2007; McCallum, 2006]

### 3.5 Conclusion

We studied the effects of lidocaine on acute painful stimulation in the brain and demonstrated an increase in the somatosensory fMRI BOLD signal to brief noxious stimuli after lidocaine administration. Our results suggest that lidocaine's analgesic efficacy is unlikely to be through an action on normal physiological pain pathways. To further determine the potential mechanism of lidocaine's analgesic action, future studies are required in animal models of neuropathic pain to assess if under these conditions lidocaine alters signaling in the pain pathways in the brain. We are also planning future fMRI studies to characterize the effect of selective calcium channel inhibitors on the brain's response to acute and chronic pain.

### 3.6 List of References

3-1) Amir R, Argoff CE, Bennett GJ et al. The role of sodium channels in chronic inflammatory and neuropathic pain. J Pain. 2006, 7: S1.

3-2) Araujo MC, Sinnott CJ, Strichartz GR. Multiple phases of relief from experimental mechanical allodynia by systemic lidocaine: responses to early and late infusions. Pain. 2003, 103: 21.

3-3) Austin VC, Blamire AM, Allers KA et al. Confounding effects of anesthesia on functional activation in rodent brain: a study of halothane and alpha-chloralose anesthesia. Neuroimage. 2005, 24: 92.

3-4) Balasubramanian S, Morley-Forster P, Bureau Y. Opioids and brain imaging. J Opioid Manag. 2006, 2: 147.

3-5) Baron R, Baron Y, Disbrow E, Roberts TP. Brain processing of capsaicin-induced secondary hyperalgesia: a functional MRI study. Neurology. 1999, 53: 548.

3-6) Beardsley D, Holman S, Gantt R et al. Transient neurologic deficit after spinal anesthesia: local anesthetic maldistribution with pencil point needles? Anesth Analg. 1995, 81: 314.

3-7) Berwick J, Devonshire IM, Martindale AJ et al. Cocaine administration produces a protracted decoupling of neural and haemodynamic responses to intense sensory stimuli. Neuroscience. 2005, 132: 361.
3-8) Bennett PN, Aarons LJ, Bending MR et al. Pharmacokinetics of lidocaine and its deethylated metabolite: dose and time dependency studies in man. J Pharmacokinet Biopharm. 1982, 10: 265.
3-9) Bock C, Krep H, Brinker G, Hoehn-Berlage M. Brain mapping of alpha-chloralose anesthetized rats with T2*-weighted imaging: distinction between the representation of the forepaw and hindpaw in the somatosensory cortex. NMR Biomed. 1998, 11: 115.
3-10) Bonica J. The management of pain. Philadelphia: Lea & Febiger. 1953.
3-11) Borras MC, Becerra L, Ploghaus A et al. fMRI measurement of CNS responses to naloxone infusion and subsequent mild noxious thermal stimuli in healthy volunteers. J Neurophysiol. 2004, 91: 2723.
3-12) Cassuto J, Wallin G, Hogstrom S et al. Inhibition of postoperative pain by continuous low-dose intravenous infusion of lidocaine. Anesth Analg. 1985, 64: 971.
3-13) Chang C, Shyu BC. A fMRI study of brain activations during non-noxious and noxious electrical stimulation of the sciatic nerve of rats. Brain Res. 2001, 897: 71.
3-14) Chaplan SR, Bach FW, Shafer SL, Yaksh TL. Prolonged alleviation of tactile allodynia by intravenous lidocaine in neuropathic rats. Anesthesiology. 1995, 83: 775.
3-15) Chen NH, Reith ME. Effects of locally applied cocaine, lidocaine, and various uptake blockers on monoamine transmission in the ventral tegmental area of freely moving rats: a microdialysis study on monoamine interrelationships. J Neurochem. 1994, 63: 1701.
3-16) Devonshire IM, Berwick J, Jones M et al. Haemodynamic responses to sensory stimulation are enhanced following acute cocaine administration. Neuroimage. 2004, 22: 1744.
3-17) Devor M. Neuropathic pain and injured nerve: peripheral mechanisms. Br Med Bull. 1991, 47: 619.
3-18) Devor M, Wall PD, Catalan N. Systemic lidocaine silences ectopic neuroma and DRG discharge without blocking nerve conduction. Pain. 1992, 48: 261.
3-19) de Zwart JA, Silva AC, van Gelderen P et al. Temporal dynamics of the BOLD fMRI impulse response. Neuroimage. 2005, 24: 667.
3-20) Du C, Yu M, Volkow ND et al. Cocaine increases the intracellular calcium concentration in brain independently of its cerebrovascular effects. J Neurosci. 2006, 26: 11522.
3-21) Fuchs A, Rigaud M, Hogan QH. Painful nerve injury shortens the intracellular Ca2+ signal in axotomized sensory neurons of rats. Anesthesiology. 2007, 107: 106.
3-22) Fujitani T, Adachi N, Miyazaki H et al. Lidocaine protects hippocampal neurons against ischemic damage by preventing increase of extracellular excitatory amino acids: a microdialysis study in Mongolian gerbils. Neurosci Lett. 1994, 179: 91.
3-23) Goldin AL. Diversity of mammalian voltage-gated sodium channels. In: Ruby B, Seeburg P, eds. Molecular and functional diversity of ion channels and receptors. New York: New York Academy of Sciences. 1999: 38.
3-24) Groudine SB, Fisher HA, Kaufman RP, Jr. et al. Intravenous lidocaine speeds the return of bowel function, decreases postoperative pain, and shortens hospital stay in patients undergoing radical retropubic prostatectomy. Anesth Analg. 1998, 86: 235.
3-25) Hagelberg N, Kajander JK, Nagren K et al. Mu-receptor agonism with alfentanil increases striatal dopamine D2 receptor binding in man. Synapse. 2002, 45: 25.

3-26) Hernandez L, Guzman NA, Hoebel BG. Bidirectional microdialysis in vivo shows differential dopaminergic potency of cocaine, procaine and lidocaine in the nucleus accumbens using capillary electrophoresis for calibration of drug outward diffusion. Psychopharmacology (Berl). 1991, 105: 264.
3-27) Hirsch E, Danober L, Simler S et al. The amygdala is critical for seizure propagation from brainstem to forebrain. Neuroscience. 1997, 77: 975.
3-28) Hogan QH. Role of decreased sensory neuron membrane calcium currents in the genesis of neuropathic pain. Croat Med J. 2007, 48: 9.
3-29) Huang JH, Thalhammer JG, Raymond SA, Strichartz GR. Susceptibility to lidocaine of impulses in different somatosensory afferent fibers of rat sciatic nerve. J Pharmacol Exp Ther. 1997, 282: 802.
3-30) Ikeda M, Dohi T, Tsujimoto A. Protection from local anesthetic-induced convulsions by gamma-aminobutyric acid. Anesthesiology. 1982, 56: 365.
3-31) Jonsson A, Cassuto J, Hanson B. Inhibition of burn pain by intravenous lignocaine infusion. Lancet. 1991, 338: 151.
3-32) Kanai Y, Katsuki H, Takasaki M. Graded, irreversible changes in crayfish giant axon as manifestations of lidocaine neurotoxicity in vitro. Anesth Analg. 1998, 86: 569-73.
3-33) Keilholz SD, Silva AC, Raman M et al. Functional MRI of the rodent somatosensory pathway using multislice echo planar imaging. Magn Reson Med. 2004, 52: 89.
3-34) Kida I, Hyder F, Behar KL. Inhibition of voltage-dependent sodium channels suppresses the functional magnetic resonance imaging response to forepaw somatosensory activation in the rodent. J Cereb Blood Flow Metab. 2001, 21: 585.
3-35) Kida I, Smith AJ, Blumenfeld H et al. Lamotrigine suppresses neurophysiological responses to somatosensory stimulation in the rodent. Neuroimage. 2006, 29: 216.
3-36) Kragh J, Bolwig TG, Woldbye DP, Jorgensen OS. Electroconvulsive shock and lidocaine-induced seizures in the rat activate astrocytes as measured by glial fibrillary acidic protein. Biol Psychiatry. 1993, 33: 794.
3-37) Lam AM, Donlon E, Engl CC. The effect of lidocaine on cerebral blood flow and metabolism during normocapnia and hypocapnia in humans. Am Soc Anesthesiologist. 1993, 79: A202.
3-38) Lowe AS, Beech JS, Williams SC. Small animal, whole brain fMRI: innocuous and nociceptive forepaw stimulation. Neuroimage. 2007, 35: 719.
3-39) Mao J, Chen LL. Systemic lidocaine for neuropathic pain relief. Pain. 2000, 87: 7.
3-40) Matharu MS, Cohen AS, Goadsby PJ. SUNCT syndrome responsive to intravenous lidocaine. Cephalalgia. 2004, 24: 985.
3-41) McCallum JB, Kwok WM, Sapunar D et al. Painful peripheral nerve injury decreases calcium current in axotomized sensory neurons. Anesthesiology. 2006, 105: 160.
3-42) Niederlehner JR, DiFazio CA, Foster J, Westfall TC. Cerebral monoamines and lidocaine toxicity in rats. Anesthesiology. 1982, 56: 184-7.
3-43) Petersen KL, Rowbotham MC. Will ion-channel blockers be useful for management of nonneuropathic pain? J Pain. 2000, 1: 26.
3-44) Peyron R, Laurent B, Garcia-Larrea L. Functional imaging of brain responses to pain. A review and meta-analysis. Neurophysiol Clin. 2000, 30: 263.

3-45) Radwan IA, Saito S, Goto F. The neurotoxicity of local anesthetics on growing neurons: a comparative study of lidocaine, bupivacaine, mepivacaine, and ropivacaine. Anesth Analg. 2002, 94: 319.
3-46) Rutter JJ, Baumann MH, Waterhouse BD. Systemically administered cocaine alters stimulus-evoked responses of thalamic somatosensory neurons to perithreshold vibrissae stimulation. Brain Res. 1998, 798: 7.
3-47) Rutter JJ, Devilbiss DM, Waterhouse BD. Effects of systemically administered cocaine on sensory responses to peri-threshold vibrissae stimulation: individual cells, ensemble activity, and animal behaviour. Eur J Neurosci 2005, 22: 3205.
3-48) Rykaczewska-Czerwinska M. Antinociceptive effect of lidocaine in rats. Pharmacol Rep. 2006, 58: 961.
3-49) Sakura S, Bollen AW, Ciriales R, Drasner K. Local anesthetic neurotoxicity does not result from blockade of voltage-gated sodium channels. Anesth Analg. 1995, 81: 338.
3-50) Sakura S, Kirihara Y, Muguruma T et al. The comparative neurotoxicity of intrathecal lidocaine and bupivacaine in rats. Anesth Analg. 2005, 101: 541.
3-51) Shah YB, Haynes L, Prior MJ et al. Functional magnetic resonance imaging studies of opioid receptor-mediated modulation of noxious-evoked BOLD contrast in rats. Psychopharmacology (Berl). 2005, 180: 761.
3-52) Spenger C, Josephson A, Klason T et al. Functional MRI at 4.7 tesla of the rat brain during electric stimulation of forepaw, hindpaw, or tail in single- and multislice experiments. Exp Neurol. 2000, 166: 246.
3-53) Strichartz GR, Zhou Z, Sinnott C, Khodorova A. Therapeutic concentrations of local anaesthetics unveil the potential role of sodium channels in neuropathic pain. Novartis Found Symp. 2002, 241: 189.
3-54) Tanelian DL, MacIver MB. Analgesic concentrations of lidocaine suppress tonic A-delta and C fiber discharges produced by acute injury. Anesthesiology. 1991, 74: 934.
3-55) Thomson AH, Elliott HL, Kelman AW et al. The pharmacokinetics and pharmacodynamics of lignocaine and MEGX in healthy subjects. J Pharmacokinet Biopharm. 1987, 15: 101.
3-56) Tracey I, Becerra L, Chang I et al. Noxious hot and cold stimulation produce common patterns of brain activation in humans: a functional magnetic resonance imaging study. Neurosci Lett. 2000, 288: 159.
3-57) Verkhratsky A. Calcium ions and integration in neural circuits. Acta Physiol (Oxf). 2006, 187: 357.
3-58) Waxman SG, Hains BC. Fire and phantoms after spinal cord injury: Na+ channels and central pain. Trends Neurosci. 2006, 29: 207.
3-59) Wise RG, Rogers R, Painter D et al. Combining fMRI with a pharmacokinetic model to determine which brain areas activated by painful stimulation are specifically modulated by remifentanil. Neuroimage. 2002, 16: 999.
3-60) Wise RG, Williams P, Tracey I. Using fMRI to quantify the time dependence of remifentanil analgesia in the human brain. Neuropsychopharmacology. 2004, 29: 626.
3-61) Woodward JJ, Compton DM, Balster RL, Martin BR. In vitro and in vivo effects of cocaine and selected local anesthetics on the dopamine transporter. Eur J Pharmacol. 1995, 277: 7.
3-62) Yamashita A, Matsumoto M, Matsumoto S et al. A comparison of the neurotoxic effects on the spinal cord of tetracaine, lidocaine, bupivacaine, and ropivacaine administered intrathecally in rabbits. Anesth Analg. 2003, 97: 512.

3-63) Zhao P, Waxman SG, Hains BC. Sodium channel expression in the ventral posterolateral nucleus of the thalamus after peripheral nerve injury. Mol Pain. 2006, 2: 27.

# Chapter 4 Optical Coherence Doppler Tomography Quantifies Laser Speckle Contrast Imaging for Blood Flow in Rat Cerebral Cortex

## 4.1 Introduction

Laser Doppler techniques have long been used to measure microscopic blood flow such as LCBF *in vivo*. Recently, laser speckle contrast imaging (LSCI), a full-field approach to extract flow speed by virtue of laser speckle contrast change, was applied to map neuronal activations in response to functional challenges in rat brain [Dunn, 2003; Durduran, 2004]. This imaging modality is able to achieve high spatiotemporal resolution; however, like any other homodyne laser Doppler technique, it fails to discriminate flow direction and only measures the *en face* relative flow change. Nevertheless, the apparent merits of LSCI (e.g., high spatiotemporal resolution, simplicity, and cost effectiveness) have recently attracted great efforts to quantify its measurement, including attempts to use phantom calibration and MRI perfusion imaging [Choi, 2006; Barbier, 2001]. On the other hand, spectral-domain Doppler optical coherence tomography (SDOCT) is a new heterodyne technique that enables spatially resolved Doppler frequency-shifted flow imaging[Leitgeb, 2003], thus potentially rendering directional and absolute blood flow imaging in 2D and even 3D[Wang, 2007]. Here we propose to use 2D SDOCT to quantify LSCI by correlating co-registered cortical arterial blood flow, and present experimental data of tissue phantom study and *in vivo* animal study using cocaine-induced cerebral blood flow changes in rat cortical brain for proof of concept.

## 4.2 Methods and Materials

Fig. 4-1(a,b) shows a schematic diagram and a picture of the dual-imaging setup which combines SDOCT and LSCI for high-resolution quantitative rat cortical LCBF imaging. As the principles of SDOCT and LSCI have been previously reported [Dunn, 2003; Choi, 2006], only a brief summary is outlined here. For SDOCT, a broadband source with pigtailed output power of 18mW was employed to illuminate a fiber-optic Michelson interferometer which equally split light between sample and reference arms. The reference arm was connected to a stationary mirror to match the optical pathlengths between two arms. The sample arm was connected to a handheld probe in which light exiting the fiber was collimated to ϕ5mm, scanned laterally by a servo mirror, and focused by an achromate (f=40mm) onto rat cortical surface under imaging. A green laser (532nm, 2mW) was coupled into the input arm via a 95%:5% coupler to ensure SDOCT scan across cortical arteries. The detection arm was connected to a spectral radar in which light was collimated to ϕ10mm, diffracted by a holographic grating (d=1200/ mm) and then focused by a lens system (f=120mm)

onto a linear InGaAs photodiode array (1k pixels). Each detected spectral graph for a lateral position x, including spectrally encoded interference fringes from different depths within rat cortex was digitized, rescaled to k(=2π/λ) domain, and converted to an A-scan $I_x(z)$ by inverse complex FFT at a line rate of $f_T \approx 7.7$kHz. Subsurface Doppler flow velocity $v_x(z)$ could be acquired by extracting the phase shift $\Delta\phi_x(z,\tau)$ between adjacent A-scan [Leitgeb, 2003].

$$\Delta\phi_x(z,\tau) = \tan^{-1}\left(\frac{\mathrm{Im}[I_x(z,\tau)]}{\mathrm{Re}[I_x(z,\tau)]}\right) - \tan^{-1}\left(\frac{\mathrm{Im}[I_x(z)]}{\mathrm{Re}[I_x(z)]}\right) \tag{4-1}$$

$$v_x(z) = \lambda_0 \Delta\phi_x(z,\tau)/4\pi n\cos(\theta) \tag{4-2}$$

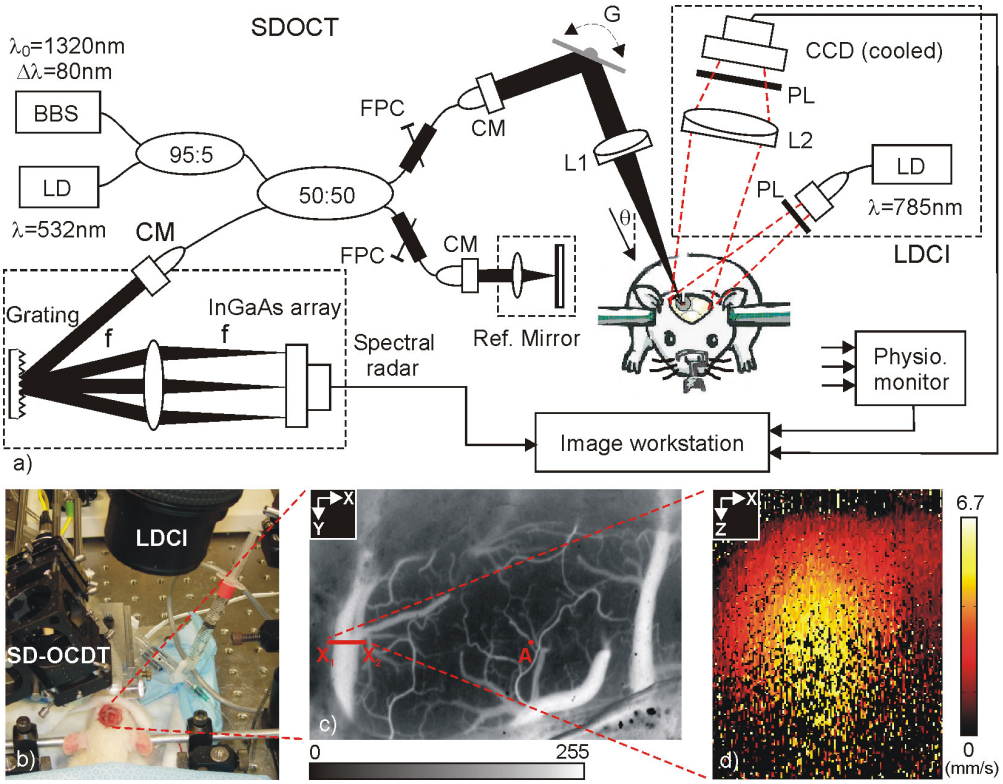


Fig. 4-1 (a, b) A sketch/picture of a dual-modality flow imaging setup, c) A LSCI of a rat cortex (image size: 5×4mm$^2$), and d) SDOCT of a ~ϕ300um artery across $x_1$-$x_2$ (image size: 380×440μm$^2$). BBS; broadband source, LD: diode laser, CM: fiberoptic collimator, G: servo mirror, L1, L2: lenses, PL: polarizer, θ≈68$^0$: incline angle with flood flow.

where θ was the angle with the blood flow and $\tau = 1/f_T \approx 0.13$ms was the interval. Averaging $\Delta\phi_x(z,\tau)$ over 4 scans was implemented to reduce phase noise. Then, the servo mirror was scanned to the next lateral position until a 2D cross-sectional flow image was completed and displayed in pseudo color. Although the axial/lateral resolutions of structural OCT were roughly 10μm, it was found that SDOCT barely detected arteriolar flows with size ϕ<80μm due to limited phase detection sensitivity.

For LSCI, a stabilized diode laser (785nm, 50mW) was used to illuminate the rat cortical surface at an angle of 45°. A fast macro lens (f/105mm, F#/2.8) was used to relay the cortical surface image to an air-cooled CCD camera (12-bit, 6.45μm/pixel) at an exposure time of T=10ms controlled by the image workstation via IEEE-1394 interface to acquire laser speckle images. Post-processing was performed to reconstruct LSCI which included 5×5 pixel binning to calculate regional laser speckle contrast/fluctuation K(x,y)=σ(x,y)/I(x,y), i.e., defined as the ratio between standard deviation σ and mean of binned pixel intensity I. K(x,y) has been previously derived[Dunn, 2003; Durduran, 2004], i.e.:

$$K^2(x,y) = \frac{\exp\left(-2Tak < v^2(x,y) >^{1/2}\right) - 1 + 2Tak < v^2(x,y) >^{1/2}}{2 \cdot [Tak < v^2(x,y) >^{1/2}]^2} \qquad (4\text{-}3)$$

to relate the flow in a form of mean-square-rooted speed $<v^2(x,y)>^{1/2}$ of the scattering particles, where $k=2\pi/\lambda$. However, $a$ was an unknown parameter related to the optical properties and speed distribution of the flow media; thus, the combined flow speed index $a<v^2(x,y)>^{1/2}$ was numerically solved in Eq.(4-2) as the apparent flow output of LSCI, which is apparently relative measurement. The sensitivity of LSCI could be changed by adjusting T for different flow range [Choi, 2006], and the theoretical resolution of LSCI was ~30um (i.e., 5×6.45μm).

### 4.3 Results

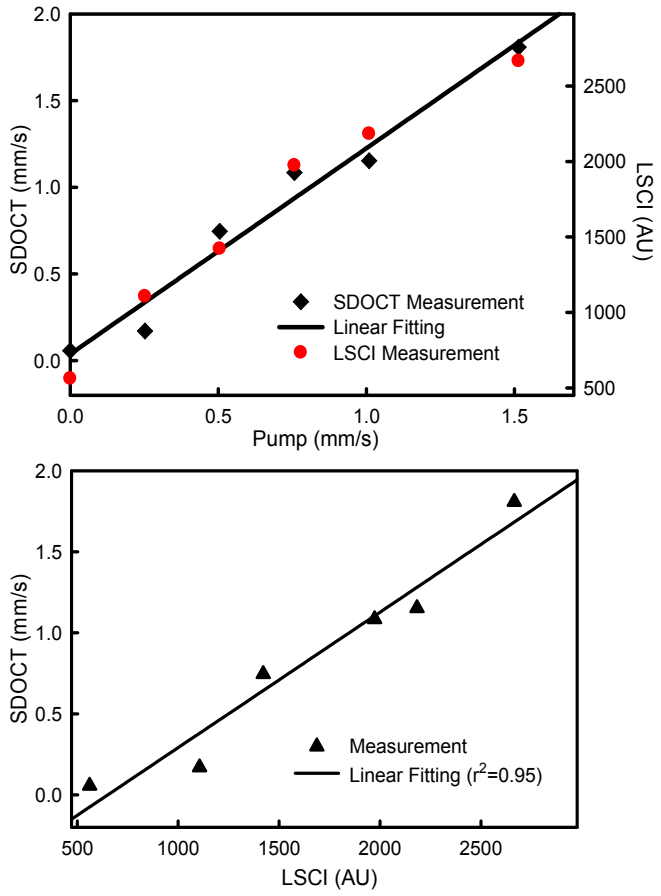


Fig. 4-2 Result of phantom flow. a) SDOCT and LSCI data vs. flow pump, b) Least-square-fit calibration. A ϕ580μm polyethylene tubing with 1% intralipid was used.

The relative flow measurement $a\langle v^2(x,y)\rangle^{1/2}$ of LSCI can be calibrated by SDOCT. For proof of concept, we performed phantom study, and Fig. 4-2 shows the result of simultaneous SDOCT and LSCI measurements of a 1%-Intralipid flow in a transparent polyethylene tubing (ϕ580um) driven by a precision pump for flow calibration. The result of least square fit (r=0.97) indicates that the relative LSCI flow change can be accurately quantified by SDOCT.

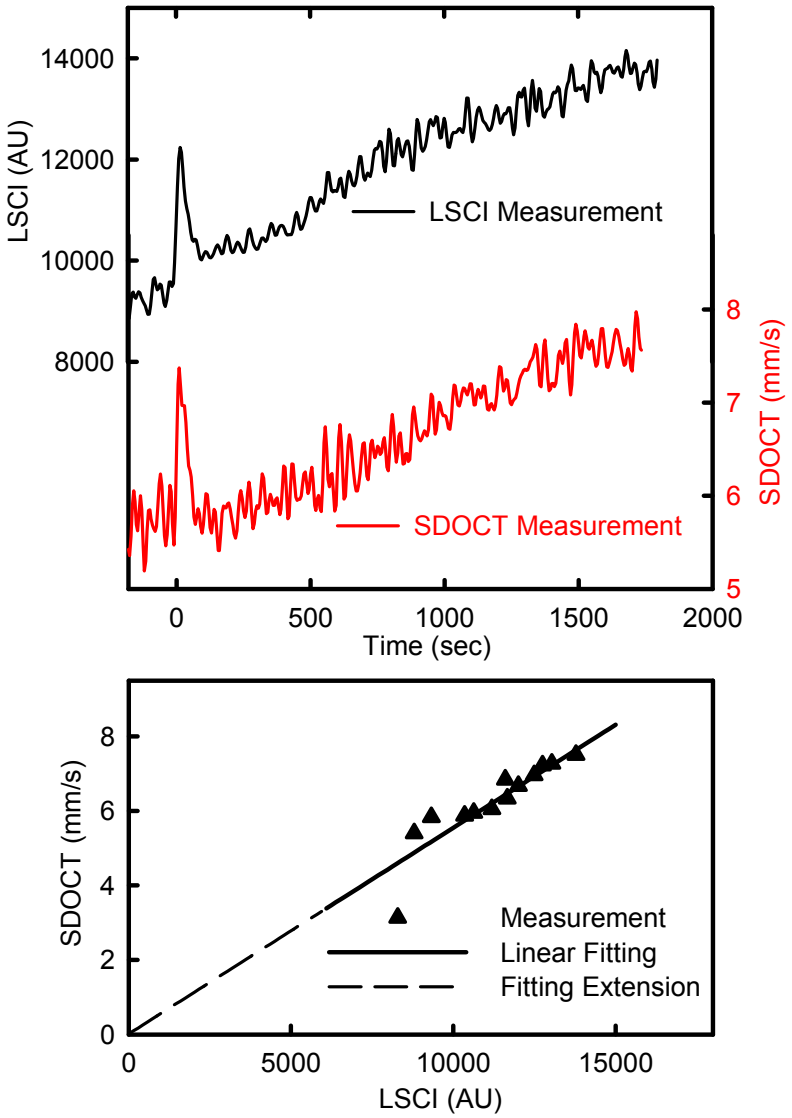


Fig. 4-3 Result of in vivo rat study under cocaine challenge. a) SDOCT and LSCI data vs. time (cocaine induction at t=0s). b) Least-square-fit calibration. Peristaltic pulsate variations in the measured flow data were smoothed by digital data processing to enhance least square fit.

To further test the utility of this quantification approach for *in vivo* imaging, we performed animal study to track cocaine-induced LCBF changes in rat brain cortex. In

this experiment, a Sprague-Dawley rat (female, 250g) was anesthetized with 2~3% isoflurane and mounted stereotaxically during which its femoral and tail veins were catheterized for drug induction and a femoral artery was catheterized for blood pressure monitoring during the study. A ~ϕ5mm cranial window was created on the rat cortex and dura mater was removed to expose the brain surface which was kept moist with saline under a slightly-tilted 160μm-thick microscopic cover glass to minimize specular reflection or surface scattering. Then, inhalational isoflurane was curtailed and anesthesia was switched to α-chloralose infusion via femoral vein (~6.25mg/hr). Physiological conditions of the rat, e.g., ECG, blood pressure, respiration, and temperature (37°C) were monitored and displayed on the image workstation. One bolus of cocaine (1mg/kg) was administrated through the tail vein followed by an immediate flush of 1ml saline, during which simultaneous SDOCT and LSCI image sequences were recorded at 5s interval for 35 minutes (totaling 420 frames/each) to track LCBF response to cocaine. Fig. 4-1(c) shows a full-field LSCI image in which a cerebral artery at $x_1$-$x_2$ was chosen as ROI for quantification, and a cross-sectional SDOCT image is shown in Fig. 4-1(d). The measured time courses of blood flow response to cocaine in this artery are plotted in Fig. 4-3, showing excellent correlation between LSCI and SDOCT data based on least square fit (r=0.94). Therefore, the relative LSCI data can be accurately quantified. Assume LSCI has a linear response in the LCBF flow range[Choi, 2006], smaller cortical cerebral arteriolar flows can be quantified by a linear extrapolation, and Fig. 4-4 show the quantified curves of the arterial flow in Fig. 4-3 and an arteriolar flow at A in Fig. 4-1(b).

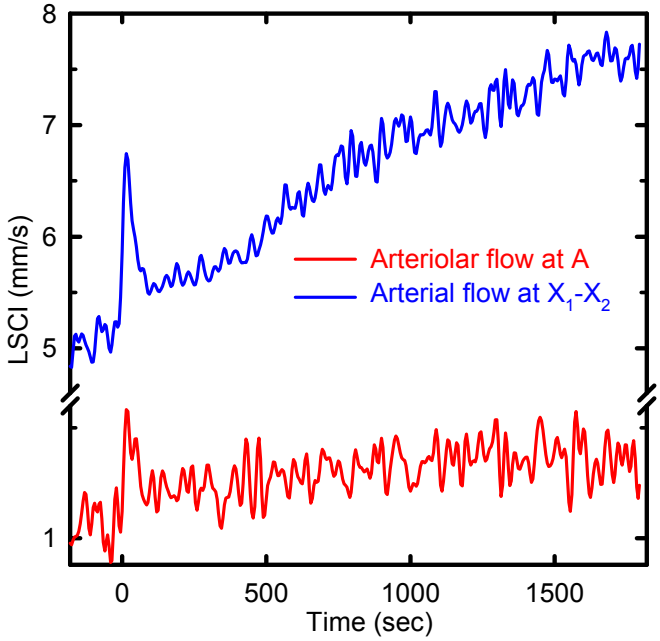


Fig. 4-4 Quantified LSCI results of the arterial flow in Fig. 4-3 and an arteriolar flow (~ϕ30μm) at spot A. Cocaine-induced flow increases in the small arteriole and in the artery are about 49% and 53%, respectively.

## 4.4 Summary

In summary, we provide experimental evidence based on phantom and *in vivo* animal studies to demonstrate that the relative flow measurement of LSCI can be accurately quantified with SDOCT ($r^2 \approx 0.96$). The dual-imaging system in Fig. 4-1 can be easily integrated by using a dichromatic mirror to ease the optical alignment. Although SDOCT calibration is based on linear extrapolation, the quantified flow rate for a small arteriole (Fig. 4-4) falls into the physiologic range previously reported; nevertheless, we plan to further validate the quantification by performing fluorescence video microscopy. Quantification of LSCI for cerebral blood flow imaging is of significance to the quantitative analyses of the spatiotemporal hemodynamics of functional brain activations and thus improved understanding of neural process.

## 4.5 List of References


4-1) Barbier E, Silva A, Kim S, Koretsky A. Perfusion imaging using dynamic arterial spin labeling (DASL). Mag. Res. in Med. 2001, 45: 1021.

4-2) Choi B, Ramirez-San-Juan J, Lotfi J, Nelson J. Linear response range characterization and in vivo application of laser speckle imaging of blood flow dynamics. JBO. 2006, 11: 1.

4-3) Dunn A, Devor A, Bolay H, et al. Simultaneous imaging of total cerebral hemoglobin concentration, oxygenation, and blood flow during functional activation. Opt. Lett. 2003, 28: 28.

4-4) Durduran T, Burnett M, Yu G, Zhou C, et al. Spatiotemporal Quantification of Cerebral Blood Flow During Functional Activation in Rat Somatosensory Cortex Using Laser-Speckle Flowmetry. J. Cereb. Blood Flow Metab. 2004, 24: 518.

4-5) Kleinfeld D, Mitra P, Helmchen F, Denk W. Fluctuations and stimulus-induced changes in blood flow observed in individual capillaries in layers 2 through 4 of rat neocortex. PNAS. 1998, 95: 15741.

4-6) Leitgeb R, Schmetterer L, Drexler W, Fercher A. Real-time assessment of retinal blood flow with ultrafast acquisition by color Doppler Fourier domain optical coherence tomography. Opt. Ex. 2003, 11: 3116.

4-7) Wang R, Jacques S, and Ma1 Z, et al. Three dimensional optical angiography. Opt. Ex. 2007, 15: 4083.

# Chapter 5 Quantification of Cocaine-Induced Cortical Blood Flow Changes Using Laser Speckle Contrast Imaging and Doppler Optical Coherence Tomography

## 5.1 Introduction

Cocaine is one of the most commonly abused psychostimulants and it evokes widespread and elusive neuronal and metabolic activity across the brain [Bardo, 1998; Marota, 2000; Schmidt, 2006]. Moreover, cocaine abuse can induce arterial spasm, vasculitis, and acute hypertension [Brust, 1997; Martinez, 1996], thus severely increasing the risk of life-threatening neurological complications, such as hemorrhagic stroke, seizures, and transient ischemia [Buttner, 2003]. Advanced medical imaging techniques have been shown to offer great potential to investigate the changes of neuronal–metabolic–vascular reactions induced by cocaine and provide important insight into the mechanisms leading to cocaine abuse and, thus, improved treatment effects.

Several imaging techniques, such as functional magnetic resonance imaging (fMRI), positron emission tomography (PET), and single-photon-emission computed tomography (SPECT), have been widely used to study brain functional changes induced by stimulants, including cocaine [Marota, 2000; Schmidt, 2006, Gollub, 1998; Kaufman, 1998; London, 1990; Pearlson, 1993; Wallace, 1996]. A recent full-field optical modality, laser speckle contrast imaging (LSCI), which uses laser speckle contrast to represent cerebral flows, has been employed to map neuronal activations in rat brain [Briers, 1996; Briers, 2001; Durduran, 2004; Dunn, 2005]. Compared to functional MRI and SPECT/PET, the unique merits of LSCI lie in its high detection sensitivity and superior spatiotemporal resolutions, e.g., sub-100 μm and up to 100 frames per second (fps). In recent years, LSCI has been extensively used for in-vivo imaging of microvascular dynamics in normal and diseased organs, especially for mapping neurovascular coupling in the central nervous system [Durduran, 2004; Dunn, 2005]. However, LSCI can only measure *en face* relative flow changes and fails to discriminate flow directions due to its homodyne nature and multiple scattering of tissue (e.g., brain); therefore, calibration is needed to provide quantitative measurements [Briers, 1996; Briers, 2001]. On the other hand, spectral-domain Doppler optical coherence tomography (SDOCT) is a heterodyne detection technique that potentially enables two dimensional (2D) and even three-dimensional (3D) quantitative flow imaging (i.e., absolute flow measurement). Because of inherent phase noise, the high spatial resolution and sensitivity of SDOCT may be compromised in minute blood flow detection and quantification, although recent technological advances have shown great promise of improvement [Wang, 2007]. It was recently demonstrated that the cortical cerebral blood flow (CBF) obtained by LSCI could be calibrated by spatiotemporal coregistration and correlation with the absolute flow image acquired by SDOCT [Luo, 2008]. In this study, we further examined the utility of SDOCT-calibrated LSCI in quantitative analysis of local CBF changes in the parietal cortex of rats and characterization of the spatiotemporal responses to systemic

cocaine challenge.

## 5.2 Materials and Methods

### *5.2.1 Animal preparation and Experimental Protocol*

Cocaine-naïve female Sprague–Dawley rats (250–300 g each) were anesthetized with inhalational gas consisting of 50% oxygen-enriched air mixed with 1.0–1.5% isoflurane vapor during the surgical procedure. With the rat mounted on a stereotaxic frame, a ~ϕ5mm cranial window was created on one lateral side of the parietal bone that exposed the somatosensory and motor cortex area. The dura membrane was removed and the exposed brain surface was immediately submerged in saline to reduce surface scattering and specular reflection. Throughout the surgical and imaging procedures, the arterial blood pressure (ABP) and body temperature of the rat were continuously monitored (PC-SAM monitor, SA Inc.) and the blood gas was periodically measured (ABL 700, Radiometer Medical) to ensure the rat was under normal physiological condition (pH=7:35–7:40, $PCO_2$=35–45mmHg, $StO_2$=97:5–100%, mean ABP=80–100mmHg, T=36:5–37:5 °C).

Two different regimes of anesthetics were used. For rats (n=4) in group A, anesthesia were induced by isoflurane during the surgery and then switched to α-chloralose using an initial bolus of 50mg/kg followed by continuous infusion of 25mg/kg/h through the femoral vein during the experiment. Rats (n=4) in group B were anesthetized by isoflurane throughout the entire experiment. When the physiological condition of the rat was stabilized, LSCI was initiated to measure the baseline CBF and the changes after a bolus of cocaine (1mg/kg) was administrated through the tail vein followed by a 0.5 cc saline flush.

### *5.2.2 Image Acquisition*

Fig. 5-1 illustrates the experimental setup that allowed for simultaneous LSCI and SDOCT imaging of cortical blood flows of the rat. In the LSCI system, light from a 785nm single-mode laser diode (HL7851G, Hitachi) was quasi-collimated (ϕ5mm) to illuminate the exposed brain surface at an angle of 30° off the normal direction. A macrolens (1×, f-number 2.8) above the cranial window relayed the brain surface image onto a 12 bit monochromatic CCD camera (Retiga-Ex, pixel size 6:45 μm). The exposure duration ($T$) was set to 10 ms and the acquired image sequence was transferred to a PC via an IEEE-1394 interface. To extract flow from the raw images featured with speckle patterns, a square binning of 5×5 pixels was conducted over each individual frame to compute the speckle contrast map ($K$) by dividing the standard deviation ($\sigma$) against the mean intensity ($\langle I \rangle$) within each square. As has been previously reported [Briers, 1996; Briers, 2001], $K$ can be derived as a function of $T/\tau_C$, i.e.,

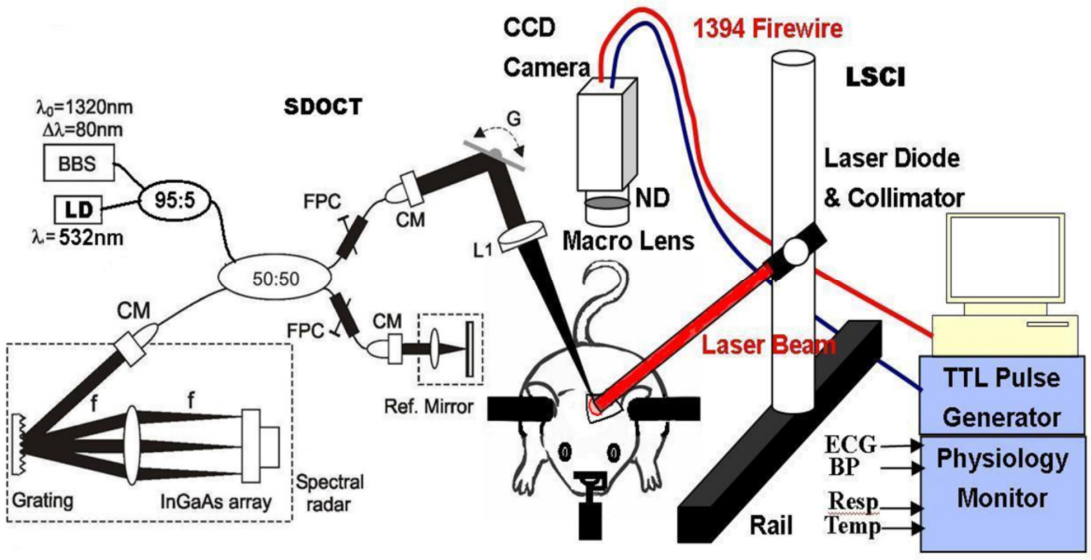


Fig.5-1 Sketch of the dual-imaging setup combining SDOCT and LSCI for quantitative blood flow imaging. LD: diode laser, BBS: broadband source, CM: fiberoptic collimator, G: servo mirror, L1: lens.

$$K(x,y,t)=\frac{\sigma(x,y,t)}{<I>(x,y,t)}=\frac{\tau_C(x,y,t)}{T}\sqrt{\frac{1}{2}\cdot\left[\exp\left(-\frac{2T}{\tau_C(x,y,t)}\right)-1+\frac{2T}{\tau_C(x,y,t)}\right]} \quad (5\text{-}1)$$

where $\tau_C$ is the autocorrelation time of the speckle intensity fluctuation which is inversely proportional to the root of mean square (RMS) speed of the scattering particles ($<v^2>^{1/2}$) [Briers, 1996; Briers, 2001]

$$\tau_C=\frac{1}{ak<v^2>^{1/2}} \quad (5\text{-}2)$$

$k=2\pi/\lambda$ is the wave number of light and $a$ is a unit-less factor related to the speed distribution and tissue scattering properties. Substituting $\tau_C$ in Eq.(5-2) into Eq.(5-1) yields,

$$K=\frac{1}{Tak<v^2>^{1/2}}\sqrt{\frac{\exp\left(-2Tak<v^2>^{1/2}\right)-1+2Tak<v^2>^{1/2}}{2}} \quad (5\text{-}3)$$

which indicates that the flow index $a<v^2(x,y)>^{1/2}$ can be derived from the measured $K$ image. However, the binning process (i.e., 5x5 pixel window) reduces the resolution of flow mapping to approximately 32μm (i.e., 5x6.45μm).

In the SDOCT system, a pigtailed broadband light source (18mW, $\lambda_0$=1320nm, $\Delta\lambda_{FWHM}$=90nm) was employed to illuminate a fiberoptic Michelson interferometer which split the light equally between sample and reference arms. The path length difference and the polarization state in the two arms were matched using a stationary mirror in the reference arm and two fiber polarization controllers (FPC. In the sample arm, light exiting the fiber was collimated (ϕ5mm), scanned laterally by a servo mirror, and focused onto the cortical surface at an incline angle of θ=31°. In the detection fiber, light returning from both arms was recombined and connected to a spectral imager in which it

was collimated, diffracted by a holographic grating (d=1200/mm) and focused onto a linear InGaAs photodiode array (1024 pixels with 25μm pitch, readout rate: $f_L$=7.7k line/s, Sensors Unlimited Inc.). At each lateral position $x$, the spectrograph which encoded interference fringes from different depths $z$ within the rat cortex in $k$-domain, could be converted to a complex A-line or depth profile $I_x(z,t)$ by inverse FFT. A consecutive A-scan $I_x(z, \tau_L)$ with an interval $\tau_L$ ($\tau_L$=1/$f_L$=0.13ms) was acquired to extract the Doppler frequency shift and thus the flow speed $v_x(z)$ can be derived as [Leitgeb, 2003]:

$$v_x(z) = \frac{\tan^{-1}\left\{\mathrm{Im}[I_x(z,\tau_L)]/\mathrm{Re}[I_x(z,\tau_L)]\right\} - \tan^{-1}\left\{\mathrm{Im}[I_x(z)]/\mathrm{Re}[I_x(z)]\right\}}{2k\tau_L\cos\theta} \quad (5\text{-}4)$$

$v_x(z)$ was often averaged over 4 consecutive scans to reduce phase noises. This procedure was repeated for all $x$ to form 2D and even 3D cross-sectional flow images. For a known θ (extracted from the spatial shift of the flow centers of 2 adjacent SDOCT images), $v_x(z)$ could be accurately obtained. Since both the relative speed index $a\langle v^2(x,y)\rangle^{1/2}$ and absolute flow rate $v_x(z)$ were co-registered spatiotemporally, i.e., measured simultaneously from the selected cortical vessels using LSCI and SDOCT, the time course of these two measurements could be correlated using least squares fitting and therefore the relative flow index $a\langle v^2(x,y)\rangle^{1/2}$ could be calibrated to quantify $\langle v^2(x,y)\rangle^{1/2}$. (denoted as calibrated flow speed or $v_c(x,y)$ hereafter)

Fig.5-2 shows typical LSCI (a) and SDOCT (c) images. LSCI provides *en face* blood flow image with a large field of view (FOV), whereas SDOCT provides cross-sectional flow images with detailed flow profile across a vessel section x1-x2 (ϕ400μm, highlighted by red arrows in Fig. 5-2(a)). To co-register these two flow images spatiotemporally, the exposure of the two systems was synchronized by an external TTL triggering signal; in the meantime, a green laser was scanned collinearly with the SDOCT beam (invisible), thus allowing accurate location of the lateral position of the SDOCT scan (Fig.5-2(c)) over the vessel network within the LSCI image (Fig.5-2(a)). To calibrate the relative flow change measured by LSCI, we extracted the averaged time course of flow speed from the selected section x1-x2 in the SDOCT images (Fig.5-2(c)), as well as its counterpart in LSCI images (Fig.5-2(b)). The two time courses were linearly fitted with least square method as shown in Fig.5-2(d), and then the fitting coefficients were used to convert all the flow indices in the LSCI images to quantitative flow speeds [Luo, 2008]. It is noteworthy that to avoid overwhelming data storage and processing incurred due to long duration of vascular response in the cortical brain (e.g., >20min), both LSCI and SDOCT images were captured at every 5s over the 35min recording period for each rat, which was sufficient to preserve the dynamic features of the cocaine-induced CBF variations.

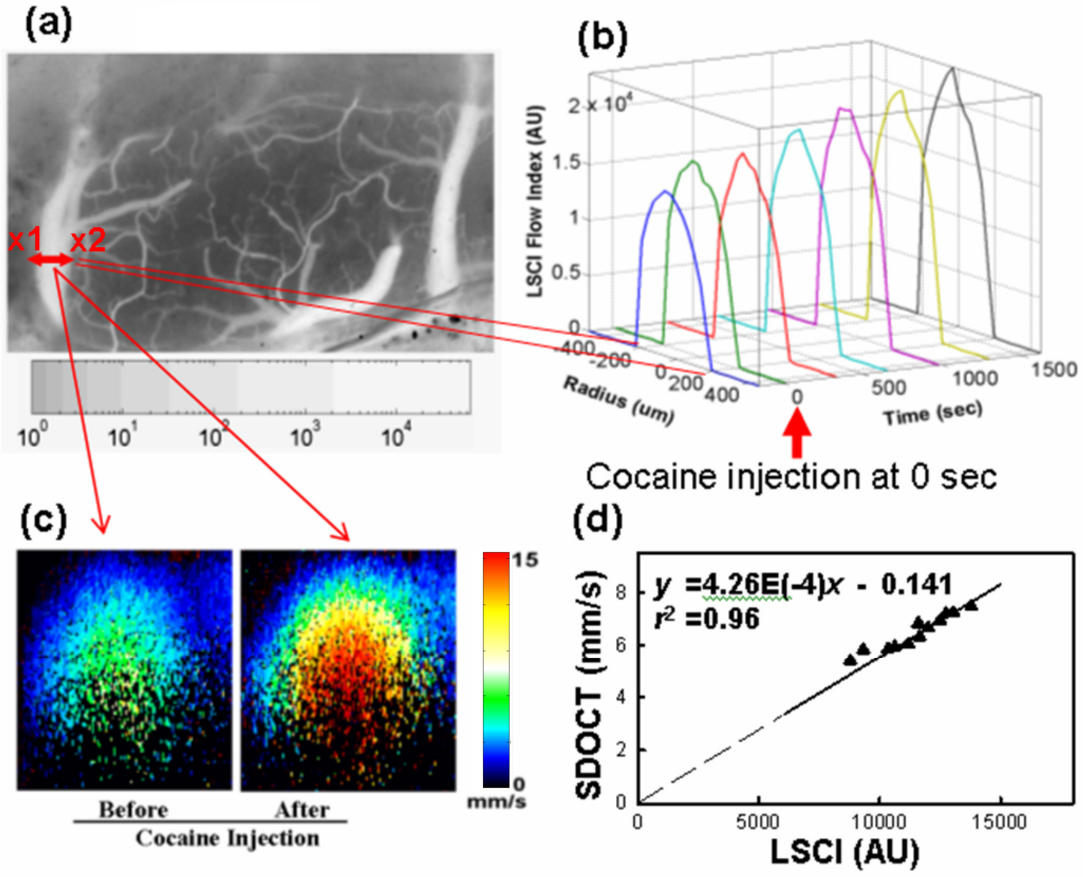


Fig.5-2 Simultaneous LSCI and SDOCT imaging for blood flow quantification. (a) *en face* LSCI image of flow speed index; (b) LSCI profiles of flow index (AU, relative measurement) across a vessel section highlighted (labeled as x1-x2) in panel (a) before and after cocaine challenge; (c) quantitative cross-sectional SDOCT flow profiles across the same section x1-x2 prior to and post cocaine administration; (d) calibration curve derived from the least squares fit ($r^2$=0.96) between panels (b, c) to quantify LSCI flow index.

*5.2.3 Data Analysis*:

To determine the statistical significance of cocaine-induced cortical CBF changes, a t-test of the flow map $\langle v^2(x,y)\rangle^{1/2}$ in Eq.(5-3) was performed at each binned pixel, i.e.,

$$t(x,y)=\frac{\langle v_{ct}(x,y)\rangle-\langle v_{ct0}(x,y)\rangle}{\sqrt{\frac{S_t^2\cdot(n_t-1)+S_{t0}^2\cdot(n_{t0}-1)}{(n_t-1)+(n_{t0}-1)}\left(\frac{1}{n_t}+\frac{1}{n_{t0}}\right)}} \tag{5-5}$$

where $\langle v_{ct0}(x,y)\rangle$, $\langle v_{ct}(x,y)\rangle$ were the calibrated mean flow speed averaged before (baseline) and after cocaine injection, and $S_{t0}$ and $S_t$ were the standard deviations, respectively. $n_{t0}$ and $n_t$ were the numbers of frames acquired during the two periods. Only those pixels with t-values higher than a threshold (associated with a significance $p<0.05$) were considered statistically significant for LCBF responses to cocaine injection, and accordingly a Boolean map of cocaine activation could be generated as has been

commonly used for further pharmacological analysis.

## 5.3 Results

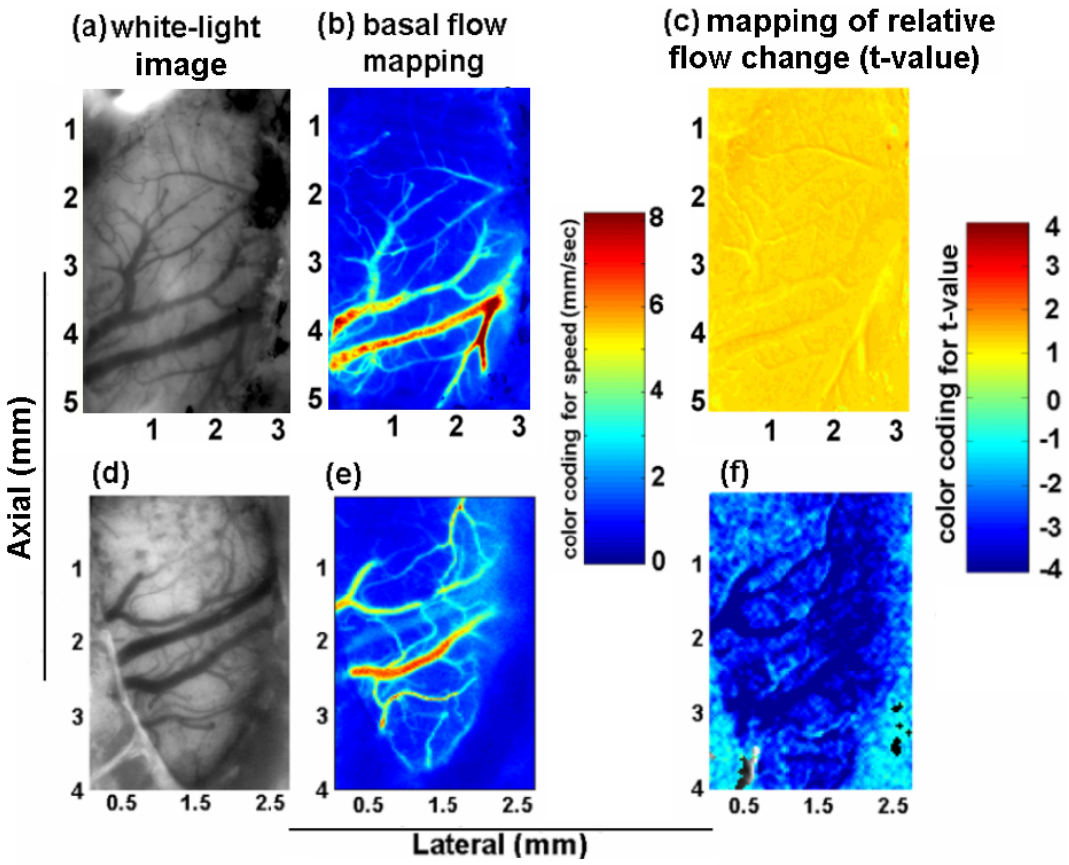


Fig.5-3 Cocaine-induced cortical CBF changes under α-chloralose anesthesia (upper row) and isoflurane anesthesia (bottom row). (a, d): white-light images of the cranial window; (b, e): quantified baseline cortical CBF images prior to cocaine challenge; (c, e) t-value mapping superimposed on the cortical CBF images.

Fig.5-3 (a-c) are the images obtained from a rat cortex anesthetized by α-chloralose, whereas the Fig.5-3 (d-f) are the counterparts anesthetized by isofluorane. Fig.5-3(a, d) show the white-light images of the craniotomy of rat brains and Fig.5-3(b, e) are typical quantified basal cerebral blood flows derived from SDOCT-calibrated LSCI as described above. Fig.5-3 (c, f) show major cortical CBF changes (as indicated by the mapping of t-values) in response to cocaine challenge under both α-chloralose and isoflurane anesthesia. From the color tunes of the two t-value maps, it is clear that, with α-chloralose (c), the CBF primarily increased following cocaine administration, while, with isoflurane (f), the CBF in the cortex primarily decreased in response to IV cocaine, indicating that the anesthetic regime modified the response of cortical CBF to cocaine.

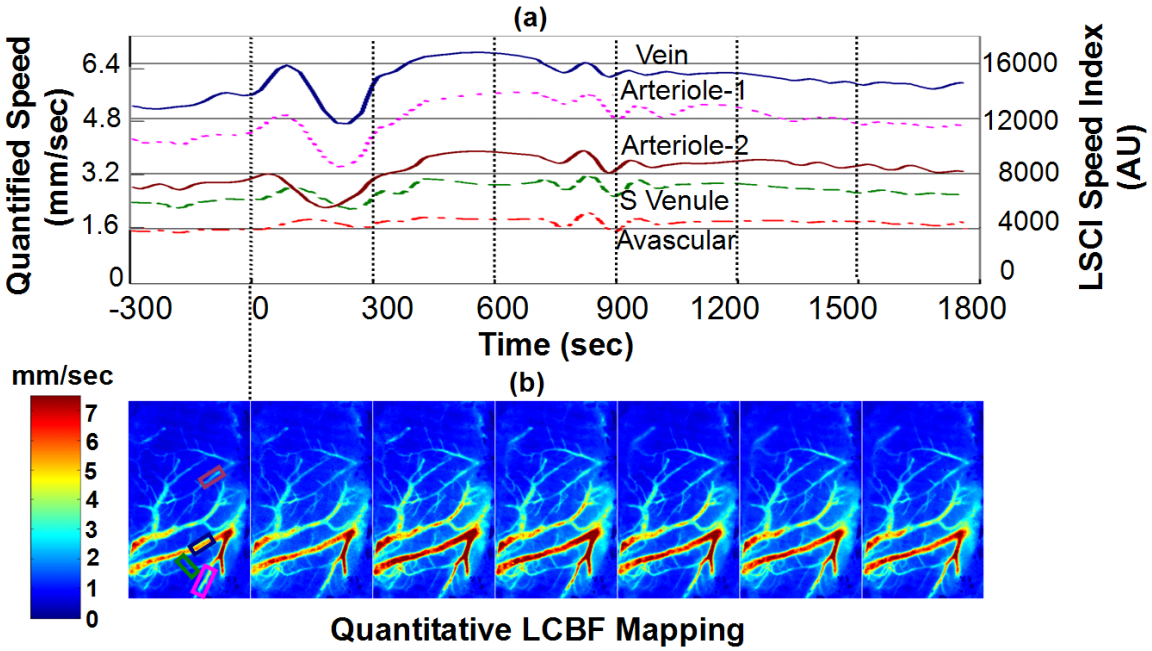


Fig.5-4 Measured spatiotemporal dynamics of cortical LCBF in response to cocaine challenge (IV injection at t=0s) in a rat under α-chloralose anesthesia. (a) cocaine-evoked cortical CBF changes with time acquired from two arterioles (magenta and brown), a vein (blue) and a venule (green) and the avascular (tissue) region (red); (b) quantified time-lapse cortical CBF maps, each averaged over the time frames within the dotted time grids.

Fig.5-4 shows an example of cocaine-induced CBF changes in vascular and avascular regions with time in α-chloralose anesthetized rats and the corresponding time lapsed and quantified CBF maps following cocaine challenge. Under α-chloralose anesthesia, the CBF time courses in almost all vascular compartments of the cortex underwent a transient ±18% fluctuation in the first 5 min immediately following the cocaine and saline flush given intravenously, then rose to a plateau 28%~35% above the baseline, which lasted for another 5 min and then very slowly declined towards the baseline over a period more than 30 min (not completely shown here). More specifically, the CBF in the two arterioles rose 33-35% above the baseline, from 4.3mm/s to 5.8mm/s in arteriol-1 (magenta, ϕ~100μm) and from 2.9 mm/s to 4.0mm/s in arteriole-2 (brown, ϕ~70μm). The CBF in the vein (blue, ϕ~220μm) increased 28% from 5.4mm/s to 7.2mm/s, and increased 34% in the small venule (green, ϕ~30μm) from 2.4mm/s to 3.2mm/s and that in the avascular region (red) increased ~33% from 1.5mm/s to 2.1mm/s.

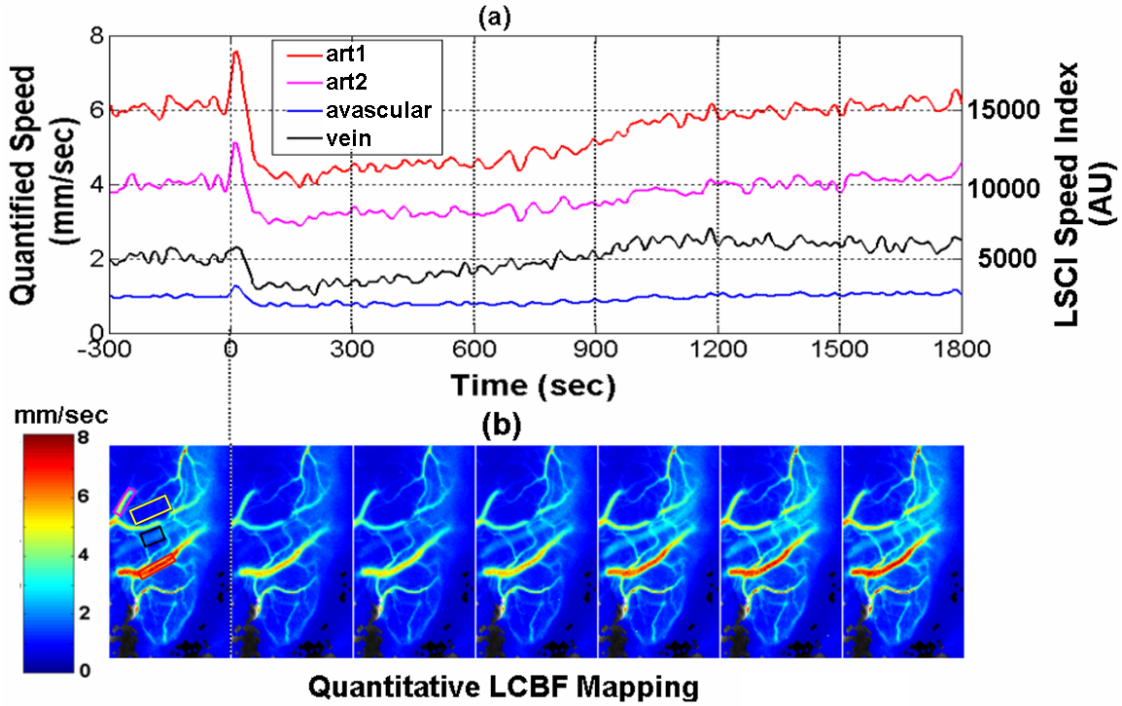


Fig.5-5 Measured spatiotemporal dynamics of cortical LCBF in response to cocaine challenge (IV injection at t=0s) in a rat under isoflurane anesthesia. (a) cocaine-evoked cortical CBF changes with time acquired from two arterioles (art1, art2: red, magenta marks), a veinule (black mark) and an avascular region(yellow mark); (b) quantified time-lapse cortical CBF maps, each averaged over the time frames within the dotted time grids.

Fig.5-5 plots the time course of the quantified cortical CBF change (a) and the time lapsed flow map (b) in response to cocaine challenge in an isoflurane anesthetized rat. In contrast to the α-chloralose group, a rapid decrease of CBF was observed in the first 1-2 min following IV cocaine and saline injection along the vascular and avascular regions, which is followed by a timely recovery to the basal level in 10-15 minutes after cocaine injection. More specifically, the CBF of the arterioles dropped 25-34% below the baseline, e.g, from 6mm/s to 4mm/s in arteriole-1 (red mark, ϕ~240μm) and from 4mm/s to 3mm/s in arteriole-2 (magenta mark, ϕ~150μm). The CBF in a veinule (black mark, ϕ~220μm) reduced by ~35% from 2mm/s to 1.3mm/s and that in the avascular region (yellow mark) dropped ~25% from 1mm/s to 0.75mm/s.

Fig.5-6 summarizes the changes of the mean arterial blood pressure (MABP) and the cortical CBF in the vascular and avascular regions in both α-chloralose and isoflurane anesthetized rats. Cocaine induced an transient MABP increase (Fig.5-6 (a)) from 108.6±13mmHg to 127.8±10mmHg in the α-chloralose group (A, n=4); whereas it induced a dropping in MABP (Fig.5-6 (d)) from 100.2±4.3mmHg to 70.5±7.4mmHg in the isoflurane group (B, n=4). Both started to return to the basal pressure level ~8 minutes after cocaine challenge. The CBF declining in group B (Fig.5-6 (e,f)) behaved very similarly to the contemporary MABP dropping, however the CBF increase in group A (Fig.5-6 (b,c)) seemed to be independent of the early MABP rising, by lagging 10 min

after a fluctuation.

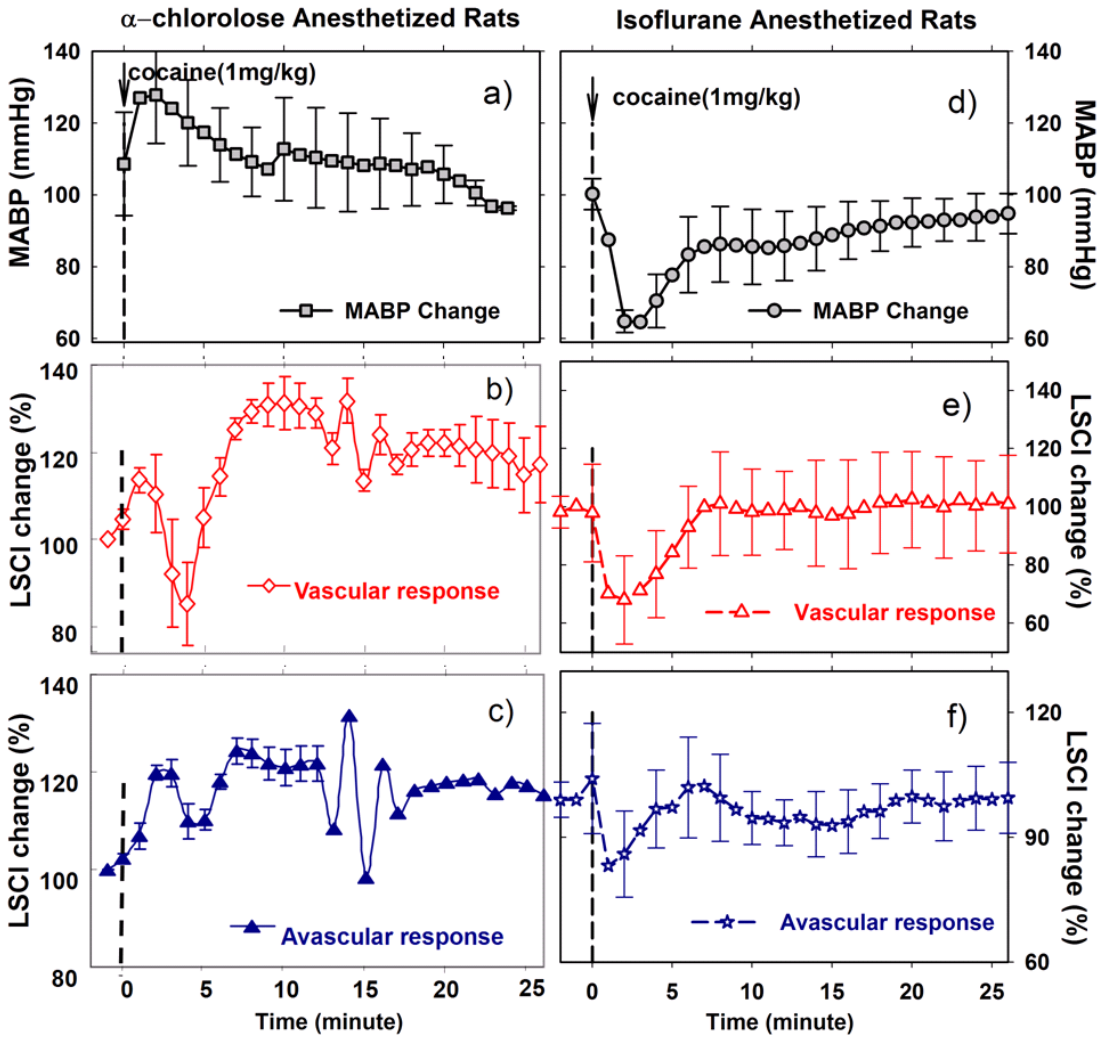


Fig.5-6 Cocaine-induced MABP (a and d) and relative changes of cortical CBF in both vascular (b and e) and avascular region(c and f) with time averaged for rats under α-chloralose anesthesia (left panel) and isoflurane anesthesia (right panel).

## 5.4 Discussions and Conclusion

In this study, we applied a new technique, which combines LSCI with SDOCT, to quantitatively characterize the spatiotemporal changes of cortical CBF in response to systemic cocaine administration in rat. Compared with other neuroimaging modalities, e.g., fMRI, PET, SPECT, this technique offers enhanced spatiotemporal resolutions (~32μm, ~100fps) and is suitable for characterizing cocaine-induced CBF changes in both vascular and avascular area. Two major findings of this study can be summarized as 1) acute cocaine challenge (1mg/kg) induced significant cortical local CBF changes, and 2) anesthetic regime modified the hemodynamic responses to cocaine.

Animal studies in sheep and pigs using a variety of CBF measures and anesthetics have shown different cerebrovascular responses to cocaine: 1) increased CBF and hypertension [Iida, 1994; Gleason, 1995]; 2) decreased CBF and hypotension [Anday, 1993; Yonetani, 1994; Stankovic, 1998]; or 3) no change at all [Albuquerque, 1995]. fMRI studies in rat brain have also shown variable blood oxygen level dependent (BOLD) responses to cocaine under different anesthetic regimes. For example, rats anesthetized with 0.7% halothane - a potent vasodilator to increase basal CBF 3-folds - exhibited widespread increases in regional CBV and BOLD after 1mg/kg cocaine injection [Marota, 2000]. In another study, rats anesthetized with urethane (1.2g/kg) - known to have minimal effect on basal CBF - exhibited widespread and dose-depended early decreases and later increases in the BOLD signals following cocaine challenge [Luo, 2003]. Recently, rats administrated with isoflurane and intravenous cocaine (1mg/kg) were found to present a negative BOLD signal in the immediate cortical surface [Schmidt, 2006]; which were in agreement with our findings using the optical spectroscopy that demonstrated the decreases in the cerebral blood volume and tissue oxygenation in isoflurane-anesthetized rat brains [Du, 2006]. Those results are also closely relevant to the presented results here as LSCI recorded mostly from superficial cortical CBFs (e.g., within 1mm below the cortical surface).

Here we demonstrated that, along the vasculature, cocaine evoked increase in CBF for rats anesthetized with α-chloralose (Fig.5-6 (b)) but decreases for those with isoflurane (Fig.5-6 (e)). The MABP exhibited the same patterns in response to cocaine challenge (Fig.5-6 (a, d)) and both MABP and CBF changes lasted 8-10 minutes, suggesting their coupling effects in the process. Our results in isoflurane anesthetized rats were in agreement with the negative BOLD responses to cocaine [Schmidt, 2006]. The CBF responses in α-chloralose anesthetized rats agreed with our previous findings using optical spectroscopy [Du, 2005; Du, 2006] and fMRI (positive BOLD responses) in urethane anesthetized animals [Luo, 2003]. The accentuation of cocaine-induced vasoconstriction effects in vasodilator (such as isoflurane and halothane) anesthtized rats could explain the results of previously reported negative BOLD response and decreased CBF after cocaine administration [Gollub, 1998]. On the other hand, as α-chloralose has minimal influence on the autonomic functions of brain and neurovascular coupling [Bonvento, 1994], cocaine-induced CBF changes in α-chloralose anesthetized rats were more likely to truly reflect the neurometabolic changes induced by cocaine.

In conclusion, we presented a dual-modality optical imaging technique which combins LSCI and SDOCT to enable quantitative characterization of cortical cerebral blood flow changes in small animals continuously and at high spatiotemporal resolutions. To examine the utility of this new technique for functional neuroimaging studies, we compared the cocaine-induced cortical CBF changes in rats anesthetized with α-chloralose and isoflurane. The results indicated that this technique was able to provide sufficient sensitivity and spatiotemporal resolutions to track subtle pharmadynamic changes, in particular cocaine-induced local CBF perfusions in superficial brain cortex. The observed cocaine-induced cortical CBF changes are in agreement with those reported previously using fMRI and other optical techniques, thus demonstrate the ability of this technique to quantify brain functional changes under cocaine challenge.

## 5.5 List of References


5-1) Albuquerque ML, Monito CL, Shaw L, Anday EK. Ethanol, morphine and barbiturate alter the hemodynamic and cerebral response to cocaine in newborn pigs. Biol. Neonate. 1995, 67: 432.

5-2) Anday EK, Lien R, Goplerud JM, Kurth DC, Shaw LM. Pharmacokinetics and effect of cocaine on cerebral blood flow in the newborn. Dev. Pharmacol. Ther. 1993, 20: 35.

5-3) Bardo MT. Neuropharmacological mechanisms of drug reward: beyond dopamine in the nucleus accumbens. Crit. Rev. Neurobiol. 1998, 12: 37.

5-4) Bonvento G, Charbonné R, Corrèze JL, Borredon J, Seylaz J, Lacombe P. Is alpha-chloralose plus halothane induction a suitable anesthetic regimen for cerebrovascular research? Brain Res. 1994, 665: 213.

5-5) Briers JD, Webster S. Laser speckle contrast analysis (LASCA): a nonscanning, full-field technique for monitoring capillary blood flow. J. Biomed. Opt. 1996, 1, 174.

5-6) Briers JD. Laser Doppler, speckle and related techniques for blood perfusion mapping and imaging. Physiol. Meas. 2001, R35.

5-7) Brust JC. Vasculitis owing to substance abuse. Neurol. Clin. 1997, 15: 945.

5-8) Buttner A, Mall G, Penning R, Sachs H. Theneuropathology of cocaine abuse. Leg. Med. (Tokyo) 2003, 5: S240.

5-9) Du C, Koretsky AP, Izrailtyan I, Benveniste H. Simultaneous detection of blood volume, oxygenation, and intracellular calcium changes during cerebral ischemia and reperfusion in vivo using diffuse reflectance and fluorescence. J. Cereb. Blood Flow Metab. 2005, 25: 1078.

5-10) Du C, Yu M, Volkow ND, Koretsky AP, Fowler JS, Benveniste H. Cocaine increases intracellular concentration of calcium in brain independently of its cerebrovascular effects. J. Neurosci. 2006, 26: 11522.

5-11) Dunn A, Devor A, Dale AM, Boas DA. Spatial extent of oxygen metabolism and hemodynamic changes during functional activation of the rat somatosensory cortex. Neuro-Image. 2005, 27: 279.

5-12) Durduran T, Burnett M, Yu G, Zhou C, Furuya D, Yodh A, Detre J, Greenberg J. Spatiotemporal quantification of cerebral blood flow during functional activation in rat somatosensory cortex using laser-speckle flowmetry. J. Cereb. Blood Flow Metab. 2004, 24: 518.

5-13) Gleason CA, Traystman RJ. Cerebral responses to maternal cocaine injection in immature fetal sheep. Pediatr. Res. 1995, 38: 943.

5-14) Gollub RL, Breiter HC, Kantor H, Kennedy D, Gastfriend D, Mathe RT, Makris N, Guimaraes A, Riorden J, Campbell T, Foley M, Hyman SE, Rosen B, Weisskoff R. Cocaine decreases cortical cerebral blood flow but does not obscure regional activation in functional magnetic resonance imaging in human subjects. J. Cereb. Blood Flow Metab. 1998, 18: 724.

5-15) Iida H, Gleason CA, O'Brien TP, Traystman RJ. Fetal response to acute fetal cocaine injection in sheep. Am. J. Physiol. 1994, 267: H1968.

5-16) Kaufman MJ, Levin JM, Maas LC, Rose SL, Lukas SE, Mendelson JH, Cohen BM, Renshaw PF. Cocaine decreases relative cerebral blood volume in humans: a dynamic susceptibility contrast magnetic resonance imaging study. Psychopharmacology. 1998, 138: 76.

5-17) Leitgeb R, Schmetterer L, Drexler W, Fercher A, Zawadzki R, Bajraszewski T. Real-time assessment of retinal blood flow with ultrafast acquisition by color DopplerFourier domain optical coherence tomography. Opt. Express. 2003, 11: 3116.
5-18) Lenz C, Frietsch T, Futterer C, Rebel A, van Ackern K, Kuschinsky W, Waschke KF. Local coupling of cerebral blood flow to cerebral gluocose metabolism during inhalational anesthesia in rats: desflurane versus isoflurane. Anesthesiology. 1999, 91:1720.
5-19) London ED, Cascella NG, Wong DF, Phillips RL, Dannals RF, Links JM, Herning R, Grayson R, Jaffe JH, Wagner Jr HN. Cocaine-induced reduction of glucose utilization in the human brain: a study using positron emission tomography and [fluorine18]-fluorodeoxyglucose. Arch. Gen. Psychiatry, 1990, 47: 567.
5-20) Luo F, Wu G, Li Z, Li SJ. Characterization of effects of mean arterial blood pressure induced by cocaine and cocaine methiodide on BOLD signals in rat brain. Magn. Reson. Med. 2003, 49: 264.
5-21) Luo Z, Wang Z, Yuan Z, Du C, Pan Y. Optical coherence Doppler tomography quantifies laser speckle contrast imaging for blood flow imaging in the rat cerebral cortex. Opt. Lett. 2008, 33: 1156.
5-22) Maekawa T, Tommasino C, Shapiro HM, Keifer-Goodman J, Kohlenberger RW. Local cerebral blood flow and glucose utilization during isoflurane anesthesia in the rat. Anesthesiology. 1986, 65: 144.
5-23) Marota JJ, Mandeville JB, Weisskoff RM, Moskowitz MA, Rosen BR, Kosofsky BE. Cocaine activation discriminates dopaminergic projections by temporal response: an fMRI study in rat. NeuroImage. 2000, 11: 13.
5-24) Martinez NE, Diez-Tejedor E, Frank A. Vasospasm/thrombus in cerebral ischemia related to cocaine abuse. Stroke. 1996, 27: 147.
5-25) Masamoto K, Kim T, Fukuda M, Wang P, Kim SG. Relationship between neural, vascular and BOLD signals in isoflurane-anesthetized rat somatosensory cortex. Cereb. Cortex. 2007, 17: 942.
5-26) Pearlson GD, Jeffery PJ, Harris GJ, Ross CA, Fischman MW, Camargo EE. Correlation of acute cocaineinduced changes in local cerebral blood flow with subjective effects. Am. J. Psychiatry. 1993, 150: 495.
5-27) Schmidt KF, Febo M, Shen Q, Luo F, Sicard KM, Ferris CF, Stein EA, Duong TQ. Hemodynamic and metabolic changes induced by cocaine in anesthetized rat observed with multimodal functional MRI. Psychopharmacology. 2006, 185: 479.
5-28) Stankovic MR, Fujii A, Maulik D, Kirby D, Stubblefield PG. Optical brain monitoring of the cerebrovascular effects induced by acute cocaine exposure in neonatal pigs. J. Maternal–Fetal Investig. 1998, 8: 108.
5-29) Wallace EA, Wisniewski G, Zubal G, Vandyck CH, Pfau SE, Smith EO, Rosen MI, Sullivan MC, Woods SW, Kosten TR. Acute cocaine effects on absolute cerebral blood flow. Psychopharmacology. 1996, 128: 17.
5-30) Wang R, Jacques S, Ma Z, Hurst S, Hanson S, Gruber A. Three dimensional optical angiography. Opt. Express. 2007, 15: 4083.
5-31) Yonetani M, Lajevardi N, Pastuszko A. Delivoria-Papadopoulos M, Dopamine, blood flow and oxygen pressure in brain of newborn piglets. Biochem. Med. Metabol. Biol. 1994, 51: 91.

# Chapter 6. Simultaneous Imaging of Cortical Hemodynamics and Blood Oxygenation Change during Cerebral Ischemia Using Dual-Wavelength Laser Speckle Contrast Imaging

## 6.1 Introduction

Characterization of cerebral hemodynamic and oxygen metabolic changes is of great importance to the study of brain functions and the relevant neurovascular disorders. Compared with other functional imaging modalities, e.g., fMRI and PET/SPECT, optical imaging techniques have the potential for high spatiotemporal resolutions and differentiation of the changes in blood flow, blood volume, and hemoglobin oxygenation by utilizing a wide variety of optical effects, including Doppler effect, absorption, scattering, and photon-acoustic effects [Dunn, 2003; Zhang, 2007; Du, 2005]. More importantly, simultaneous imaging of these parameters will immensely enhance our understanding of the hemodynamic processes that underlie neural activities and brain functions [Dunn, 2003; Du, 2005; Jones, 2001]. In this chapter, we report a dualwavelength laser speckle contrast imaging (DW-LSCI) technique that integrates laser Doppler flowmetry and near-IR oxymetry, and present experimental results for simultaneous imaging of blood flow, volume, and hemoglobin oxygenation changes induced by cortical transient-ischemia of rat brain.

## 6.2 Methods and Materials

Fig. 6-1 illustrates the DW-LSCI system that was illuminated by two single-mode laser diodes at the wavelengths of 785 nm (25 mW) and 830 nm (30 mW). As these two wavelengths were close and symmetrical to the isobestic point of the hemoglobin absorbance at 805 nm [Takatani,1987], their path-length difference was insignificant (<6%), and the resultant complications for hemoglobin oxygenation measurement could be neglected. The laser irradiances were collimated to ~ϕ5 mm and modulated by an optical chopper that passed these two beams alternatively at a constant speed (e.g., 2 Hz in this study). The two laser beams were then combined in the beam splitter to collinearly illuminate onto the cranial window surgically created on a rat cortical surface at 30°. The diffusely reflected light from rat cortex was relayed by a 1× macro lens (Nikon, f /105 mm, f#/ 2.8) to a cooled 12-bit monochromatic CCD camera (Retiga-Ex, pixel size: 6.45 μm) to be captured at an exposure time of $T$=10 ms, which had been optimized to render high contrast and sufficient dynamic range for speckle flow imaging [Dunn, 2003; Luo, 2008; Briers 1996]. Imaging acquisition was synchronized with the optical chopper to trigger the camera exposure interlaced between the two wavelengths. The captured image sequence was streamed into a computer via an IEEE-1394 interface for postimage processing to extract flow index distribution.

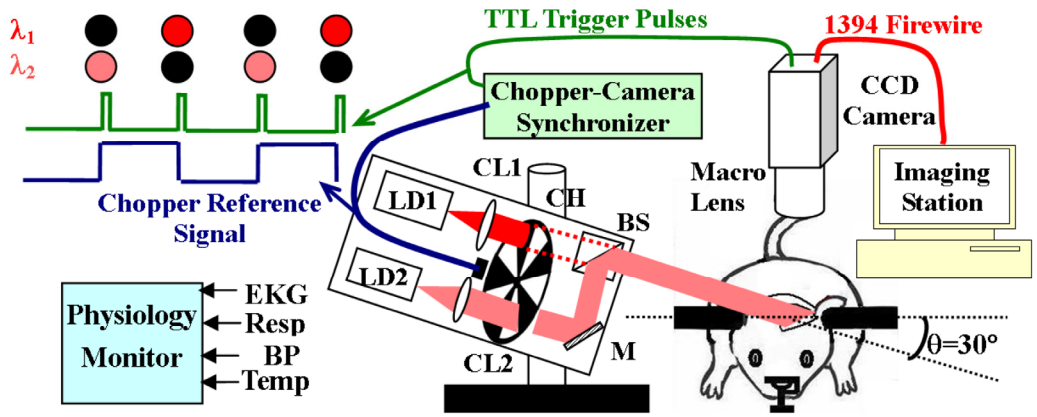


Fig. 6-1 Sketch illustrating the DW-LSCI setup. LD1, LD2: laser diodes at $\lambda_1$=785nm, $\lambda_2$=830nm; CL: collimator (f=20mm); BS: beam splitter; M: mirror, CH: chopper

To extract the flow contrast from a raw reflectance image embedded in speckle patterns, 5×5 binning was performed to compute the speckle contrast map $K=\sigma/\langle I\rangle$, where $\langle I\rangle$ and $\sigma$ were the mean intensity and the standard deviation of each binning window (i.e., 6.45×5≈32μm), respectively. The relationship between $K$ and the dynamic features of the speckles is highly complex and has been approximately derived as [Bandyopadhyay, 2005]

$$K=\left\{\frac{\tau_C}{T}+\frac{\tau_c^2}{2T^2}\left[exp\left(-\frac{2T}{\tau_C}\right)-1\right]\right\}^{1/2} \tag{6-1}$$

where $\tau_C=[ka\langle v^2\rangle^{1/2}]^{-1}$ is the autocorrelation time of the speckle intensity fluctuation, $k=2\pi/\lambda$ is the wave number of light, and $\langle v^2\rangle^{1/2}$ represents the rms speed of the scattering particles [Briers 1996]. As $a$ is an unknown factor associated with $v$ distribution and tissue scattering characteristics, the combined quantity $a\langle v^2\rangle^{1/2}$ is defined as the speed index, which was obtained from a precalculated look-up table between $K$ and $a\langle v^2\rangle^{1/2}$ to minimize computation.

Blood volume and oxygenation changes can be derived from the dual-wavelength images under the assumption that the concentration changes of the oxygenated hemoglobin $\Delta[HbO_2]$ and deoxygenated hemoglobin $\Delta[HbR]$ dominate the dynamic changes of light absorption and thus the measured diffuse reflectance [1-4], which can be expressed by

$$\begin{bmatrix}\Delta[HbO_2(t)]\\ \Delta[HbR(t)]\end{bmatrix}=\begin{bmatrix}\varepsilon_{HbO_2}^{\lambda_1} & \varepsilon_{HbR}^{\lambda_1}\\ \varepsilon_{HbO_2}^{\lambda_2} & \varepsilon_{HbR}^{\lambda_2}\end{bmatrix}^{-1}\cdot\begin{bmatrix}\dfrac{\ln\left(R_{\lambda_1}(0)/R_{\lambda_1}(t)\right)}{L_{\lambda_1}(t)}\\ \dfrac{\ln\left(R_{\lambda_2}(0)/R_{\lambda_2}(t)\right)}{L_{\lambda_2}(t)}\end{bmatrix} \tag{6-2}$$

where $\varepsilon$ refers to the molar spectral absorbance coefficient of the chromophore, $R_{\lambda 1}(t)$, $R_{\lambda 2}(t)$ are the measured diffuse reflectances (averaged over 5 consecutive frames to

reduce speckle noise) at these two wavelengths at time point $t$, and $R_{\lambda 1}(0)$, $R_{\lambda 2}(0)$ are their baseline values prior to ischemia. $L_{\lambda 1}(t) \approx L_{\lambda 2}(t)$ where $L_{\lambda 1}(t)$, $L_{\lambda 2}(t)$ are their pathlengths. The concentration change of the total hemoglobin can be obtained by $\Delta[HbT]=\Delta[HbO_2]+\Delta[HbR]$ and is assumed to be linearly proportional to local blood volume [Dunn, 2003; Du, 2005; Jones, 2001]. Based on Eq.(1) and Eq.(2), the changes in the cerebral blood flow, blood volume and hemoglobin oxygenation within the cortical window can be simultaneously imaged at high resolutions using the DW-LSCI system.

To examine the utility of this technique for simultaneous imaging, we performed animal study in 4 female Sprague-Dawley rats (250-300g/each). For surgical preparation, the rat was anesthetized and ventilated with 2% isflurane mixed in oxygen. The right carotid artery was cannulated for continuous arterial blood pressure monitoring and the left carotid artery was isolated by a 3.0 suture. The rat was then positioned on a stereotaxic frame, and a 4×5mm$^2$ craniotomy was created above the sensory-motor cortex. The isoflurane level was then reduced to 1% during imaging. Transient forebrain ischemia was induced for 5 minutes by concurrently occluding the left carotid artery and rapidly withdrawing 3-5ml of blood from the right carotid cannula. During ischemia, the mean arterial blood pressure was maintained at 35-43mmHg. At the end of the ischemic insult, reperfusion was achieved by releasing the carotid occlusion and carefully infusing the extracted blood in 60s to avoid sudden overshoot of cerebral blood flow and volume and the potential reperfusion damage to the brain. During the experiment, the physiological parameters, e.g., peripheral pulse, intra-arterial pressure, ECG, and body temperature were continuously monitored.

### 6.3 Results

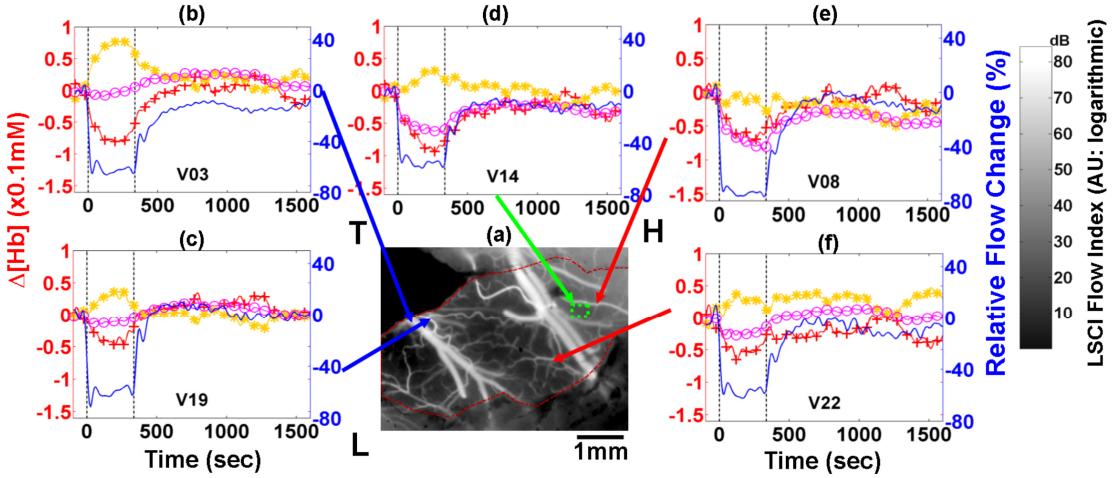


Fig.6-2 (a) Snap shot of DW-LSCI flow image of rat cortex. The dashed red circle shows the cranial window region for quantitative analysis. H, T, L: head, tail and lateral directions. Panels (b-f): traces of relative cerebral blood flow changes (solid curves) and $\Delta[HbO_2]$ (crosses), $\Delta[HbR]$(asterisks), $\Delta[HbT]$ (circles) in the selected (b)large ($\phi$220μm) and (c)small ($\phi$65μm) venous, (e,f) arterial ($\phi$50μm, $\phi$38μm) and (d) perfused tissue regions as pointed by arrows. The two dashed vertical lines indicate the onset of ischemia (t=0s) and reperfusion (t=336s)

periods. Right y-axises (red): Δ[Hb] (x0.1mM); left y-axis (blue): relative flow changes (%).

Fig.6-2 shows the typical changes of rat brain in response to ischemic insult and reperfusion. At the onset of ischemia (t=0s) a rapid decrease was induced in both cortical vascular flow (63±7%) and tissue perfusion (47±8%) as shown by the solid curves. Meanwhile, [$HbO_2$] (crosses) decreased gradually in all regions, whereas [HbR] (asterisks) increased significantly in venous flow [Figs.6-2(b) and 2(c)] and perfused tissue [Fig. 6-2(d)] but remained unchanged or slighted changed in arteriolar flows [Figs. 6-2(e) and (f)]. These results were consistent with previous physiological studies in that deprivation of cerebral blood and hence oxygen supply during forebrain ischemia resulted in an increase of oxygen extraction from capillaries and thus accelerated accumulation of [HbR] in the downstream regimes (i.e., venous flow and perfused tissue), while [HbR] in the upstream arterial regimes remained unaffected [Du, 2005]. The result further indicated that even in the downstream regimes, the magnitude of Δ[$HbO_2$] was greater than that of Δ[HbR] but in opposite directions. As a result, Δ[HbT] (circles) exhibited a gradual negative change similar to Δ[$HbO_2$] but at a substantially reduced magnitude in the entire cortical area during ischemia. At the onset of reperfusion (*t*=336 s) after ischemia, the blood flow increased rapidly first, followed by a slow recovery toward the baseline over a 10 min duration. Meanwhile, [HbT], [$HbO_2$], and [HbR] all followed a gradual recovery toward their baselines within the perturbed regions.

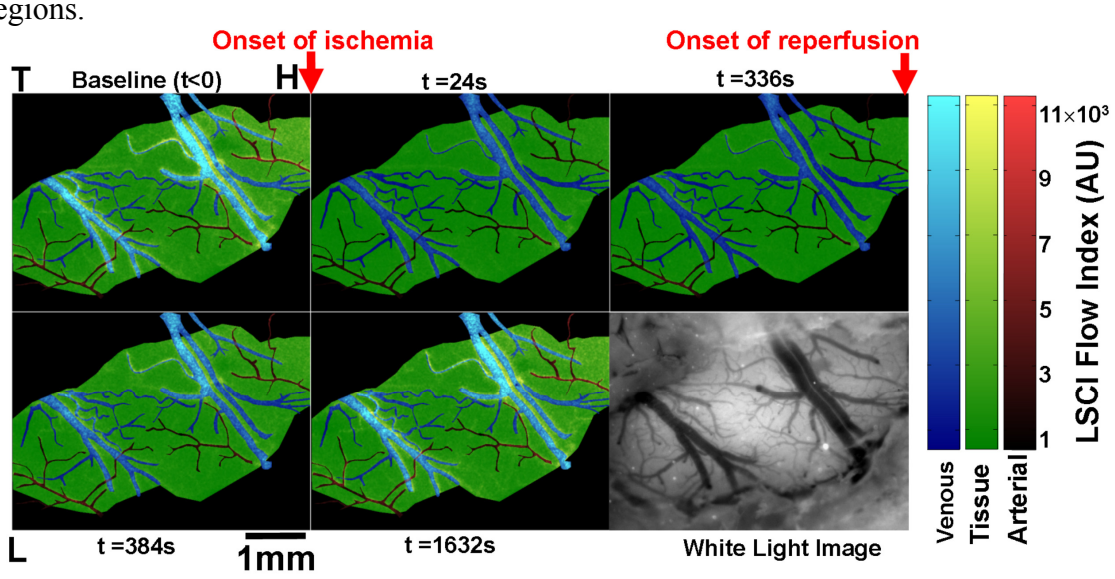


Fig.6-3: Time-lapse DW-LSCI flow images of rat cortex undergoing cerebral ischemia (t=0~336s) and reperfusion. Image size: 3.7×5.1 $mm^2$. Arterial and venous flow rates and tissue perfusion rate were color coded in red, blue and green, respectively. The black shadow is the region out of the cranial window. Detailed time-course changes were shown in Fig.6-2.

Taking advantage of the distinct difference in the metabolic transients between arterial and venous flows in response to ischemia as shown in Fig.6-2, Δ[HbR] can be used to differentiate these two types of vessels [Zhang, 2007], which is in fact critical to many hemodynamic studies. To do this, all sizeable vessels ($\phi$>30μm) were first segmented from the adjacent tissue (including irresolvable capillary beds) owing to the high flow contrast provided by the LSCI images. Then, the segmented flow mask was overlapped on the Δ[HbR($x$, $y$, $t$)] mapping to perform 2-stage 1-tail t-tests between 1) ischemia (i.e. 0~336s in Fig.6-2) and pre-baseline (e.g., -96~0s) and 2) between ischemia (e.g. 0~336s) and post-baseline (e.g., 500~600s) for each segmented vessel, i.e.,

$$t_{1|2} = \frac{< R_i > - < R_b >}{\left[ \frac{(n_i - 1)\sigma_i^2 + (n_b - 1)\sigma_b^2}{n_i n_b (n_i + n_b - 2)/(n_i + n_b)} \right]^{1/2}} \quad (3)$$

where $<R_{i/b}>$, $\sigma_{i/b}$, and $n_{i/b}$ are the mean, standard deviation and the time points of the sampled Δ[HbR] within a segmented vessel during ischemic ($i$) and baseline ($b$) periods. For venous and arterial flow classification, vessels with both $t_1$- and $t_2$-values >1.75 (threshold for significance p=0.05) were considered to be venous flows; otherwise, they were arterial flows. The results tend to be confirmed by the orientations of vessel fortifications, i.e., arterial stems branch towards midline whereas venous stems branch towards the lateral side [Hebel, 1986]. With the flow types differentiated, Fig. 6-3 shows the typical flow changes during ischemia and reperfusion in which arterial, venous and perfusion flows were linearly color coded in red, blue and green respectively. The detailed time courses for blood flow, blood volume and oxygenation changes in several regions were presented in Fig.6-2.

### 6.4 Summary

In summary, we presented a new dual-wavelength LSCI technique. Compared with other simultaneous imaging methods [Zhang, 2007], this technique is compact, low cost and easy for clinical adoption. Preliminary animal results demonstrated the efficacy of this simple technique for simultaneous full-field imaging of both cerebral blood flow and hemoglobin oxygenation and blood volume changes following rat cerebral ischemia and reperfusion, thus allowing us to distinguish arterial and venous branches within cerebral vessel network based on the detected [HbR] transient differences. Additional advantage of DW-LSCI included enhanced flow contrast because the residual speckles noise at the two wavelengths were incoherent and thus effectively reduced. Noteworthily, the hemoglobin oxygenation characterizations can be further improved by correcting the ischemia-induced pathlength changes in Eq.(2), which could be 25-35%. Further work will include applying the technique to analyze the complex hemodynamic and neuronal responses to functional brain activations and drug paradigms.

### 6.5 List of References

6-1) Bandyopadhyay R, Gittings AS, Suh SS, Dixon PK, Durian DJ. Speckle-visibility spectroscopy: A tool to study time-varying dynamics. Rev Sci Instru. 2005, 76:093110.
6-2) Briers JD, Webster S. Laser speckle contrast analysis (LASCA): A nonscanning, full-field technique for monitoring capillary blood flow. J. Biomed. Opt. 1996, 1: 174.

6-3) Du C, Koretsky AP, Izrailtyan I and Benveniste H. Simultaneous detection of blood volume, oxygenation, and intracellular calcium changes during cerebral ischemia and reperfusion in vivo using diffuse reflectance and fluorescence. J Cereb Blood Flow Metab. 2005, 25: 1078.
6-4) Dunn AK, Devor A, Bolay H, Andermann ML, Moskowitz MA, Dale AM, Boas D A. Simultaneous imaging of total cerebral hemoglobin concentration, oxygenation, and blood flow during functional activation. Opt Lett. 2003, 28:28.
6-5) Hebel R, Stromberg MW. Anatomy and Embryology of the Laboratory Rat. Biomed Verlag. 1986.
6-6) Jones M, Berwick J, Johnston D, Mayhew J. Concurrent optical imaging spectroscopy and laser-Doppler flowmetry: The relationship between blood flow, oxygenation, and volume in rodent barrel cortex. NeuroImage. 2001, 13(6): 1002.
6-7) Luo Z, Wang Z, Yuan Z, Du C, Pan Y. Optical coherence Doppler tomography quantifies laser speckle contrast imaging for blood flow imaging in the rat cerebral cortex. Opt Lett. 2008, 33(10): 1156.
6-8) Takatani S, Graham MD. Theoretical analysis of diffuse reflectance from a two-layer tissue model,IEEE Trans. Biomed. Eng. 1987, 26: 656.
6-9) Zhang HF, Maslov K, Sivaramakrishnan M, Stoica G, Wang LH. Imaging of hemoglobin oxygen saturation variations in single vessels in vivo using photoacoustic microscopy. Appl Phys Lett. 2007, 90(5): 053901.

# Summary

**Outline**

In my thesis, first, a review was given about the physiological scenarios and mechanisms behind the neuronal-metabolic-vascular coupling during brain activation and how they exhibit contrast in different functional measurements. Following the introdution, a set of biophysical models, which was created by Buxton and his coworkers, was introduced and fully discussed. The qualitative and quantitative descriptions in this chapter served as the theoretical guidance throughout this thesis for experimental studies using various techniques in Chapter 2, 3, 5 as well as for the improvement of LSCI system pursued in Chapter 4 and 6.

Chapter 2 described the animal protocol for performing electrical somatosensory stimulation and the optimal conditions for obtaining cortex responses. Then it presented an electrophysiological and three optical methods for detecting electrical stimulus evoked FP, CBF, CBV and oxygenation changes in somatosensory cortex. Especially, the impressive versatility of ODF and the imaging power of LSCI inspired the work in Chapter 6 to integrate dual-wavelength oximetry into flow mapping. All the results were in good agreement with the modeling in Chapter 1 and repeatedly validated our animal protocol for in-vivo brain function measurements.

As optical measurements described here can only track the cortical responses within less than 1mm depth, the desire to study activations in other brain areas led us to use BOLD based fMRI technique in Chapter 3. In this particular study, BOLD-fMRI was used to assess systemic lidocaine's analgesic effect on brain activations in response to innocuous and nociceptive electrical stimulation. As demonstrated by the results, therapeutic *iv* lidocaine doesn't have evident suppression to the stimulated BOLD response in either non-noxious or nociceptive pathway in the brain. Quite the contrary, it even enhances the BOLD response in the cortex.

Our in-house built LSCI system has shown its advantages in Chapter 2, such as high spatiotemporal resolution, the effectiveness of full field flow mapping by a single exposure. However, the fact that LSCI can only measure relative flow speed change has become a major obstacle to its promotion for more serious applications. In Chapter 4, LSCI was combined with SDOCT, which can render cross sectional mapping of absolute flow speed at high spatial resolution, in an attempt to circumvent the obstacle and to quantify the relative flow measurement of LSCI. Several features built into the combined system facilitated the simultaneous imaging and co-registration of the two modaility, thus pernitted in field calbartion of LSCI. The speed calibration using least square linear fitting achieved high correlation, which demonstrated the LSCI's potential to be used in quantitative assessment of cerebral blood flow change.

In Chapter 5, the quantified LSCI was further used to characterize spatial and temporal CBF response to acute cocaine in rat's brain cortex under α-chloralose and isoflurane anesthesia regimes. The results revealed two distinctive patterns: under α-chloralose anesthesia, following iv cocaine injection, CBFs in both vascular and perfused tissue regions rise to an elevated plateau after a transient fluctuation; while under

isoflurane anesthesia, following iv cocaine injection, CBFs in both vascular and perfused tissue regions undergo a brief decrease before returning to the basal level, which reflect isoflurane's effect of causing vessel dilation and suppressing neuron activity. This is a pioneering work to use LSCI to track CBF changes in response to cocaine at high spatiotemporal resolution, and again demonstrated LSCI's potential as a quantitative flow imaging tool.

The ideal of simultaneous imaging of hemodynamic and blood oxygenation change in brain tissue motivated the development of dual-wavelength LSCI system in Chapter 6. DW-LSCI is a unique approach that can simultaneously image full field cortical changes of CBF, CBV and hemoglobin oxygenation. The distinctive oxygenation changes in arterial, venous and perfused tissue compartments allow the arterial andvenous compartments to be discriminated based on a transient cerebral ischemia model.

**Future Works**

In the future, beside hemodynamic and blood oxygenation mapping, LSCI will be further extended to accommodate simultaneous fluorescent imaging, for instance, for detecting $[Ca^{2+}]_i$ change in brain cortex. In case of using the non-ratiorized $[Ca^{2+}]_i$ labeling dye Rhod(AM), a green beam will be needed for excitation, a long pass filter in front of CCD will be needed for selectively passing fluorescent light, and a yellow beam with a wavelength close to the fluorescent emission peak will be needed for correcting the absorbance change for a more accurate quanfication of $[Ca^{2+}]_i$. In addition, for the alternative delivery of multiple wavelengths, which is beyond the capability of mechanic chopping, a programable electronic switching system and optic fiber based light delivery must be designed for the new system. In the preliminary study, we simply replaced one NIR laser in the DW-LSCI system with a green laser and inserted a long pass filter into the camera. It was observed that fluorescence emission increased accompanying decreased CBF during ischemia as well as accompanying increased CBF following iv cocaine injection in α-chloralose anesthetized rats, which both agreed with the previous measurements using our ODF technique. The inherent advantages and our recent improvement of LSCI also encourage my attempts to adapt LSCI into other clinical optical imaging platforms, such as surgical microscope, endoscope and ophthalmoscope.

Cocaine' effect on brain activation in naive and cocaine-addicted animal is also an interesting question that needs to be answered. In a recent study, we used fMRI to assess brain activation in response to forepaw stimuations before and after a single dose (1mg/kg) of iv cocaine injection, somehow similar to the paradigm we used in chapter 3 for studying lidocaine's effect. In both naive and cocaine-addicted rats, enhancement of BOLD response by acute cocaine was observed in contralateral somatosernsory cortex. The difference was that, in order to get significant baseline BOLD response in the cocaine naive rats, the animal protocol described in Chapter 2 should be followed to maintain the rat in normocapnia ($PCO_2$=35-41mmHg), while, to get the alike significant baseline response in the cocaine addicted rats (20mg/kg *ip* cocaine per day for 14 days), those rats have to be kept in slightly hypercapnic condition ($PCO_2$=44-47mmHg). More careful analyses of the activation patterns and the blood gas measurements are needed to assess the enhancement effect and to explain the difference induced by chronic cocaine treatments.

# List of References


**Chapter 1**

1-1) Ames III A. CNS energy metabolism as related to function. Brain Res. Rev. 2000, 34: 42.

1-2) Bronzino JD. The Biomedical Engineering Handbook, Second Edition ed. Boca Raton, FL: CRC Press LLC. 2000.

1-3) Boynton GM, Engel SA, Glover GH, Heeger DJ. Linear systems analysis of functional magnetic resonance imaging in human V1. J. Neurosci. 1996, 16: 4207–21.

1-4) Buxton RB, Frank LR. A model for the coupling between cerebral blood flow and oxygen metabolism during neural stimulation. J. Cereb. Blood Flow Metab. 1997, 17: 64.

1-5) Buxton RB, Uludag K, Dubowitz DJ, Liu TT. Modeling the hemodynamic response to brain activation. NeuroImage, 2004, 23: S220.

1-6) Davis TL, Kwong KK, Weisskoff RM, Rosen BR. Calibrated functional MRI: mapping the dynamics of oxidative metabolism. Proc. Natl. Acad. Sci. U. S. A. 1998, 95: 1834.

1-7) Devor A, Dunn AK et al.. Coupling of total hemoglobin concentration, oxygenation, and neural activity in rat somatosensory cortex. Neuron, 2003, 39-2: 353.

1-8) Dunn AK, Devor A et al., Simultaneous imaging of total cerebral hemoglobin concentration, oxygenation, and blood flow during functional activation. Opt Lett. 2003, 28: 28.

1-9) Dunn AK, Devor A, Dale AM, Boas DA. Spatial extent of oxygen metabolism and hemodynamic changes during fucntional activation of the rat somatosensory cortex. NeuroImage. 2005, 27: 279.

1-10) Durduran T and Yu G et al., Diffuse optical measurement of blood flow, blood oxygenation, and metabolism in a human brain during sensorimotor cortex activation. Opt. Lett. 2004, 29-14: 1766.

1-11) Faraci FM and Heistad DD. Regulation of the Cerebral Circulation: Role of Endothelium and Potassium Channels. Physiol. Rev. 1998, 78: 53.

1-12) Friston KJ, Mechelli A, Turner R, Price CJ. Nonlinear responses in fMRI: the Balloon model, Volterra kernels, and other hemodynamics. NeuroImage. 2000, 12: 466.

1-13) Grubb RL, Raichle ME, Eichling JO, Ter-Pogossian MM. The effects of changes in PaCO2 on cerebral blood volume, blood flow, and vascular mean transit time. Stroke. 1974, 5: 630.

1-14) Hoge RD and Atkinson J et al. Linear coupling between cerebral blood flow and oxygen consumption in activated human cortex. PNAS-USA. 1999, 96, 16: 9403.

1-15) Jones M and Berwick J et al., Concurrent optical imaging spectroscopy and laser-Doppler flowmetry: the relationship between blood flow, oxygenation, and volume in rodent barrel cortex. Neuroimage. 2001, 13: 1002.

1-16) Kandel et al. Principles of Neural Science. New York: McGraw Hill. 2000.

1-17) Kida I, Hyder F, Behar KL. Inhibition of voltage-dependent sodium channels suppresses the functional magnetic resonance imaging response to forepaw somatosensory activation in the rodent. J. Cereb. Blood Flow Metab. 2001, 21: 585.
1-18) Kneipp J, Balakrishnan G, Chen R, Shen TJ, Sahu SC, Ho NT, Giovannelli JL, Simplaceanu V, Ho C, Spiro TG. Dynamics of allostery in hemoglobin: roles of the penultimate tyrosine H bonds. J Mol Biol. 2006, 356(2): 335.
1-19) Lauritzen, M. Relationship of spikes, synaptic activity, and local changes of cerebral blood flow. J. Cereb. Blood Flow Metab. 2001, 21:1367.
1-20) Leybaert L. Neurobarrier coupling in the brain: a partner of neurovascular and neurometabolic coupling. J. Cereb. Blood Flow Metab. 2005, 25: 2.
1-21) Logothetis NK. The underpinnings of the BOLD functional magnetic resonance imaging signal. J. Neurosci. 2003, 23: 3963.
1-22) Magistretti PJ, Pellerin L. Cellular mechanisms of brain energy metabolism and their relevance to functional brain imaging. Philos. Trans R Soc Lond B Biol Sci. 1999, 354: 1155.
1-23) Malonek D, Grinvald A. Interactions between electrical activity and cortical microcirculation revealed by imaging spectroscopy: implications for functional brain mapping. Science. 1996, 272-5261: 551.
1-24) Mandeville JB, Marota JJA, Weisskoff RM et al. Evidence of a cerebrovascular post-arteriole Windkessel with delayed compliance. J. Cereb. Blood Flow Metab. 1999b, 19: 679.
1-25) Marieb EN. Human Anatomy & Physiology. Benjamin Cummings. 2003, 6 ed.
1-26) Mayhew J, Johnston D et al. Increased oxygen consumption following activation of brain: theoretical footnotes using spectroscopic data from barrel cortex. Neuroimage. 2001(13): 975.
1-27) Mintun MA, Lundstrom BN, Snyder AZ, Vlassenko AG, Shullman GL, Raichle ME. Blood flow and oxygen delivery to human brain during functional activity: Theoretical modeling and experimental data. PNAS. 2001, 98: 6859.
1-28) Ogawa S, Menon RS, Tank DW, Kim SG, Merkle H, Ellerman, JM, Ugurbil K. Functional brain mapping by blood oxygenation level-dependent contrast magnetic resonance imaging: a comparison of signal characteristics with a biophysical model. Biophys. J. 1993, 64: 803.
1-29) Raichle ME. Behind the scenes of functional brain imaging: A historical and physiological perspective. PNAS.1998, 95: 765.
1-30) Rengachary SS, Ellenbogen RG, editors, Principles of Neurosurgery, Edinburgh: Elsevier Mosby, 2005.
1-31) Takano T, Tian G, Nedergaard M et al, Astrocyte-mediated control of cerebral blood flow, Nat Neurosci. 2006, 9(2: 260.
1-32) Zonta M, Angulo MC, Gobbo S, Rosengarten B, Hossmann KA, Pozzan T, Carmignoto G, "Neuron-to-Astrocyte Signaling is Central to the Dynamic Control of Brain Microcirculation," Nat. Neurosci. 2003, 6: 43.

**Chapter 2**

2-1) Ances BM, Greenberg JH, Detre J. Laser Doppler imaging of activation-flow coupling in the rat somatosensory cortex. NeuroImage. 1999, 10): 716.

2-2) Austin VC, Blamire AM, Grieve SM, O'Neill MJ, Matthews PM, Sibson NR. Difference in the BOLD fMRI response to direct and indirect cortical stimulation in the rat. Magn Reson Med. 2003, 49: 838.
2-3) Barfod C, Akgoren N, Fabricius M, Dirnagl U, Lauritzen M. Laser-Doppler measurements of concentration and velocity of moving blood cells in rat cerebral circulation. Acta Physiol Scand. 1997, 160(2): 123.
2-4) Barnett NJ, Dougherty G, Pettinger SJ. Comparative study of two laser Doppler blood flowmeters. J Med Engin Tech. 1990, 11(6): 243.
2-5) Bonner R, Nossal R. Model for laser Doppler measurements of blood flow in tissue. Appli Optics. 1981, 20(12): 2097.
2-6) Bonner R, Nossal R. Principles of laser-Doppler flowmetry. In: Laser-Doppler blood flowmetry, Vol 107. Shepard Alber P and Öberg P Ake, editors. Boston: Kluwer Academic Publishers. 1990, 17.
2-7) Briers JD, Webster S. Laser speckle contrast analysis (LASCA): a nonscanning, full-field technique for monitoring capillary blood flow. J Biomed Opt. 1996, 1: 174.
2-8) Briers JD. Laser Doppler, speckle and related techniques for blood perfusion mapping and imaging. Physiol. Meas. 2001, 22: R35.
2-9) Chance B, Cohen P, Jobsis F, Schoener B. Intracellular oxidation-reduction state in vivo. Science 1962, 137: 499.
2-10) Chance B, Nioka S, Sadi S, Li C. Oxygenation and blood concentration changes in human subject prefrontal activation by anagram solutions. Adv Exp Med Biol. 2003, 510: 397.
2-11) Chapin JK, Lin CS. Mapping the body representation in the SI cortex of anesthetized and awake rats. J Comp Neurol. 1984, 229: 199.
2-12) Coq JO, Xerri C. Environmental enrichment alters organizational features of the forepaw representation in the primary somatosensory cortex of adult rats. Exp Brain Res. 1998, 121: 191.
2-13) Culver JP, Durduran T, Furuya D, Cheung C, Greenberg JH, Yodh AG. Diffuse optical tomography of cerebral blood flow, oxygenation, and metabolism in rat during focal ischemia. J Cereb Blood Flow Metab. 2003, 23(8): 911.
2-14) Du C, MacGowan GA, Farkas DL, Koretsky AP. Calcium measurements in perfused mouse heart: quantitating fluorescence and absorbance of Rhod-2 by application of photon migration theory. Biophys J 2001,80(1): 549.
2-15) Du C, Koretsky AP, Izrailtyan I, Benveniste H. Simultaneous detection of blood volume, oxygenation, and intracellular calcium changes during cerebral ischemia and reperfusion in vivo using diffuse reflectance and fluorescence. J Cereb Blood Flow Metab. 2005, 25: 1078.
2-16) Dunn AK, Bolay T, Moskowitz MA, Boas DA. Dynamic imaging of cerebral blood flow using laser speckle. J Cereb Blood Flow Metab. 2001, 21: 195.
2-17) Dunn A, Devor A, Bolay H et al. Simultaneous imaging of total cerebral hemoglobin concentration, oxygenation, and blood flow during functional activation. Opt. Lett. 2003, 28: 28.
2-18) Dunn A, Devor A, Dale AM, Boas DA. Spatial extent of oxygen metabolism and hemodynamic changes during functional activation of the rat somatosensory cortex. NeuroImage. 2005, 27: 279.

2-19) Duong TQ, Silva AC, Lee SP, Kim SG. Functional MRI of calcium-dependent synaptic activity: cross correlation with CBF and BOLD measurements. Magn Reson Med. 2000, 43: 383.
2-20) Durduran T, Burnett M, Yu G et al. Spatiotemporal Quantification of Cerebral Blood Flow During Functional Activation in Rat Somatosensory Cortex Using Laser-Speckle Flowmetry. J. Cereb. Blood Flow Metab. 2004, 24: 518.
2-21) Fabricius M, Akgoren N, Dirnagl U, Lauritzen M. Laminar analysis of cerebral blood flow in cortex of rats by laser-Doppler flowmetry: a pilot study. J Cereb Blood Flow Metab. 1997, 17(12): 1326.
2-22) Jones M, Berwick J, Johnston D, Mayhew J. Concurrent optical imaging spectroscopy and laser Doppler flowmetry: The inrelationship between blood flow, oxygenation, and volume in rodent barrel cortex. NeuroImage. 2001(13): 1002.
2-23) Kharlamov A, Brown BR, Easley KA, Jones SC. Heterogeneous changes in cerebral blood flow during hypotension demonstrated by laser speckle technique. J Cereb Blood Flow Metab Suppl. 2003, 23(S1): 84.
2-24) Kim S. Quantification of relative cerebral blood flow change by flow-sensitive alternating inversion recovery (FAIR) technique: application to functional mapping. Mag Res Med. 1995, 34: 293.
2-25) Kohl M, Lindauer U, Royl G, Kuhl M, Gold L, Villringer A, Dirnagl U. Physical model for the spectroscopic analysis of cortical intrinsic optical signals. Phys Med Biol. 2000, 45: 3749.
2-26) Kwong KK, Belliveau JW, Chesler DA, Goldberg IE, Weisskoff RM, Poncelet BP, Kennedy DN, Hoppel BE, Cohen MS, Turner R, Cheng HM, Brady T, Rosen B. Dynamic magnetic resonance imaging of human brain activity during primary sensory stimulation. Proc. Natl Acad Sci USA. 1992, 89: 5675.
2-27) Lindsburg PJ, O'Neil JT, Paakkari IA, Hallembeck JM, Feuerstein G. Validation of laser Doppler flowmetry in measurement of spinal cord blood flow. Am J Physiol. 1989, 257: H674.
2-28) Malonek D, Dirnagl U, Lindauer U, Yamada K, Kanno I, Grinvald A. Vascular Imprints of neural activity: Relationship between the dynamics of cortical blood flow, oxygenation, and volume changes following sensory stimulation. Proc Natl Acad Sci: Neurobiol. 1997, 94.: 14826.
2-29) Marieb EN. Human Anatomy & Physiology. Benjamin Cummings. 2003, 6 Ed.
2-30) Matsuura T, Fujita H, Seki C, Kashikura K, Yamada K, Kanno I. CBF change evoked by somatosensory activation measured by laser-Doppler flowmetry: independent evaluation of RBC velocity and RBC concentration. Jpn. J. Physiol. 1999, a(49): 289.
2-31) Matsuura T, Kanno I. Quantitative and temporal relationship between local cerebral blood flow and neuronal activation induced by somatosensory stimulation in rats. Neurosci Res. 2001, 40: 281.
2-32) National Nuclear Data Center, Brookhaven National Laboratory. Information extracted from the NuDat 2.1 database (retrieved Sept. 2005).
2-33) Navakatikyan M, Leonard BL, Evans RG, Malpas SC. Modelling the neural control of intrarenal blood flow. Clin Exper Pharm Physiol. 2000, 27: 650.
2-34) Nioka S, Luo Q, Chance B. Human brain functional imaging with reflectance CWS. Adv Exp Med Bio. 1997, 428: 237.

2-35) Offenhauser N, Thomsen K, Caesar K, Lauritzen M. Activity induced tissue oxygenation changes in rat cerebellar cortex: interplay of postsynaptic activation and blood flow. J. Physiol. 2005, 565(1): 279.
2-36) Paxinos G, Watson C. The rat brain in stereotaxic coordinates. Academic Press. 1982.
2-37) Phelps ME, Huang SC, Hoffman EJ, Selin C, Sokoloff L, Kuhl DE. Tomographic measurement of local cerebral glucose metabolic rate in humans with (F-18)2-fluoro-2-deoxy-D-glucose: validation of method. Ann Neurol. 1979, 6(5): 371.
2-38) Roy CS, Sherrington CS. On the regulation of the blood supply of the brain. J Physiol. 1890, 11: 85.
2-39) Silva AC, Koretsky AP. Laminar specificity of functional MRI onset times during somatosensory stimulation in rat. PNAS. 2002, 99 (23): 15182.
2-40) Skarphedinsson JO, Harding H, Thoren P. Repeated measurements of cerebral blood flow in rats. Comparison between the hydrogen clearance method and laser Dopplr flowmetry. Acta Physiol Scand. 1988, 134: 133.
2-41) Tenland T. On laser Doppler flowmetry: Methods and microvascular applications. Linkoping University Medical Dissertations, no. 136, Linkoping, Sweden, 1982.
2-42) Thomsen K, Offenhauser N, Lauritzen M. Principal neuron spiking: neither necessary nor sufficient for cerebral blood flow in rat cerebellum. J. Physiol. 2004, 560(1): 181.
2-43) Ureshi M, Matsuura T, Kanno I. Stimulus frequency dependence of the linear relationship between local cerebral blood flow and field potential evoked by activation of rat. NeuroSci Res. 2004, 48: 146.
2-44) Vongsavan N, Matthews B. Some aspects of the use of laser Doppler flow meters for recording tissue blood flow. Exp Physiol. 1993, 78: 1.
2-45) Xerri C , Bourgeon S, Coq JO. Perceptual context-dependent remodeling of the forepaw map in the SI cortex of rats trained on tactile discrimination. Behavioural Brain Research. 2005, 162: 207.
2-46) Yaoeda K, Shirakashi M, Funaki S, Funaki H, Nakatsue T, Abe H. Measurement of microcirculation in the optic nerve head by laser speckle flowgraphy and scanning laser Doppler flowmetry. Am J Ophthalmol. 2000, 129:734.

**Chapter 3**

3-1) Amir R, Argoff CE, Bennett GJ et al. The role of sodium channels in chronic inflammatory and neuropathic pain. J Pain. 2006, 7: S1.
3-2) Araujo MC, Sinnott CJ, Strichartz GR. Multiple phases of relief from experimental mechanical allodynia by systemic lidocaine: responses to early and late infusions. Pain. 2003, 103: 21.
3-3) Austin VC, Blamire AM, Allers KA et al. Confounding effects of anesthesia on functional activation in rodent brain: a study of halothane and alpha-chloralose anesthesia. Neuroimage. 2005, 24: 92.
3-4) Balasubramanian S, Morley-Forster P, Bureau Y. Opioids and brain imaging. J Opioid Manag. 2006, 2: 147.
3-5) Baron R, Baron Y, Disbrow E, Roberts TP. Brain processing of capsaicin-induced secondary hyperalgesia: a functional MRI study. Neurology. 1999, 53: 548.

3-6) Beardsley D, Holman S, Gantt R et al. Transient neurologic deficit after spinal anesthesia: local anesthetic maldistribution with pencil point needles? Anesth Analg. 1995, 81: 314.
3-7) Berwick J, Devonshire IM, Martindale AJ et al. Cocaine administration produces a protracted decoupling of neural and haemodynamic responses to intense sensory stimuli. Neuroscience. 2005, 132: 361.
3-8) Bennett PN, Aarons LJ, Bending MR et al. Pharmacokinetics of lidocaine and its deethylated metabolite: dose and time dependency studies in man. J Pharmacokinet Biopharm. 1982, 10: 265.
3-9) Bock C, Krep H, Brinker G, Hoehn-Berlage M. Brain mapping of alpha-chloralose anesthetized rats with T2*-weighted imaging: distinction between the representation of the forepaw and hindpaw in the somatosensory cortex. NMR Biomed. 1998, 11: 115.
3-10) Bonica J. The management of pain. Philadelphia: Lea & Febiger. 1953.
3-11) Borras MC, Becerra L, Ploghaus A et al. fMRI measurement of CNS responses to naloxone infusion and subsequent mild noxious thermal stimuli in healthy volunteers. J Neurophysiol. 2004, 91: 2723.
3-12) Cassuto J, Wallin G, Hogstrom S et al. Inhibition of postoperative pain by continuous low-dose intravenous infusion of lidocaine. Anesth Analg. 1985, 64: 971.
3-13) Chang C, Shyu BC. A fMRI study of brain activations during non-noxious and noxious electrical stimulation of the sciatic nerve of rats. Brain Res. 2001, 897: 71.
3-14) Chaplan SR, Bach FW, Shafer SL, Yaksh TL. Prolonged alleviation of tactile allodynia by intravenous lidocaine in neuropathic rats. Anesthesiology. 1995, 83: 775.
3-15) Chen NH, Reith ME. Effects of locally applied cocaine, lidocaine, and various uptake blockers on monoamine transmission in the ventral tegmental area of freely moving rats: a microdialysis study on monoamine interrelationships. J Neurochem. 1994, 63: 1701.
3-16) Devonshire IM, Berwick J, Jones M et al. Haemodynamic responses to sensory stimulation are enhanced following acute cocaine administration. Neuroimage. 2004, 22: 1744.
3-17) Devor M. Neuropathic pain and injured nerve: peripheral mechanisms. Br Med Bull. 1991, 47: 619.
3-18) Devor M, Wall PD, Catalan N. Systemic lidocaine silences ectopic neuroma and DRG discharge without blocking nerve conduction. Pain. 1992, 48: 261.
3-19) de Zwart JA, Silva AC, van Gelderen P et al. Temporal dynamics of the BOLD fMRI impulse response. Neuroimage. 2005, 24: 667.
3-20) Du C, Yu M, Volkow ND et al. Cocaine increases the intracellular calcium concentration in brain independently of its cerebrovascular effects. J Neurosci. 2006, 26: 11522.
3-21) Fuchs A, Rigaud M, Hogan QH. Painful nerve injury shortens the intracellular Ca2+ signal in axotomized sensory neurons of rats. Anesthesiology. 2007, 107: 106.
3-22) Fujitani T, Adachi N, Miyazaki H et al. Lidocaine protects hippocampal neurons against ischemic damage by preventing increase of extracellular excitatory amino acids: a microdialysis study in Mongolian gerbils. Neurosci Lett. 1994, 179: 91.
3-23) Goldin AL. Diversity of mammalian voltage-gated sodium channels. In: Ruby B, Seeburg P, eds. Molecular and functional diversity of ion channels and receptors. New York: New York Academy of Sciences. 1999: 38.

3-24) Groudine SB, Fisher HA, Kaufman RP, Jr. et al. Intravenous lidocaine speeds the return of bowel function, decreases postoperative pain, and shortens hospital stay in patients undergoing radical retropubic prostatectomy. Anesth Analg. 1998, 86: 235.
3-25) Hagelberg N, Kajander JK, Nagren K et al. Mu-receptor agonism with alfentanil increases striatal dopamine D2 receptor binding in man. Synapse. 2002, 45: 25.
3-26) Hernandez L, Guzman NA, Hoebel BG. Bidirectional microdialysis in vivo shows differential dopaminergic potency of cocaine, procaine and lidocaine in the nucleus accumbens using capillary electrophoresis for calibration of drug outward diffusion. Psychopharmacology (Berl). 1991, 105: 264.
3-27) Hirsch E, Danober L, Simler S et al. The amygdala is critical for seizure propagation from brainstem to forebrain. Neuroscience. 1997, 77: 975.
3-28) Hogan QH. Role of decreased sensory neuron membrane calcium currents in the genesis of neuropathic pain. Croat Med J. 2007, 48: 9.
3-29) Huang JH, Thalhammer JG, Raymond SA, Strichartz GR. Susceptibility to lidocaine of impulses in different somatosensory afferent fibers of rat sciatic nerve. J Pharmacol Exp Ther. 1997, 282: 802.
3-30) Ikeda M, Dohi T, Tsujimoto A. Protection from local anesthetic-induced convulsions by gamma-aminobutyric acid. Anesthesiology. 1982, 56: 365.
3-31) Jonsson A, Cassuto J, Hanson B. Inhibition of burn pain by intravenous lignocaine infusion. Lancet. 1991, 338: 151.
3-32) Kanai Y, Katsuki H, Takasaki M. Graded, irreversible changes in crayfish giant axon as manifestations of lidocaine neurotoxicity in vitro. Anesth Analg. 1998, 86: 569-73.
3-33) Keilholz SD, Silva AC, Raman M et al. Functional MRI of the rodent somatosensory pathway using multislice echo planar imaging. Magn Reson Med. 2004, 52: 89.
3-34) Kida I, Hyder F, Behar KL. Inhibition of voltage-dependent sodium channels suppresses the functional magnetic resonance imaging response to forepaw somatosensory activation in the rodent. J Cereb Blood Flow Metab. 2001, 21: 585.
3-35) Kida I, Smith AJ, Blumenfeld H et al. Lamotrigine suppresses neurophysiological responses to somatosensory stimulation in the rodent. Neuroimage. 2006, 29: 216.
3-36) Kragh J, Bolwig TG, Woldbye DP, Jorgensen OS. Electroconvulsive shock and lidocaine-induced seizures in the rat activate astrocytes as measured by glial fibrillary acidic protein. Biol Psychiatry. 1993, 33: 794.
3-37) Lam AM, Donlon E, Engl CC. The effect of lidocaine on cerebral blood flow and metabolism during normocapnia and hypocapnia in humans. Am Soc Anesthesiologist. 1993, 79: A202.
3-38) Lowe AS, Beech JS, Williams SC. Small animal, whole brain fMRI: innocuous and nociceptive forepaw stimulation. Neuroimage. 2007, 35: 719.
3-39) Mao J, Chen LL. Systemic lidocaine for neuropathic pain relief. Pain. 2000, 87: 7.
3-40) Matharu MS, Cohen AS, Goadsby PJ. SUNCT syndrome responsive to intravenous lidocaine. Cephalalgia. 2004, 24: 985.
3-41) McCallum JB, Kwok WM, Sapunar D et al. Painful peripheral nerve injury decreases calcium current in axotomized sensory neurons. Anesthesiology. 2006, 105: 160.

3-42) Niederlehner JR, DiFazio CA, Foster J, Westfall TC. Cerebral monoamines and lidocaine toxicity in rats. Anesthesiology. 1982, 56: 184-7.
3-43) Petersen KL, Rowbotham MC. Will ion-channel blockers be useful for management of nonneuropathic pain? J Pain. 2000, 1: 26.
3-44) Peyron R, Laurent B, Garcia-Larrea L. Functional imaging of brain responses to pain. A review and meta-analysis. Neurophysiol Clin. 2000, 30: 263.
3-45) Radwan IA, Saito S, Goto F. The neurotoxicity of local anesthetics on growing neurons: a comparative study of lidocaine, bupivacaine, mepivacaine, and ropivacaine. Anesth Analg. 2002, 94: 319.
3-46) Rutter JJ, Baumann MH, Waterhouse BD. Systemically administered cocaine alters stimulus-evoked responses of thalamic somatosensory neurons to perithreshold vibrissae stimulation. Brain Res. 1998, 798: 7.
3-47) Rutter JJ, Devilbiss DM, Waterhouse BD. Effects of systemically administered cocaine on sensory responses to peri-threshold vibrissae stimulation: individual cells, ensemble activity, and animal behaviour. Eur J Neurosci 2005, 22: 3205.
3-48) Rykaczewska-Czerwinska M. Antinociceptive effect of lidocaine in rats. Pharmacol Rep. 2006, 58: 961.
3-49) Sakura S, Bollen AW, Ciriales R, Drasner K. Local anesthetic neurotoxicity does not result from blockade of voltage-gated sodium channels. Anesth Analg. 1995, 81: 338.
3-50) Sakura S, Kirihara Y, Muguruma T et al. The comparative neurotoxicity of intrathecal lidocaine and bupivacaine in rats. Anesth Analg. 2005, 101: 541.
3-51) Shah YB, Haynes L, Prior MJ et al. Functional magnetic resonance imaging studies of opioid receptor-mediated modulation of noxious-evoked BOLD contrast in rats. Psychopharmacology (Berl). 2005, 180: 761.
3-52) Spenger C, Josephson A, Klason T et al. Functional MRI at 4.7 tesla of the rat brain during electric stimulation of forepaw, hindpaw, or tail in single- and multislice experiments. Exp Neurol. 2000, 166: 246.
3-53) Strichartz GR, Zhou Z, Sinnott C, Khodorova A. Therapeutic concentrations of local anaesthetics unveil the potential role of sodium channels in neuropathic pain. Novartis Found Symp. 2002, 241: 189.
3-54) Tanelian DL, MacIver MB. Analgesic concentrations of lidocaine suppress tonic A-delta and C fiber discharges produced by acute injury. Anesthesiology. 1991, 74: 934.
3-55) Thomson AH, Elliott HL, Kelman AW et al. The pharmacokinetics and pharmacodynamics of lignocaine and MEGX in healthy subjects. J Pharmacokinet Biopharm. 1987, 15: 101.
3-56) Tracey I, Becerra L, Chang I et al. Noxious hot and cold stimulation produce common patterns of brain activation in humans: a functional magnetic resonance imaging study. Neurosci Lett. 2000, 288: 159.
3-57) Verkhratsky A. Calcium ions and integration in neural circuits. Acta Physiol (Oxf). 2006, 187: 357.
3-58) Waxman SG, Hains BC. Fire and phantoms after spinal cord injury: Na+ channels and central pain. Trends Neurosci. 2006, 29: 207.
3-59) Wise RG, Rogers R, Painter D et al. Combining fMRI with a pharmacokinetic model to determine which brain areas activated by painful stimulation are specifically modulated by remifentanil. Neuroimage. 2002, 16: 999.

3-60) Wise RG, Williams P, Tracey I. Using fMRI to quantify the time dependence of remifentanil analgesia in the human brain. Neuropsychopharmacology. 2004, 29: 626.
3-61) Woodward JJ, Compton DM, Balster RL, Martin BR. In vitro and in vivo effects of cocaine and selected local anesthetics on the dopamine transporter. Eur J Pharmacol. 1995, 277: 7.
3-62) Yamashita A, Matsumoto M, Matsumoto S et al. A comparison of the neurotoxic effects on the spinal cord of tetracaine, lidocaine, bupivacaine, and ropivacaine administered intrathecally in rabbits. Anesth Analg. 2003, 97: 512.
3-63) Zhao P, Waxman SG, Hains BC. Sodium channel expression in the ventral posterolateral nucleus of the thalamus after peripheral nerve injury. Mol Pain. 2006, 2: 27.

**Chapter 4**

4-1) Barbier E, Silva A, Kim S, Koretsky A. Perfusion imaging using dynamic arterial spin labeling (DASL). Mag. Res. in Med. 2001, 45: 1021.
4-2) Choi B, Ramirez-San-Juan J, Lotfi J, Nelson J. Linear response range characterization and in vivo application of laser speckle imaging of blood flow dynamics. JBO. 2006, 11: 1.
4-3) Dunn A, Devor A, Bolay H, et al. Simultaneous imaging of total cerebral hemoglobin concentration, oxygenation, and blood flow during functional activation. Opt. Lett. 2003, 28: 28.
4-4) Durduran T, Burnett M, Yu G, Zhou C, et al. Spatiotemporal Quantification of Cerebral Blood Flow During Functional Activation in Rat Somatosensory Cortex Using Laser-Speckle Flowmetry. J. Cereb. Blood Flow Metab. 2004, 24: 518.
4-5) Kleinfeld D, Mitra P, Helmchen F, Denk W. Fluctuations and stimulus-induced changes in blood flow observed in individual capillaries in layers 2 through 4 of rat neocortex. PNAS. 1998, 95: 15741.
4-6) Leitgeb R, Schmetterer L, Drexler W, Fercher A. Real-time assessment of retinal blood flow with ultrafast acquisition by color Doppler Fourier domain optical coherence tomography. Opt. Ex. 2003, 11: 3116.
4-7) Wang R, Jacques S, and Ma1 Z, et al. Three dimensional optical angiography. Opt. Ex. 2007, 15: 4083.

**Chapter 5**

5-1) Albuquerque ML, Monito CL, Shaw L, Anday EK. Ethanol, morphine and barbiturate alter the hemodynamic and cerebral response to cocaine in newborn pigs. Biol. Neonate. 1995, 67: 432.
5-2) Anday EK, Lien R, Goplerud JM, Kurth DC, Shaw LM. Pharmacokinetics and effect of cocaine on cerebral blood flow in the newborn. Dev. Pharmacol. Ther. 1993, 20: 35.
5-3) Bardo MT. Neuropharmacological mechanisms of drug reward: beyond dopamine in the nucleus accumbens. Crit. Rev. Neurobiol. 1998, 12: 37.
5-4) Bonvento G, Charbonné R, Corrèze JL, Borredon J, Seylaz J, Lacombe P. Is alpha-chloralose plus halothane induction a suitable anesthetic regimen for cerebrovascular research? Brain Res. 1994, 665: 213.
5-5) Briers JD, Webster S. Laser speckle contrast analysis (LASCA): a nonscanning, full-field technique for monitoring capillary blood flow. J. Biomed. Opt. 1996, 1, 174.

5-6) Briers JD. Laser Doppler, speckle and related techniques for blood perfusion mapping and imaging. Physiol. Meas. 2001, R35.
5-7) Brust JC. Vasculitis owing to substance abuse. Neurol. Clin. 1997, 15: 945.
5-8) Buttner A, Mall G, Penning R, Sachs H. Theneuropathology of cocaine abuse. Leg. Med. (Tokyo) 2003, 5: S240.
5-9) Du C, Koretsky AP, Izrailtyan I, Benveniste H. Simultaneous detection of blood volume, oxygenation, and intracellular calcium changes during cerebral ischemia and reperfusion in vivo using diffuse reflectance and fluorescence. J. Cereb. Blood Flow Metab. 2005, 25: 1078.
5-10) Du C, Yu M, Volkow ND, Koretsky AP, Fowler JS, Benveniste H. Cocaine increases intracellular concentration of calcium in brain independently of its cerebrovascular effects. J. Neurosci. 2006, 26: 11522.
5-11) Dunn A, Devor A, Dale AM, Boas DA. Spatial extent of oxygen metabolism and hemodynamic changes during functional activation of the rat somatosensory cortex. Neuro-Image. 2005, 27: 279.
5-12) Durduran T, Burnett M, Yu G, Zhou C, Furuya D, Yodh A, Detre J, Greenberg J. Spatiotemporal quantification of cerebral blood flow during functional activation in rat somatosensory cortex using laser-speckle flowmetry. J. Cereb. Blood Flow Metab. 2004, 24: 518.
5-13) Gleason CA, Traystman RJ. Cerebral responses to maternal cocaine injection in immature fetal sheep. Pediatr. Res. 1995, 38: 943.
5-14) Gollub RL, Breiter HC, Kantor H, Kennedy D, Gastfriend D, Mathe RT, Makris N, Guimaraes A, Riorden J, Campbell T, Foley M, Hyman SE, Rosen B, Weisskoff R. Cocaine decreases cortical cerebral blood flow but does not obscure regional activation in functional magnetic resonance imaging in human subjects. J. Cereb. Blood Flow Metab. 1998, 18: 724.
5-15) Iida H, Gleason CA, O'Brien TP, Traystman RJ. Fetal response to acute fetal cocaine injection in sheep. Am. J. Physiol. 1994, 267: H1968.
5-16) Kaufman MJ, Levin JM, Maas LC, Rose SL, Lukas SE, Mendelson JH, Cohen BM, Renshaw PF. Cocaine decreases relative cerebral blood volume in humans: a dynamic susceptibility contrast magnetic resonance imaging study. Psychopharmacology. 1998, 138: 76.
5-17) Leitgeb R, Schmetterer L, Drexler W, Fercher A, Zawadzki R, Bajraszewski T. Real-time assessment of retinal blood flow with ultrafast acquisition by color DopplerFourier domain optical coherence tomography. Opt. Express. 2003, 11: 3116.
5-18) Lenz C, Frietsch T, Futterer C, Rebel A, van Ackern K, Kuschinsky W, Waschke KF. Local coupling of cerebral blood flow to cerebral gluocose metabolism during inhalational anesthesia in rats: desflurane versus isoflurane. Anesthesiology. 1999, 91:1720.
5-19) London ED, Cascella NG, Wong DF, Phillips RL, Dannals RF, Links JM, Herning R, Grayson R, Jaffe JH, Wagner Jr HN. Cocaine-induced reduction of glucose utilization in the human brain: a study using positron emission tomography and [fluorine18]-fluorodeoxyglucose. Arch. Gen. Psychiatry, 1990, 47: 567.
5-20) Luo F, Wu G, Li Z, Li SJ. Characterization of effects of mean arterial blood pressure induced by cocaine and cocaine methiodide on BOLD signals in rat brain. Magn. Reson. Med. 2003, 49: 264.

5-21) Luo Z, Wang Z, Yuan Z, Du C, Pan Y. Optical coherence Doppler tomography quantifies laser speckle contrast imaging for blood flow imaging in the rat cerebral cortex. Opt. Lett. 2008, 33: 1156.
5-22) Maekawa T, Tommasino C, Shapiro HM, Keifer-Goodman J, Kohlenberger RW. Local cerebral blood flow and glucose utilization during isoflurane anesthesia in the rat. Anesthesiology. 1986, 65: 144.
5-23) Marota JJ, Mandeville JB, Weisskoff RM, Moskowitz MA, Rosen BR, Kosofsky BE. Cocaine activation discriminates dopaminergic projections by temporal response: an fMRI study in rat. NeuroImage. 2000, 11: 13.
5-24) Martinez NE, Diez-Tejedor E, Frank A. Vasospasm/thrombus in cerebral ischemia related to cocaine abuse. Stroke. 1996, 27: 147.
5-25) Masamoto K, Kim T, Fukuda M, Wang P, Kim SG. Relationship between neural, vascular and BOLD signals in isoflurane-anesthetized rat somatosensory cortex. Cereb. Cortex. 2007, 17: 942.
5-26) Pearlson GD, Jeffery PJ, Harris GJ, Ross CA, Fischman MW, Camargo EE. Correlation of acute cocaineinduced changes in local cerebral blood flow with subjective effects. Am. J. Psychiatry. 1993, 150: 495.
5-27) Schmidt KF, Febo M, Shen Q, Luo F, Sicard KM, Ferris CF, Stein EA, Duong TQ. Hemodynamic and metabolic changes induced by cocaine in anesthetized rat observed with multimodal functional MRI. Psychopharmacology. 2006, 185: 479.
5-28) Stankovic MR, Fujii A, Maulik D, Kirby D, Stubblefield PG. Optical brain monitoring of the cerebrovascular effects induced by acute cocaine exposure in neonatal pigs. J. Maternal–Fetal Investig. 1998, 8: 108.
5-29) Wallace EA, Wisniewski G, Zubal G, Vandyck CH, Pfau SE, Smith EO, Rosen MI, Sullivan MC, Woods SW, Kosten TR. Acute cocaine effects on absolute cerebral blood flow. Psychopharmacology. 1996, 128: 17.
5-30) Wang R, Jacques S, Ma Z, Hurst S, Hanson S, Gruber A. Three dimensional optical angiography. Opt. Express. 2007, 15: 4083.
5-31) Yonetani M, Lajevardi N, Pastuszko A. Delivoria-Papadopoulos M, Dopamine, blood flow and oxygen pressure in brain of newborn piglets. Biochem. Med. Metabol. Biol. 1994, 51: 91.

**Chapter 6**

6-1) Bandyopadhyay R, Gittings AS, Suh SS, Dixon PK, Durian DJ. Speckle-visibility spectroscopy: A tool to study time-varying dynamics. Rev Sci Instru. 2005, 76:093110.
6-2) Briers JD, Webster S. Laser speckle contrast analysis (LASCA): A nonscanning, full-field technique for monitoring capillary blood flow. J. Biomed. Opt. 1996, 1: 174.
6-3) Du C, Koretsky AP, Izrailtyan I and Benveniste H. Simultaneous detection of blood volume, oxygenation, and intracellular calcium changes during cerebral ischemia and reperfusion in vivo using diffuse reflectance and fluorescence. J Cereb Blood Flow Metab. 2005, 25: 1078.
6-4) Dunn AK, Devor A, Bolay H, Andermann ML, Moskowitz MA, Dale AM, Boas D A. Simultaneous imaging of total cerebral hemoglobin concentration, oxygenation, and blood flow during functional activation. Opt Lett. 2003, 28:28.
6-5) Hebel R, Stromberg MW. Anatomy and Embryology of the Laboratory Rat. Biomed Verlag. 1986.

6-6) Jones M, Berwick J, Johnston D, Mayhew J. Concurrent optical imaging spectroscopy and laser-Doppler flowmetry: The relationship between blood flow, oxygenation, and volume in rodent barrel cortex. NeuroImage. 2001, 13(6): 1002.
6-7) Luo Z, Wang Z, Yuan Z, Du C, Pan Y. Optical coherence Doppler tomography quantifies laser speckle contrast imaging for blood flow imaging in the rat cerebral cortex. Opt Lett. 2008, 33(10): 1156.
6-8) Takatani S, Graham MD. Theoretical analysis of diffuse reflectance from a two-layer tissue model,IEEE Trans. Biomed. Eng. 1987, 26: 656.
6-9) Zhang HF, Maslov K, Sivaramakrishnan M, Stoica G, Wang LH. Imaging of hemoglobin oxygen saturation variations in single vessels in vivo using photoacoustic microscopy. Appl Phys Lett. 2007, 90(5): 053901.

## Appendix A

Based on equ (1-1)~(1-4), $N(t)$ and $I(t)$ following the onset of the first stimulus pulse can be expressed as below

$$When\ S(t) = S_0,\ t = 0 \sim T_s$$

$$I(t) = I_{sss}(1 - e^{-\frac{k+1}{\tau_1}t}) + I(0^-)e^{-\frac{k+1}{\tau_1}t} = I_{sss}(1 - e^{-\frac{k+1}{\tau_1}t}) + I_{ssr}e^{-\frac{k+1}{\tau_1}t}$$

$$= (I_{sss} - I_{ssr})(1 - e^{-\frac{k+1}{\tau_1}t}) + I_{ssr} \tag{A-1}$$

$$N(t) = N_{sss}(1 - e^{-\frac{k+1}{\tau_1}t}) + (S_0 + N(0^-))e^{-\frac{k+1}{\tau_1}t} = N_{sss}(1 - e^{-\frac{k+1}{\tau_1}t}) + (S_0 + N_{ssr})e^{-\frac{k+1}{\tau_1}t}$$

$$= (S_0 + N_{ssr} - N_{sss})e^{-\frac{k+1}{\tau_1}t} + N_{sss}$$

$N(t)$ described by these equations would jump to an initial peak at $S_0$+$N(0^-)$, and then decay towards a plateau at $N_{sss}$. In the mean time, the $I(t)$ will gradually increase from I(0) towards a plateau at $I_{sss}$. The stabilization rate is $(k+1)/\tau_1$. The elevated plateau 'sss' can be reached only if the duration $T_s >> \tau_1/(k+1)$.

Likewise, following the end of the first stimulus, $N(t)$ and $I(t)$ can be expressed as below.

$$When\ S(t) = 0,\ t = T_s \sim T_s + T_r$$

$$I(T_s) = \frac{kS_0}{k+1}(1 - e^{-\frac{(k+1)}{\tau_1}Ts}) + \frac{kN_0}{k+1} \tag{A-2}$$

$$if\ N_0 \geq I(T_s)\begin{cases} I(t) = I_{ssr}(1 - e^{-\frac{k+1}{\tau_1}(t-T_s)}) + I(T_s)e^{-\frac{k+1}{\tau_1}(t-T_s)} \\ N(t) = N_{ssr}(1 - e^{-\frac{k+1}{\tau_1}(t-T_s)}) + (N_0 - I(T_s))e^{-\frac{k+1}{\tau_1}(t-Ts)} \end{cases}$$

$$if\ N_0 < I(T_s)\begin{cases} I(t) = \begin{cases} I(T_s)e^{-\frac{1}{\tau_1}(t-Ts)} & T_s + T_{z1} \geq t \geq T_s \\ I_{ssr}(1 - e^{-\frac{k+1}{\tau_1}(t-T_s-T_{z1})}) + N_0 e^{-\frac{k+1}{\tau_1}(t-Ts-T_{z1})} & T_s + T_r \geq t \geq T_s + T_{z1} \end{cases} \\ N(t) = \begin{cases} 0 & T_s + T_{z1} \geq t \geq T_s \\ N_{ssr}(1 - e^{-\frac{k+1}{\tau_1}(t-T_s-T_{z1})}) & T_s + T_r \geq t \geq T_s + T_{z1} \end{cases} \end{cases}$$

$$T_{z1} = \tau_1 \ln\frac{I(T_s)}{N_0} \qquad where\ I(t) = I(T_s + T_{z1}) = N_0 \quad and \quad N(t) = N(T_s + T_{z1}) = 0$$

$N(t)$ would immediately drop to $N_0$–$I(Ts)$ if disregarding the zero threshold, and then recover towards $N_{ssr}$. In the meant time, $I(t)$ will decrease from $I(Ts)$ towards $I_{ssr}$. The recovery rate is again $(k+1)/\tau_1$. However, when the threshold is applied and passed ($N_0$-$I(Ts)$<0), the recovery will have two stages. $I(t)$ will first decrease from $I(Ts)$ towards $N_0$ at a slow rate of $1/\tau_1$. Then from $N_0$, $I(t)$ will continue to decrease towards $I_{ssr}$ at the fast rate of $(k+1)/\tau_1$. In the mean time, $N(t)$ will first be clamped at 0 until the I(t) meet $N_0$ and

thereafter increase towards $N_{ssr}$ at rate of $(k+1)/\tau_1$. This turning point of I(t) equaling to $N_0$ can be reached before next stimulus if the resting period $T_r$ is longer than $T_{z1}$. And the resting steady state 'ssr' can be again reached only if resting period $T_r$ (in case no thesholding happens) or $T_r - T_{z1} >> \tau_1/(k+1)$. In case $N_0$ equal to 0, N(t) will be always clamped at 0 during rest and with no undershoot below $N_0$ (or 0). I(t) will never really reach $N_0$ (or zero), however, as long as $T_r >> \tau_1$, I(t) still can closely approach its 'ssr' value of zero. Therefore, steady status still can be formed before next stimulus.

The response to subsequent stimulus depends on the how $N(t)$ and $I(t)$ recover to 'ssr' during the rest. The subsequent unsteady scenario can also be deducted with a little more effort, but it is less important in this context. It is worthy to just point out that, in the above equations, the initial inhibition awaiting subsequent stimulus and rest period will be variable $I(i(T_r+T_s))$ and $I(i(T_r+T_s)+T_s)$ different than constants $I_{ssr}$ and $I_{sss}$, even when $N_0$ equal to 0. The peak and valley, $N(i(T_r+T_s)^+)$ and $N(i(T_r+T_s)+Ts^+)$, as well as the turning point $T_{zi}$, obviously will also vary with $i$. Moreover, once $I(iT_r) > I_{ssr}$ and $N(iT_r^-) < N_{ssr}$ are presented at the stimulus onset, the response will be certainly lower than the one started from steady state. Therefore, for the stimulus train to be repeated and the formula above to be continuously applied, long enough resting time $T_r$ should be allowed for closely return to steady state. The only exception is that, when k equal to 0, no inhibition exists and $N(t)$ will exactly follow $S(t)+N_0$ no matter how the stimulus and resting period are arranged.

## Appendix B

In this ballon model model, the venules are treated as a balloon filled by blood flow through capillary (i.e. CBF) and drained by venous flow, noted as $CBF_{out}$. The net in-flow determines the change rate of volume.

$$\begin{aligned}\frac{dv(t)}{dt} &= \frac{dV(t)}{V_0 dt} = \frac{F(t) - F_{out}(t)}{V_0} = \frac{F_0}{V_0}(f(t) - f_{out}(t)) \\ &= \frac{1}{\tau_{MTT}}[f(t) - f_{out}(v,t)]\end{aligned} \tag{B-1}$$

The mean transition time $\tau_{MTT}$ has a physical meaning of $V_0/F_0$. $F_0$ and $V_0$ in cortex tissue has been reported to be around 0.01ml/sec and 0.03ml in 1 ml tissue, therefore $\tau_{MTT}$ has a typical value about 3 sec.

Here, the relative inflow is the driving input from the previous step ($f(t)$). And the relative outflow is regulated against any drastic inflation (dv/dt>0) and deflation (dv/dt<0) by the viscoelasticity of venules, so that the steady state relationship ($f=v^{1/\alpha}$) is maintained. Apparently, we know that, in steady state (d$v$/d$t$=0), in flow equals to out flow.

$$f_{out}(v,t) = v^{\frac{1}{\alpha}}(t) + \tau\frac{dv(t)}{dt} \tag{B-2}$$

The time factor τ reversely represents the strength of the viscoelastic regulation against drastic change. It can be assigned with different values ($\tau_p$,$\tau_n$) during inflation and deflation. The effect of this variation will be seen in the transients of CBV, $[HbR]_a$ and BOLD signals. Apparently, we could know the following relationships during steady state (d$v$/d$t$=0):

$$f_{in} = f_{out} = v^{1/a} \tag{B-3}$$

Combining equ (B-2) and (B-3), we get the transient of $v(t)$ and $f_{out}(t)$ in terms of $f(t)$ and $v(t)$, thus can be numerically solved with input $f(t)$ and initially $v(0)=1$.

$$\frac{dv(t)}{dt} = \frac{f(t) - v(t)^{\frac{1}{\alpha}}}{\tau + \tau_{MTT}} \tag{B-4}$$

$$f_{out}(t) = \frac{\tau \cdot f(t) + \tau_{MTT} \cdot v(t)^{\frac{1}{\alpha}}}{\tau + \tau_{MTT}} \tag{B-5}$$

In the balloon, the changing rate of local HbR content is the difference between the local $CMRO_2$ and washout rate of HbR in veinules, which is the product of $F_{out}$(t) and mean HbR concentration in venules. This is defined by equ (B-6).

$$\frac{dq(t)}{dt} = \frac{dQ(t)}{Q_0 dt} = \frac{M(t) - \overline{[HbR]_b}(t)F_{out}(t)}{Q_0} = \frac{M_0}{Q_0}m(t) - \frac{F_0}{V_0}\cdot\frac{q(t)}{v(t)}\cdot f_{out}(t) \tag{B-6}$$

For those baseline coefficients, we know that they are identical (*i.e.* $M_0/Q_0=F_0/V_0=\tau_{MTT}$) based on the steady state definitions of OEF as in Equ (1-6) and (1-12).

$$so\ \frac{M_0}{Q_0} = \frac{F_0}{V_0} = \frac{1}{\tau_{MTT}} \tag{B-7}$$

By replace the $f_{out}$, we get the following for d$q$/d$t$. This can also be numerically solved knowing $m(t)$, $f(t)$ and $v(t)$ and initially $q(0)=1$.

$$\frac{dq(t)}{dt} = \frac{1}{\tau_{MTT}}\left[ m(t) - \frac{q(t)}{v(t)} \frac{\tau \cdot f(t) + \tau_{MTT} \cdot v(t)^{\frac{1}{\alpha}}}{\tau + \tau_{MTT}} \right] \tag{B-8}$$

Following the equations for CBV and $[HbR]_a$ transient, We can also get the transient of the local $HbO_2$ content, though it is not directly involved in generation of BOLD effect. The baseline OEF $E_0$ was reported to be about 40% in cortex. Moreover, the normalized venous concentration of HbR ($q_b(t)$) and $HbO_2$ ($o_b(t)$) are calculated

$$\begin{aligned} v(t) &= \frac{V(t)}{V_0} = \frac{V(t)\overline{[Hbt]_b}}{V_0\overline{[Hbt]_b}} = \frac{Q(t)+O(t)}{Q_0+O_0} = \frac{Q_0 q(t) + O_0 o(t)}{Q_0 + O_0} \\ &= E_0 q(t) + (1-E_0) o(t) \\ o(t) &= \frac{v(t) - E_0 \cdot q(t)}{1-E_0} = \frac{v(t)-q(t)}{1-E_0} + q(t) \\ q_b(t) &= q(t)/v(t) \quad \& \quad o_b(t) = o(t)/v(t) \end{aligned} \tag{B-9}$$

## Appendix C

The $T_2$-wighted contrast of a typical gradient echo (GE) signal is sensitive to susceptibility, and it can be expressed as the following:

$$S = S(0)\cdot e^{-TE\cdot R_2^*} = S(0)\cdot e^{-TE\cdot(R_{20}^* + R_2')} \tag{C-1}$$

S(0) and S represent the GE signal level before and after the transversal relaxation over period of TE (actually $TE_{eff}$ in EPI). $R^*_{20}$ represents the lumped non-susceptibility transversal relaxation rate. $R'_2$ represents the susceptibility induced transversal decay due to the local magnetic field disturbance ($\Delta$B) in presence of paramagnetic particles, such as venous HbR. Davis *et al* proposed a power approximation between $R'_2$ and $\Delta$B. However, practically, any other signal changes(such as blood volume fraction, *ie* CBV) during activation need to be considered in $R'_2$ to more precisely model the BOLD response. The relation is given in equ(C-2). The exponent $\beta$ mainly depends on the static magnetic field. Theoretical analysis shows, in a modest field (1.5-3T) $\beta$ is approximately 1.5, while in high-field (9.4 T or higher) $\beta$ approaches 1. $\Delta$B is approximately linear with local HbR content ($[HbR]_a$ or Q). And $[HbR]_a$ in turn is proportional to the product of oxygen extraction rate E and venous blood volume CBV in steady state, assuming the constant $[HbT]_b$ in blood.

$$R_2' \sim \Delta B^{\beta} / V^{\beta-1} \sim Q^{\beta} / V^{\beta-1} \sim V\cdot E^{\beta} \tag{C-2}$$

The change of signal level ($\Delta S/S_0$), *ie* BOLD response, can be given as dynamic function of {q,v}. Using the relation q/v=e=m/f induced above for steady state, it can also be expressed in terms of {m,f} in steady state only.

$$\begin{aligned} b-1 = \frac{\Delta S}{S_0} &= e^{-TE\cdot(R_2'-R_{20}')} - 1 \approx TE\cdot(R_{20}' - R_2') = TE\cdot R_{20}'\left(1-\frac{R_2'}{R_{20}'}\right) \\ &= A\left(1-\left(\frac{q^{\beta}}{v^{\beta-1}}\right)\right) = A(1-ve^{\beta}) \\ &= A\left(1-\left(\frac{m^{\beta}}{f^{\beta-\alpha}}\right)\right) \qquad \textit{in steady state} \end{aligned} \tag{C-3}$$

However, in this formula, the relative BOLD contrast *b* also depends on imaging parameter TE and baseline decay rate $R'_{20}$. While $\alpha$ and $\beta$ can be considered region-independent constant, but A varies with locations. In practice, the map of A can be estimated using BOLD and CBF images under hypercapnia challenge, by assuming a constant metabolism rate (m=1).

$$A(X) = \left.\frac{b(X)-1}{(1-f(X)^{\alpha-\beta})}\right|_{Hypercapnia} \tag{C-4}$$

The map of A can then be substituted into equ(C-3) with BOLD and CBF measurements with functional challenge to derive the map of $CMRO_2$ change in steady state, which usually is not directly measurable.

$$m(X) = \left[\left(1-\frac{b(X)-1}{A(X)}\right)f(X)^{-(\alpha-\beta)}\right]^{1/\beta} \tag{C-5}$$